UNIVERSIDADE ESTADUAL DE CAMPINAS
FACULDADE DE ENGENHARIA ELÉTRICA E DE COMPUTAÇÃO
DEPARTAMENTO DE COMPUTAÇÃO E AUTOMAÇÃO INDUSTRIAL

Segmentação de imagens de tensores de difusão no contexto da morfologia matemática

Autor: Leticia Rittner

Orientador: Prof. Dr. Roberto de Alencar Lotufo

Tese de Doutorado apresentada à Faculdade de Engenharia Elétrica e de Computação como parte dos requisitos para obtenção do título de Doutor em Engenharia Elétrica. Área de concentração: **Engenharia de Computação**.
Aprovação em 18/12/2009

Banca Examinadora:
Prof. Dr. André Vital Saúde - DCC/UFLA
Prof. Dr. Fernando Cendes - FCM/UNICAMP
Prof. Dr. Léo Pini Magalhães - FEEC/UNICAMP
Profa. Dra. Nina S. T. Hirata - IME/USP
Prof. Dr. Roberto A. Lotufo - FEEC/UNICAMP

Campinas, SP
2009

FICHA CATALOGRÁFICA ELABORADA PELA
BIBLIOTECA DA ÁREA DE ENGENHARIA - BAE - UNICAMP

Rittner, Leticia
R518s Segmentação de imagens de tensores de difusão no contexto da morfologia matemática /Leticia Rittner. – Campinas, SP: [s.n.], 2009.

Orientador: Roberto A. Lotufo
Tese de Doutorado - Universidade Estadual de Campinas, Faculdade de Engenharia Elétrica e de Computação.

1. Processamento de imagens. 2. Morfologia matemática. 3. Difusão - Imagem de ressonancia magnetica. I. Lotufo, Roberto de Alencar. II. Universidade Estadual de Campinas. Faculdade de Engenharia Elétrica e de Computação. III. Título

Título em Inglês:	Diffusion tensor image segmentation in the mathematical morphology context
Palavras-chave em Inglês:	Image processing, Mathematical morphology Diffusion - Magnetic resonance imaging
Área de concentração:	Engenharia de Computação
Titulação:	Doutor em Engenharia Elétrica
Banca Examinadora:	André Vital Saúde, Fernando Cendes Léo Pini Magalhães, Nina S. T. Hirata
Data da defesa:	18/12/2009
Programa de Pós Graduação:	Engenharia Elétrica

COMISSÃO JULGADORA - TESE DE DOUTORADO

Candidata: Letícia Rittner

Data da Defesa: 18 de dezembro de 2009

Título da Tese: "Segmentação de Imagens de Tensores de Difusão no Contexto da Morfologia Matemática"

Prof. Dr. Roberto de Alencar Lotufo (Presidente): _____

Profa. Dra. Nina Sumiko Tomita Hirata: _____

Prof. Dr. André Vital Saúde: _____

Prof. Dr. Fernando Cendes: _____

Prof. Dr. Léo Pini Magalhães: _____

Resumo

O objetivo principal desta tese é propor um método de segmentação para imagens de tensores de difusão baseado na transformada de *watershed*. Ao invés de adaptar o *watershed* para trabalhar com imagens tensoriais, definimos mapas escalares baseados na morfologia matemática que retêm a informação relevante contida nos tensores para, a partir deles, conseguir a segmentação da imagem aplicando a transformada de *watershed*. Novos mapas baseados em operadores da morfologia matemática são então propostos e analisados. O principal mapa escalar proposto é o gradiente morfológico tensorial (TMG). Um estudo comparativo do TMG com os diversos mapas escalares já existentes demonstra sua superioridade na tarefa de segmentação. Os resultados da segmentação baseada no TMG e no *watershed* hierárquico são comparáveis com resultados de segmentação baseada em atlas. O método proposto é usado para segmentar os núcleos do tálamo, uma tarefa de grande importância para a neuro-ciência. O método também é adaptado para segmentação de imagens coloridas, sendo necessária para tanto a criação de uma representação tensorial específica.

Palavras-chave: segmentação, morfologia matemática, *watershed*, gradiente morfológico tensorial, imagens de tensores de difusão.

Abstract

The main goal of this thesis is to present a segmentation method for diffusion tensor images, based on the watershed transform. Instead of adapting the watershed to work with tensorial images, scalar maps based on mathematical morphology, retaining relevant information from tensors, were defined. The desired segmentation is achieved by applying the watershed over these scalar maps. New scalar maps, based on mathematical morphology, are defined and analyzed. The tensorial morphological gradient (TMG) is the most important among the proposed scalar maps. A comparative study of the TMG with the existing scalar maps shows its superiority in the segmentation task. Segmentation results obtained by the hierarchical watershed over the TMG are comparable to atlas-based segmentation. The proposed method is used to segment the thalamic nuclei, an important task for neuroscience. The method is also adapted to segment color images, requiring a definition of a specific tensorial representation.

Keywords: segmentation, mathematical morphology, watershed, tensorial morphological gradient, diffusion tensor images.

Aos meus pais,
que me mostraram o caminho.

Ao meu marido,
que escolheu caminhar a meu lado.

Aos meus filhos,
que um dia seguirão seus próprios caminhos...

Agradecimentos

"Qualquer trabalho científico, qualquer descoberta,
qualquer invenção é um trabalho universal.
Ele está condicionado em parte pela cooperação de contemporâneos,
em parte pela utilização do trabalho de seus predecessores".
(Karl Marx)

Por isso, tentar nominar as pessoas a quem devo reconhecimento poderia ser injusto. Entretanto, atrevo-me a fazer alguns agradecimentos especiais:

Ao meu orientador , Prof. Roberto de Alencar Lotufo, pela confiança que depositou em mim. Sua orientação impecável e incansável motivou-me sempre a ir além.

Ao Prof. Léo Pini Magalhães, pelo bom humor com que conduziu nossa parceria.

Ao Prof. Bruce Pike, por me receber em seu laboratório, no Montreal Neurologic Institute, e compartilhar comigo sua grande experiência na área. E aos colegas de Montreal, que abrandaram o rigor do inverno me dando espaço e acolhimento durante as horas arduamente trabalhadas.

Ao Prof. Euclides de Mesquita Neto por me ajudar a ingressar no universo tensorial e ao Prof. Fernando Cendes, por expandir meus horizontes para além das fronteiras da engenharia.

Aos amigos Franklin, Romaric, André, Jane e Arthur que, entre um café e outro, enriqueceram este trabalho com suas idéias e experiências. À Mabia, LaTeXWoman, por me salvar nos momentos de apuro. Ao Renan, que se deixou contagiar pelo meu entusiasmo e participou deste trabalho com dedicação. Aos demais colegas do LCA, que fizeram destes anos de doutorado uma época memorável.

À minha família, que embarcou, literalmente, de corpo e alma nesta empreitada. Seu apoio, companhia e torcida foram, sem dúvida, fundamentais para que eu chegasse até aqui.

Ao CNPq e à CAPES, pelo apoio financeiro.

Sumário

Lista de Figuras

Lista de Tabelas

Glossário

AVC	Acidente vascular cerebral
CI	Índice de coerência (coherence index)
CIELUV	Modelo de cor - “X, Y e Z” - (criado pela Comission Internationale de l’Éclairage)
DP	Produto escalar (dot product)
DTI	Imagem de tensores de difusão (diffusion tensor imaging)
FA	Anisotropia fracional (fractional anisotropy)
fMRI	Imagem de ressonância magnética funcional (functional magnetic resonance imaging)
FN	Norma de Frobenius (Frobenius Norm)
HSL	Modelo de cor - “hue, saturation, luminance”
HSV	Modelo de cor - “hue, saturation, value”
IHSL	Modelo de cor - HSL modificado (improved HSL)
J-div	Divergência de Kullback-Leibler (J-divergence)
LI	Índice de reticulado (Lattice index)
LogE	Distância Log-Euclideana (Log-Euclidean distance)
MD	Difusividade média (mean diffusivity)
MRI	Imagem de ressonância magnética (magnetic resonance imaging)
PD	Densidade de próton (proton density)
PED	Direção do autovetor principal (principal eigenvector direction)
RGB	Modelo de cor - “red, green, blue”
Riem	Distância de Riemannian (Riemannian distance)
ROI	Região de interesse (region of interest)

TDP Produto tensorial (tensorial dot product)

TMG Gradiente morfológico tensorial (tensorial morphological gradient)

VF Fração de volume (volume fraction)

VR Razão de volume (volume ratio)

Trabalhos Produzidos Pelo Autor

1. L. Rittner, F. Flores, and R. Lotufo. New tensorial representation of color images: Tensorial morphological gradient applied to color image segmentation. In *SIBGRAPI07: Proceedings of the XX Brazilian Symposium on Computer Graphics and Image Processing*, pages 45–52, Belo Horizonte, Brazil, 2007. IEEE Computer Society.

2. L. Rittner and R. Lotufo. Diffusion tensor imaging segmentation by watershed transform on tensorial morphological gradient. In *SIBGRAPI08: Proceedings of the XXI Brazilian Symposium on Computer Graphics and Image Processing*, pages 196–203, Campo Grande, Brazil, 2008. IEEE Computer Society.

3. L. Rittner and R. Lotufo. Segmentation of DTI based on tensorial morphological gradient. In *Medical Imaging 2009: Image Processing*, volume 7259, page 72591E, 2009. SPIE.

4. L. Rittner, F. Flores and R. Lotufo. A tensorial framework for color images, Pattern Recognition Letters, 2009. In press.

5. L. Rittner, S. Appenzeller and R. Lotufo. Segmentation of brain structures by watershed transform on tensorial morphological gradient of diffusion tensor imaging. In *SIBGRAPI09: the XXII Brazilian Symposium on Computer Graphics and Image Processing*, Rio de Janeiro, Brazil, 2009. In press.

6. L. Rittner, J. Campbell, G.B. Pike and R. Lotufo. Segmentation of diffusion tensor fields based on scalar maps and mathematical morphology. *IEEE Transactions on Medical Imaging*. Submitted.

7. L. Rittner, J. Campbell, G.B. Pike and R. Lotufo. Segmentation of thalamic nuclei based on tensorial morphological gradient of diffusion tensor field. *International Symposium on Biomedical Imaging 2010*. Submitted.

8. R. Lobo, L. Rittner, R. Lotufo and L. Magalhães. MM-DTI: visualization and segmentation tool for diffusion tensor images. *International Symposium on Biomedical Imaging 2010*. Submitted.

Capítulo 1

Introdução

1.1 Motivação

A imagem de difusão é uma nova modalidade de imagem por ressonância magnética, muito utilizada na área médica em estudos relacionados ao cérebro. Ela trabalha com a mensuração das tendências do movimento aleatório das moléculas de água em um dado meio. Normalmente estas moléculas se movem desordenadamente em altas velocidades em todas as direções, colidindo umas com as outras assim como com as demais moléculas do meio. Tais colisões dão origem ao movimento de difusão. Em certas regiões do cérebro, este movimento aleatório se dá de forma idêntica em todas as direções, recebendo o nome de movimento isotrópico. Em outras regiões, onde o tecido cerebral é altamente organizado, o movimento das moléculas fica restrito à direção paralela à orientação da estrutura do tecido. A este movimento com direção preferencial, dá-se o nome de difusão anisotrópica.

Em regiões de difusão anisotrópica, o comportamento do movimento das moléculas de água não pode mais ser caracterizado por um único coeficiente de difusão, pois varia de acordo com a direção na qual ele está sendo observado. Quanto mais organizado o tecido, mais o coeficiente de difusão depende da direção em que o mesmo está sendo medido. Nesse caso é necessário lançar mão de um modelo mais complexo, o tensor de difusão, que consegue descrever deslocamentos por unidade de tempo diferentes em cada direção. Dá-se, então, o nome de imagem de tensores de difusão (DTI) à imagem que contém em cada voxel o tensor de difusão que descreve, não só a mobilidade molecular ao longo de todas as direções naquele voxel, mas também a correlação entre elas. Para construir a imagem de tensores de difusão, são necessárias imagens de difusão em no mínimo seis direções, além de uma imagem sem gradiente de difusão.

Há duas razões pelas quais a imagem de tensores de difusão (DTI) é uma modalidade importante. Primeiro, porque ela é capaz de revelar detalhes da anatomia da substância branca do cérebro, ao

contrário da imagem de ressonância magnética (MRI) convencional. Isso porque a MRI convencional baseia-se na composição química dos tecidos, sendo capaz apenas de diferenciar substância branca de substância cinzenta. Contudo, apesar de quimicamente homogênea, a substância branca é composta por feixes de fibras que conectam regiões distintas do cérebro. Estas conexões podem ser claramente identificadas pelas imagens de tensores de difusão, que indicam maior difusividade na direção paralela às fibras e menor difusividade em direções ortogonais em relação ao feixe de fibras.

A segunda razão se deve ao fato da DTI ser a primeira modalidade de imagem que fornece pistas para entender a conectividade do cérebro. Em patologias onde o estudo anatômico não é suficiente para explicar determinados comportamentos e sintomas, somente uma imagem que forneça informação das conexões preservadas ou comprometidas parece poder ajudar em seu diagnóstico e tratamento.

Nos últimos anos, o número de trabalhos publicados na área de imagens de difusão vem crescendo rapidamente. Existe um número significativo de estudos sendo desenvolvidos no campo de visualização das imagens de difusão, pois além de se tratarem de grandezas tridimensionais, precisam ser visualizadas em um contexto tridimensional [Westin et al., 2002, Zhang et al., 2004, He et al., 2004]. Há ainda trabalhos relatando a utilização das medidas extraídas das imagens de difusão para auxiliar no diagnóstico, na melhor compreensão e no tratamento de diversas patologias [Dong et al., 2004]. As patologias mais estudadas utilizando-se medidas de difusão são: Esclerose Múltipla [Cercignani et al., 2001, Bozzali et al., 2002, Rovaris et al., 2005], Acidente vascular cerebral (AVC) [Thomalla et al., 2005, Gupta et al., 2006], Epilepsia [Eriksson et al., 2001, Assaf et al., 2003, Thivard et al., 2006], Demência [Bozzali et al., 2005, Bozzali and Cherubini, 2007], Tumor [Mardor et al., 2001, Hein et al., 2004], Parkinson [Nicoletti et al., 2006, Chan et al., 2007, Tessa et al., 2008], entre outras[Symms et al., 2004]. Já a Tractografia baseada em DTI [Basser et al., 2000, Mori and van Zijl, 2002, Xu et al., 2002, Parker et al., 2003, Li and Wünsche, 2005, Zhang et al., 2005] visa acompanhar o caminho percorrido pelos tratos neuronais, possibilitando a geração de um mapa anatômico *in vivo*, além de viabilizar estudos de conectividade em conjunto com a ressonância magnética funcional (fMRI) e planejamento cirúrgico.

Além das áreas de pesquisa citadas acima, outro assunto que está sendo bastante estudado recentemente é a segmentação das imagens de tensores de difusão. Esta segmentação é uma etapa necessária para permitir a análise quantitativa de difusão em uma determinada estrutura do cérebro. Normalmente, o delineamento da estrutura a ser estudada é feito em uma imagem de ressonância convencional e depois transferido para imagens de tensores de difusão após registro destas imagens. A utilização de um método de segmentação baseado em DTI eliminaria a necessidade de registro das imagens, reduzindo o tempo de processamento e evitando eventuais erros introduzidos pelo registro.

Outra razão para se buscar um método de segmentação baseado em DTI é a capacidade da DTI de distinguir regiões de estruturas cerebrais, não identificadas por nenhuma outra modalidade de imagem (ex: núcleos do tálamo), graças à informação direcional que ela contém.

Alguns dos principais motivos que fazem da segmentação de imagens de tensores de difusão uma tarefa difícil são: a complexidade das imagens de tensores de difusão, formadas por grandezas tridimensionais em um contexto tridimensional; a baixa resolução desta modalidade de imagem, devido à limitações atuais no processo de aquisição; a dificuldade de avaliar o resultado da segmentação, já que uma análise qualitativa depende do observador conhecer o resultado esperado e uma avaliação quantitativa não é possível sem um padrão ouro.

Dentre os métodos de segmentação de imagens de tensores de difusão propostos na literatura, podemos citar os baseados em grafo [Ziyan et al., 2006, Weldeselassie and Hamarneh, 2007], *level-set* [Zhukov et al., 2003, Wang and Vemuri, 2005, Jonasson et al., 2005], evolução de superfície [Lenglet et al., 2006] e crescimento de regiões [Niogi et al., 2007].

1.2 Objetivos

Conforme descrito na seção anterior, a DTI traz vantagens por ser a única modalidade de imagem de ressonância magnética a conter informação direcional, mas ao mesmo tempo introduz dificuldades devido à sua complexidade. Assim, o objetivo principal desta tese é propor um método de segmentação para imagens de tensores de difusão baseado na transformada de *watershed*. Como o cálculo de um gradiente da imagem original é uma etapa fundamental da segmentação baseada em *watershed*, é necessário inicialmente definir uma forma de calcular tal gradiente a partir de imagens tensoriais. De posse deste gradiente, mostramos então como é possível aplicar o *watershed* hierárquico para segmentar imagens tensoriais, tanto sintéticas quanto reais.

Em resumo, os objetivos desta tese são:

- propor um gradiente morfológico tensorial (TMG) que sintetizasse as principais informações contidas nos tensores de difusão e transcrevesse estas informações para um mapa escalar;
- uma vez de posse deste mapa escalar, aplicar métodos de segmentação conhecidos, como por exemplo, a limiarização e a transformada de *watershed*, para obter a segmentação de imagens de tensores de difusão;
- investigar a influência no resultado final da segmentação, da escolha da função de similaridade e do elemento estruturante utilizados no cálculo do TMG;
- analisar outros mapas escalares de difusão já propostos na literatura, e discutir a possibilidade de utilização destes mapas no método de segmentação proposto;

- propor ainda novos mapas escalares, com base nos já existentes e nos conceitos da morfologia matemática.
- investigar a facilidade de segmentação de estruturas do cérebro a partir de imagens de tensores de difusão;
- verificar a viabilidade de se utilizar as imagens de tensores de difusão para encontrar subdivisões de estruturas complexas do cérebro, como o tálamo, por exemplo.

1.3 Base conceitual

1.3.1 Representação das imagens de tensores de difusão

O cérebro é composto basicamente por três tipos de tecidos distintos: substância branca, substância cinzenta e fluído cérebro-espinhal. Estes tecidos possuem níveis distintos de organização celular, restringindo de forma diferente o movimento das moléculas de água e resultando em movimentos de difusão que vão, do completamente isotrópico, até o movimento de difusão anisotrópico. Nestas regiões, a difusão não pode mais ser descrita por um único escalar, mas sim, por um tensor, que representa não só a mobilidade molecular ao longo de todas as direções, mas também a correlação entre elas [Basser and Pierpaoli, 1996].

Isso quer dizer que a cada voxel da imagem de tensores de difusão está associado um tensor de segunda ordem, que representa a difusão das moléculas de água no cérebro humano. Ele normalmente é escrito na forma de uma matriz 3×3:

$$\mathbf{T} = \begin{pmatrix} T_{xx} & T_{xy} & T_{xz} \\ T_{yx} & T_{yy} & T_{yz} \\ T_{zx} & T_{zy} & T_{zz} \end{pmatrix} \tag{1.1}$$

Como T, no caso da difusão, é uma matriz simétrica definida positiva, os autovalores (λ_1, λ_2, λ_3) da matriz são reais e seus autovetores (e_1, e_2, e_3) são ortogonais. Nesse caso, o tensor pode ser representado por um elipsóide (Fig. 1.1), cuja orientação é definida pelos autovetores e cujos raios correspondem à raiz quadrada dos autovalores associados a cada um dos eixos (autovetores).

É importante entender o que o elipsóide traz de informação dos tensores de difusão. Dada uma molécula na origem, o elipsóide definido pelos autovetores e autovalores do tensor representa para onde esta molécula poderá difundir com igual probabilidade. O tamanho do elipsóide traduz a "quantidade" de difusão, enquanto que a forma do elipsóide, mais ou menos alongada, reflete o grau de anisotropia do tensor de difusão.

1.3.2 Medidas escalares de difusão

Para atingir o objetivo pretendido e realizar a segmentação de uma imagem de tensores de difusão do cérebro utilizando-se a transformada de *watershed*, primeiro é necessário calcular o gradiente desta imagem. Ou seja, é necessário transformar a imagem tensorial em uma imagem escalar, que contenha de preferência, informação das transições existentes na imagem original. Mas, enquanto que para imagens escalares já existem diversas formas estabelecidas de se calcular o gradiente, o mesmo não acontece com imagens tensoriais.

Existem diversas medidas escalares extraídas das imagens de tensores de difusão já propostas na literatura. Estas medidas podem ser basicamente classificadas como medidas intravoxel, que levam em consideração apenas o tensor em questão, e medidas intervoxel, que levam em consideração o tensor e seus vizinhos. Este segundo grupo, pode ainda ser subdividido em distâncias tensoriais e índices de anisotropia de vizinhança.

A maioria destes mapas escalares baseia-se apenas nos autovalores dos tensores, como por exemplo, a difusividade média (MD) e a anisotropia fracional (FA):

$$MD = \frac{\lambda_1 + \lambda_2 + \lambda_3}{3} = \frac{Trace}{3}, \tag{1.2}$$

$$FA = \sqrt{\frac{3}{2}} \frac{\sqrt{(\lambda_1 - MD)^2 + (\lambda_2 - MD)^2 + (\lambda_3 - MD)^2}}{\sqrt{\lambda_1^2 + \lambda_2^2 + \lambda_3^2}}. \tag{1.3}$$

Enquanto a difusividade média (MD) corresponde a um terço do traço do tensor e dá a idéia da quantidade de difusão naquele voxel, a anisotropia fracional (FA) é uma medida da razão entre os autovalores do tensor e pode ser interpretada como a forma do elipsóide que representa o tensor. FA tende a 1 quando o elipsóide é mais alongado, significando que a difusão tem uma direção preferencial. E tende a 0 quando o elipsóide se aproxima de uma esfera, indicando que a difusão naquele voxel não possui direção preferencial, ou seja, é isotrópica.

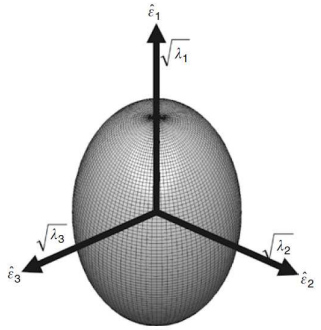

Fig. 1.1: Representação de um tensor por um elipsóide

Algumas medidas ainda, como o produto escalar (DP) e índice de coerência (CI), baseiam-se apenas nos autovetores dos tensores:

$$DP(\mathbf{T}_A, \mathbf{T}_B) = |e_{1,A} \cdot e_{1,B}|, \tag{1.4}$$

$$CI(\mathbf{T}_A) = \frac{1}{8}\sum_{j=1}^{8} |e_{1,A} \cdot e_{1,j}|, \tag{1.5}$$

onde $j = 1, 2, ...8$ indica cada um dos oito vizinhos de A. Somente uma minoria leva em conta autovalores e autovetores simultaneamente, como por exemplo o produto escalar tensorial (TDP) e a Norma de Frobenius (FN):

$$TDP(\mathbf{T}_A, \mathbf{T}_B) = \mathbf{T}_A : \mathbf{T}_B = \sum_{k=1}^{3}\sum_{l=1}^{3}(\sqrt{\lambda_{k,A}}\sqrt{\lambda_{l,B}}(e_{k,A} \cdot e_{l,B})^2, \tag{1.6}$$

$$FN(\mathbf{T}_A, \mathbf{T}_B) = \sqrt{tr(T_A - T_B)^2}. \tag{1.7}$$

Além disso, pouquíssimas são as medidas que levam em conta a difusão em uma vizinhança. Nesse caso, a vizinhança utilizada costuma ser bidimensional, vizinhança 8.

1.3.3 *Watershed* hierárquico

A transformada de *watershed* é uma ferramenta de morfologia matemática para segmentação de imagens [Beucher and Meyer, 1992]. Uma forma fácil de se entender a transformada de *watershed* por marcadores é compará-la a um processo de inundação, onde a imagem pode ser vista como uma superfície topográfica, cuja altitude corresponde ao nível de cinza. Quando buracos são abertos em alguns pontos marcados da imagem, água colorida começa a subir por estes buracos, sendo que cada cor está associada a um buraco (marcador). A medida que a inundação vai ocorrendo, barragens são construídas cada vez que águas de cores diferentes se encontram, de forma a mantê-las separadas. Estas barragens são as linhas do *watershed* e os lagos coloridos são as regiões resultantes da segmentação da imagem (Fig. 1.2).

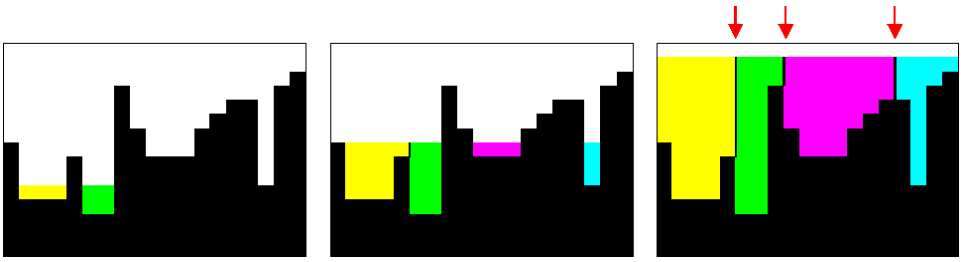

Fig. 1.2: Ilustração da transformada de *watershed* através da analogia com um processo de inundação

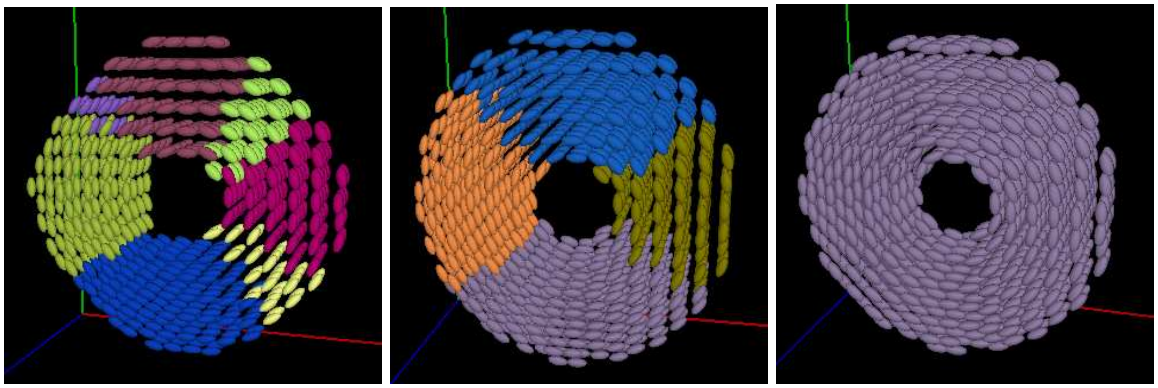

(a) Super-segmentação (b) $n = 5$ (c) $n = 2$

Fig. 1.3: Segmentação de uma imagem sintética de tensores de difusão nas n regiões mais significativas usando o *watershed* hierárquico

Ao contrário do *watershed* por marcadores descrito acima, no *watershed* clássico não há escolha explícita de marcadores. Neste caso, os marcadores são os mínimos regionais da imagem. A aplicação deste tipo de *watershed* normalmente resulta em uma super-segmentação da imagem e, na grande maioria das vezes, não é útil na resolução de problemas reais. Para obter um resultado de segmentação satisfatório, geralmente os mínimos regionais precisam ser filtrados segundo algum critério. A escolha deste critério de filtragem está diretamente relacionada com a imagem que se deseja segmentar.

Nesta tese, é usada uma variante do *watershed*, denominado *watershed* hierárquico, onde os marcadores são escolhidos usando-se o critério do valor de extinção dos mínimos regionais. Em outras palavras, após o cálculo dos mínimos regionais, foram utilizados como marcadores para o *watershed* os "n" mínimos regionais com os maiores valores de extinção segundo o critério de volume [Dougherty and Lotufo, 2003]. Deste modo, estamos segmentando a imagem nas n regiões mais significativas (Fig. 1.3).

1.4 Contribuições desta tese

1.4.1 Gradiente morfológico tensorial (Capítulo 2) e outras medidas escalares (Capítulo 5)

Com o objetivo de propor uma medida escalar extraída das imagens de tensores de difusão que retivesse o máximo de informação possível para permitir a segmentação , pensou-se em uma medida baseada nas dissimilaridades na vizinhança (de preferência, tridimensional). Assim chegou-se ao

gradiente morfológico tensorial (TMG), inspirado no conceito do gradiente morfológico adaptado para imagens tensoriais. O TMG pode ser definido como:

$$\nabla_B^T(f)(x) = \bigvee_{y,z \in B_x} d_n(\mathbf{T}_y, \mathbf{T}_z), \tag{1.8}$$

$\forall x \in E$, onde d_n representa uma medida intervoxel, $B \subset E$ é o elemento estruturante, $\mathbf{T}_y$ e $\mathbf{T}_z$ são tensores que representam a difusão em y e em z, respectivamente (y e z estão na vizinhança de x, definida por B_x). ∇_B^T é o TMG proposto. Enquanto o gradiente morfológico é dado pela dilatação menos a erosão, que no caso mais simples, é uma diferença entre a filtragem de ordem de máximo menos a de mínimo, na proposta do TMG, busca-se o máximo das diferenças ou dissimilaridades entre os voxels vizinhos.

Além do gradiente tensorial morfológico, propusemos uma classe de medidas intervoxel geradas a partir do cálculo do gradiente morfológico de medidas intravoxel. Ou seja, primeiramente o mapa escalar é calculado e em seguida o gradiente morfológico é aplicado a este mapa escalar.

1.4.2 Segmentação de imagens coloridas (Capítulo 2)

O objetivo principal do trabalho era segmentar as imagens de tensores de difusão do cérebro e, logo de início, ficou claro que os três principais desafios seriam: a dificuldade de adquirir, por falta de equipamento, imagens de tensores de difusão do cérebro; a dificuldade de trabalhar com estas imagens tensoriais; a falta de um padrão ouro para validar os eventuais resultados de segmentação que obtivéssemos. Percebemos que o ideal seria, então, começar com imagens tensoriais mais simples e cujos resultados de segmentação já fossem conhecidos.

Assim surgiu a idéia de criar uma representação tensorial para imagens coloridas, e então usá-las para testar as soluções propostas. A primeira representação tensorial baseou-se no modelo de cor HSL e criou uma correspondência entre os componentes HSL que definem cada cor (tonalidade, saturação e luminância) e os atributos de uma elipse (orientação, anisotropia e traço). A tonalidade (hue) é interpretada como a orientação do tensor (dada pelo autovetor principal), a saturação da cor passa a ser a anisotropia do tensor (razão entre os autovalores) e o tamanho (traço) do tensor é dado pela luminância. Esta representação está ilustrada na Fig. 1.4.

Desta forma, cada cor da imagem passa a ser representada por um tensor, como ilustra a Fig. 1.5. A partir desta representação, realizou-se o cálculo do TMG e subsequente segmentação utilizando-se o *watershed* hierárquico, como mostrado na Fig. 1.6.

Variantes da representação tensorial proposta foram testadas, utilizando-se desta vez outros modelos de cores, como o modelo RGB e CIELUV. Exaustivos experimentos foram realizados, combinando-se os modelos de cores e as medidas intravoxel utilizada no cálculo do TMG. De maneira

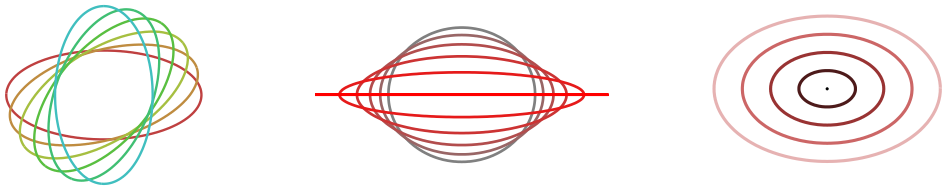

(a) Tonalidade (b) Saturação (c) Luminância

Fig. 1.4: Representação tensorial: cores *versus* elipses

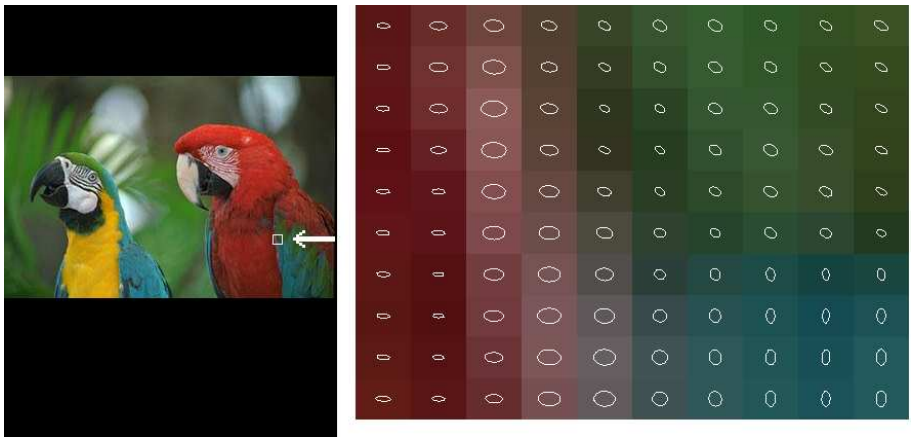

Fig. 1.5: Um exemplo de representação tensorial

(a) TMG (b) *watershed*

Fig. 1.6: Cálculo do TMG e segmentação resultante usando a Norma de Frobenius

geral, embora diversas combinações foram capazes de realizar a segmentação das imagens coloridas, a superioridade da Norma de Frobenius associada à representação tensorial das cores a partir do modelo HSL ficou demonstrada, tanto qualitativa quanto quantitativamente.

A análise qualitativa das imagens segmentadas foi bastante facilitada pela adoção do *watershed* hierárquico para segmentar as imagens estudadas. Ao fixar o número de regiões em que a imagem deveria ser segmentada, os resultados de segmentação obtidos por mapas escalares distintos puderam ser mais facilmente comparados quanto à preservação das regiões mais significativas da imagem.

A proposta desta representação tensorial nos permitiu desenvolver uma estratégia para segmentação de imagens coloridas, que se mostrou bastante competitiva, quando comparada com outras técnicas de segmentação.

1.4.3 Segmentação de imagens de tensores de difusão sintéticas e de phantom (Capítulo 3)

O método de segmentação proposto baseado no TMG foi então testado em imagens de difusão geradas sinteticamente, ou ainda, adquiridas de phantom construído com espinha dorsal de ratos. Este tipo de imagem permitiu verificar diferenças conceituais entre as diversas medidas intervoxel adotadas, bem como experimentar a utilização de diferentes elementos estruturantes responsáveis pela definição de vizinhança, no cálculo do TMG.

Os resultados obtidos pela utilização do *watershed* nas imagens de TMGs calculadas mostrou que o método proposto realmente tinha a capacidade de segmentar imagens de tensores de difusão, desde que a medida intervoxel e o elemento estruturante fossem corretamente escolhidos, de acordo com as características das estruturas que se quer segmentar. Um exemplo da adequação da medida intervoxel à imagem a ser segmentada pode ser visto na Fig. 1.7. Enquanto que para o torus sintético, ambas medidas foram capazes de preservar a borda do torus no cálculo do TMG, no caso do phantom, o

produto escalar não consegue preservar a informação necessária para a etapa de segmentação. Neste caso então, a norma de Frobenius seria a única a permitir a segmentação correta pela aplicação do *watershed* na imagem do TMG calculado.

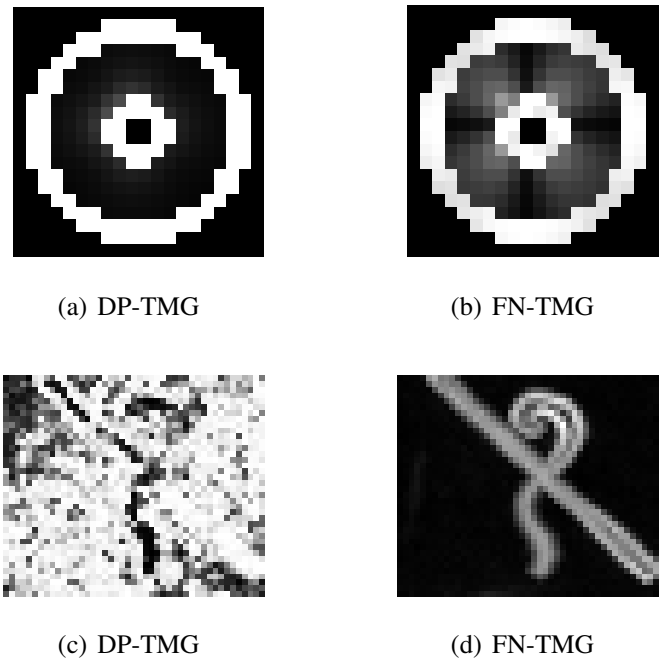

(a) DP-TMG (b) FN-TMG

(c) DP-TMG (d) FN-TMG

Fig. 1.7: TMG calculado para o torus sintético e para o phantom, utilizando o produto escalar (DP) e a norma de Frobenius (FN)

1.4.4 Segmentação de imagens de tensores de difusão do cérebro (Capítulo 4 e Capítulo 6)

Por último, foram realizados diversos experimentos de segmentação de estruturas do cérebro, utilizando-se as medidas escalares propostas e a transformada de *watershed*. A técnica de segmentação proposta foi testada tanto em estruturas de substância branca, quanto substância cinzenta do cérebro, mostrando que o método independe do tipo de tecido a ser segmentado. Até regiões que contém apenas fluído cérebro-espinhal foram segmentadas com sucesso.

As medidas escalares já existentes, apesar de úteis no estudo de patologias e na caracterização das estruturas, se mostraram adequadas para a tarefa de segmentação apenas em casos isolados, onde a estrutura a ser segmentada apresenta características de difusão completamente distintas das estruturas que a cercam (Fig. 1.8 e Fig. 1.9). Já as medidas propostas, baseadas na morfologia matemática, mostraram-se mais genéricas, sendo capazes de detectar bordas entre regiões com características de difusão similares (Fig. 1.10).

A necessidade de escolher a medida escalar a ser usada de acordo com as características da estrutura que se quer desejar ficou evidente nos estudos realizados. Medidas como o DP e o TDP, incapazes de distinguir diferenças entre tensores com a mesma orientação, mesmo que com anisotropia e/ou traço distintos, preservaram toda a borda do corpo caloso. Isso porque os tensores de difusão do corpo caloso estão fortemente alinhados e sua orientação difere da orientação dos vizinhos.

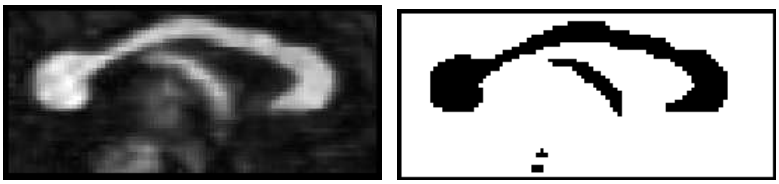

(a) *FA* (b) *FA* + limiarização

Fig. 1.8: Segmentação do corpo caloso aplicando uma limiarização em *FA*

Outra medida que apresentou bom desempenho foi a norma de Frobenius (FN), quando usada no cálculo do TMG, apesar de não invariante a rotação. Ou seja, a FN não é capaz de detectar bordas entre tensors perpendiculares entre si e não alinhados com os eixos xy. Apesar disso, ela conseguiu detectar bordas em todas as estruturas cerebrais estudadas, provavelmente porque em imagens reais é difícil encontrar objeto e fundo com tensores uniformes e perpendiculares. Também é importante mencionar que seu comportamento linear com variações de anisotropia e traço fazem da FN a melhor medida para cálculo do TMG e posterior segmentação via *watershed*.

Uma das aplicações escolhidas para validar o método de segmentação proposto foi o problema dos núcleos do tálamo. A segmentação dos núcleos do tálamo é de extrema importância para neuro-cientistas e neuro-cirurgiões e sua solução através de imagens só passou a ser possível depois do surgimento da DTI. Até então, a divisão do tálamo em núcleos só era feita *post-mortem*.

Para segmentar os núcleos do tálamo usando o método proposto, primeiro foi necessário interpolar os dados de difusão, antes do cálculo dos tensores. Em seguida, um método de segmentação

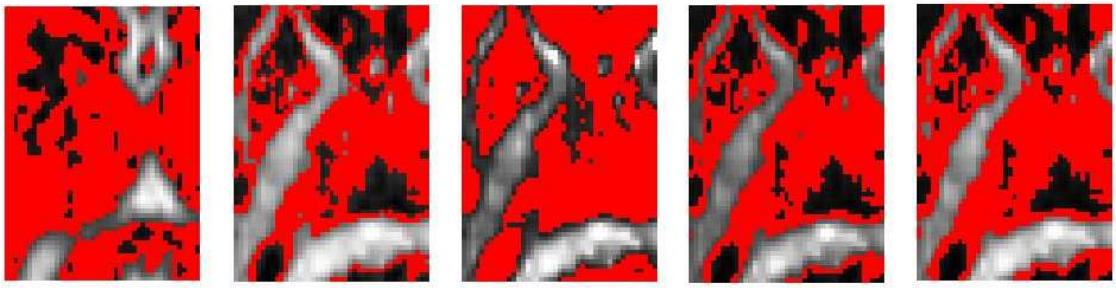

(a) MD+Th (b) FA+Th (c) VF+Th (d) sRA+Th (e) LI+Th

Fig. 1.9: Tentativa de segmentação do tálamo baseada em limiarização das medidas intravoxel

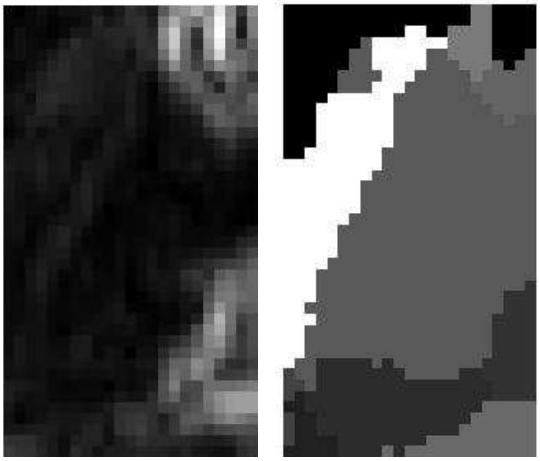

(a) TMG(FN) (b) *watershed*

Fig. 1.10: Segmentação baseada no TMG usando a norma de Frobenius e *watershed*

automática foi utilizado para encontrar a borda externa do tálamo. Esta borda foi então usada como marcador externo para o *watershed*, enquanto que os marcadores internos foram escolhidos pela dinâmica dos mínimos regionais. Os resultados obtidos pela técnica de segmentação proposta foram bastante surpreendentes, correspondendo à divisão do tálamo em núcleos descrita em atlas histológico (Fig. 1.11).

1.4.5 Ferramenta de visualização e segmentação de imagens de tensores de difusão do cérebro (Apêndice A)

No decorrer do desenvolvimento deste trabalho, ficou claro que além da dificuldade de processamento das imagens tensoriais, havia também a questão da visualização destas imagens, das etapas intermediárias, como o cálculo do TMG e da segmentação resultante.

Inicialmente, toda a visualização era feita através do MATLAB, o que limitava bastante a interpretação dos dados de difusão e dos resultados do processamento que estava sendo proposto. Como solução para essa limitação, desenvolveu-se um projeto de Iniciação Científica, vinculado a esta tese, cujo objetivo foi desenvolver uma ferramenta de visualização de imagens de tensores de difusão. Na verdade, além de visualização, a ferramenta desenvolvida implementou todas as etapas do método de segmentação proposto. Fig. 1.12 mostra a interface gráfica da ferramente desenvolvida.

A abordagem de visualização adotada permite a escolha, de forma independente, do modo de visualização dos tensores (caixas, elipsóides, tratos) e do mapa de cores associado (vinculado ou não à anisotropia). Além disso, permite a escolha da medida intervoxel, bem como do elemento estruturante, a ser utilizados no cálculo do TMG. O módulo de segmentação permite, além da escolha

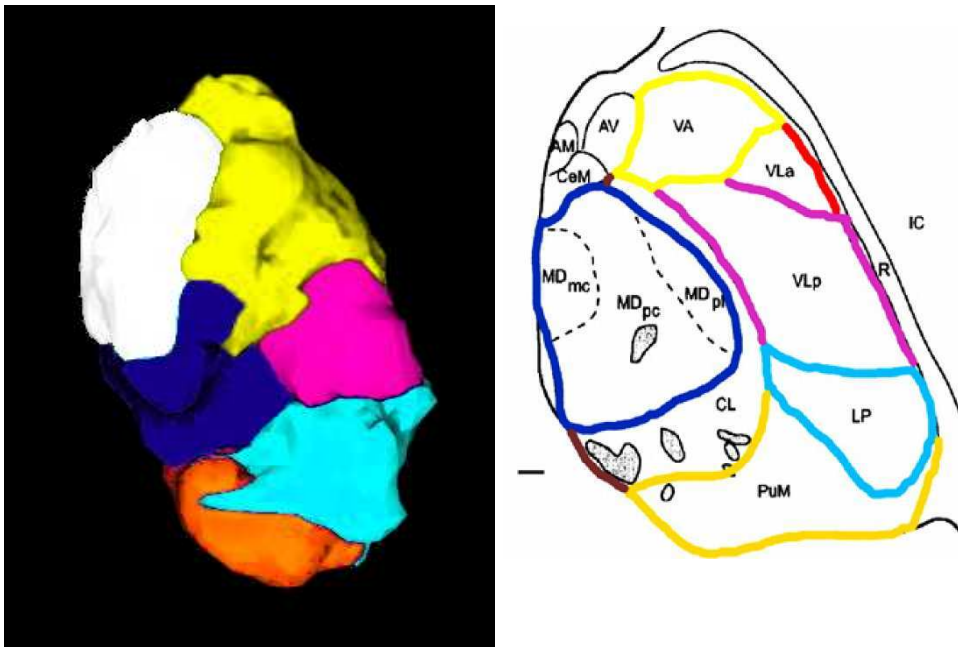

Fig. 1.11: Resultado da segmentação do tálamo obtido por watershed aplicado ao TMG (FN), comparado com os núcleos do tálamo em atlas histológico

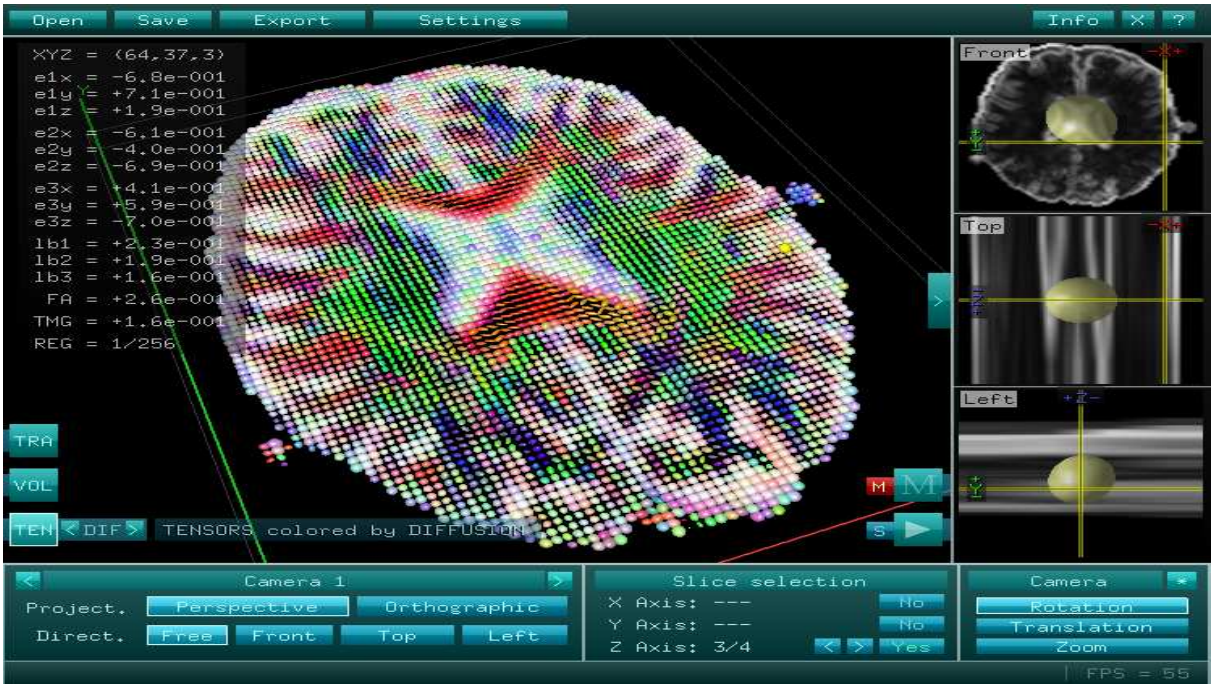

Fig. 1.12: Interface gráfica da ferramenta de visualização e segmentação

de marcadores automática, com ou sem filtragem dos mínimos regionais, uma escolha manual de marcadores. Finalmente, a ferramenta apresenta um módulo de animação, que simula o movimento das moléculas de água baseado na direção do autovetor principal dos tensores.

1.4.6 Algumas considerações

O método de segmentação de imagens de tensores de difusão baseada no TMG e na transformada de *watershed* mostrou-se capaz de segmentar os mais diversos tipos de imagens tensoriais (de imagens coloridas bidimensionais a imagens tridimensionais do cérebro). De maneira geral, a norma de Frobenius usada no cálculo do TMG levou aos melhores resultados de segmentação, apesar de não ser invariante à rotação. Isso se deve ao fato de a invariância à rotação ter se mostrado menos importante para o cálculo de um gradiente a ser usado na segmentação, do que a resposta linear às diferenças de anisotropia e traço.

Acredita-se que, uma nova medida de distância entre tensores que apresentasse uma resposta linear às diferenças de anisotropia e traço e ainda fosse invariante à rotação, levasse a resultados de segmentação ainda melhores. Propostas de novas medidas escalares de difusão, bem como novas técnicas de escolha de marcadores devem ser investigados em trabalhos futuros.

Apesar de termos conseguido uma boa segmentação das estruturas do cérebro, mesmo em problemas complexos como o dos núcleos do tálamo, ainda há necessidade de aumentar a robustez nas medidas, pois a relação sinal ruido ainda é baixa. Os bons resultados de segmentação obtidos em um conjunto de dados de difusão não se repetiram em outros conjuntos de dados, mesmo em dados adquiridos num mesmo indivíduo em instantes distintos.

Este trabalho faz parte do CInAPCe (Cooperação Interinstitucional de Apoio à Pesquisa sobre Cérebro), programa financiado pela Fapesp e coordenado pela Unicamp, que visa promover pesquisas em neurociências e formar uma rede de colaboração entre diversas instituições do Estado de São Paulo.

1.5 Organização da tese

O corpo desta tese é composto por cinco artigos em inglês, dois deles publicados em anais de congressos, um aceito para publicação em periódico de circulação internacional e outros dois já submetidos. Para facilitar a leitura da tese, cada capítulo contém um resumo introdutório do artigo apresentado na sequência. Como se tratam de artigos independentes, é inevitável a redundância de alguns conceitos e definições. Já as referências bibliográficas aparecem agrupadas no final da tese, exatamente para evitar repetições. A numeração das seções e figuras dos artigos foi unificada. Como

os artigos foram inseridos na íntegra, eventuais incorreções foram corrigidas e identificadas por notas de rodapé.

O Capítulo 2 apresenta uma abordagem tensorial para resolver problemas de segmentação de imagens coloridas. Ele inicia com a representação da imagem colorida por tensores, define o gradiente morfológico tensorial (TMG), inspirado na morfologia matemática e criado para detectar bordas em imagens tensoriais, e por fim apresenta os resultados dos experimentos de segmentação baseados no TMG e no *watershed* hierárquico.

Em seguida, o Capítulo 3 reapresenta o TMG e o método de segmentação proposto baseado no *watershed* hierárquico, desta vez aplicados às imagens de tensores de difusão sintéticas. A influência de diferentes medidas de similaridade e de diferentes elementos estruturantes é discutida.

Finalmente no Capítulo 4, a validação do método proposto se dá em imagens de tensores de difusão do cérebro. As imagens utilizadas nesta etapa foram adquiridas no Montreal Neurological Institute, McGill University, durante estágio de doutorado-sanduíche. Os resultados da segmentação baseada no TMG e em *watershed* são comparados com resultados de segmentação baseada em atlas. Além disso, o método proposto é também comparado com outros métodos de segmentação baseados em DTI, com relação à necessidade de inicialização e número de parâmetros a serem escolhidos.

Dois artigos ainda fazem parte desta tese. O primeiro deles pode ser visto no Capítulo 5, e trata de um estudo mais aprofundado das diversas medidas inter e intravoxel já propostas na literatura e sua utilidade na tarefa de segmentação. Em decorrência deste estudo, novos mapas escalares baseados em conceitos da morfologia matemática são propostos e analisados. Alguns destes mapas são utilizados na segmentação de estruturas do cérebro a partir de imagens de tensores de difusão.

Por último, o artigo apresentado no Capítulo 6 aplica o método de segmentação de DTI baseado em TMG e *watershed* hierárquico para segmentar os núcleos do tálamo.

Além dos artigos que fazem parte do corpo da tese, há ainda, no Apêndice A, um artigo que descreve o MM-DTI, uma ferramenta de visualização e segmentação de imagens de tensores de difusão. Tal ferramenta foi desenvolvida como parte de um projeto de Iniciação Científica para permitir a visualização dos resultados desta tese. Enquanto as imagens apresentadas nos Capítulos 2 e 3 desta tese foram geradas apenas com o MATLAB 7.0, as imagens dos Capítulos 4, 5 e 6 foram geradas com a ajuda da ferramenta desenvolvida.

Para facilitar a impressão da tese, todas as figuras foram inseridas em tons de cinza no corpo do texto. As figuras cujas cores têm significado importante e não podem ser simplesmente substituídas por níveis de cinza, foram repetidas, desta vez coloridas, nos Apêndices B–E.

Capítulo 2

Uma abordagem tensorial para imagens coloridas

Este capítulo contém o artigo intitulado "A tensorial framework for color images" [Rittner et al., 2009b], aceito para publicação pela *Pattern Recognition Letters*. Uma versão preliminar deste artigo [Rittner et al., 2007] foi publicada nos anais do XX Simpósio Brasileiro de Computação Gráfica e Processamento de Imagens - SIBGRAPI'07.

O artigo propõe uma nova representação para imagens coloridas, baseada na álgebra tensorial. A inspiração para tal proposta de representação veio das imagens de tensores de difusão por ressonância magnética. O primeiro passo proposto no artigo é representar as cores através de tensores. Assim sendo, uma cor originalmente representada por uma tupla de valores (por exemplo, *HSL* ou *RGB*) passa a ser representada por um tensor.

Uma vez tendo convertido a imagem colorida em uma imagem tensorial, o próximo passo é segmentar esta imagem aplicando conceitos da álgebra tensorial e usando métodos de segmentação já conhecidos, como por exemplo, a transformada *watershed*.

Um passo decisivo na segmentação por *watershed* é o realce de bordas, normalmente obtido através do cálculo do gradiente morfológico. Mas a questão é como calcular o gradiente morfológico para uma imagem tensorial. A solução que apresentamos neste artigo para resolver esta questão é a definição de um novo gradiente: o gradiente morfológico tensorial (TMG). O TMG é definido como o máximo das dissimilaridades calculadas entre todos os pares de tensores pertencentes à vizinhança, definida pelo elemento estruturante.

O artigo discute com detalhes a compatibilidade dos diversos modelos de cor existentes com a representação tensorial proposta. Também avalia a influência da medida de similaridade escolhida para o cálculo do gradiente morfológico no resultado final da segmentação. Análises qualitativas e quantitativas dos resultados da segmentação são apresentadas.

2.1 Abstract

This paper proposes a new tensorial color representation, obtained by making a correspondence between color models (*HSL*, *IHSL*, *HSV*, *RGB* and *CIELUV*) and tensors. Based on this representation, a proposed tensorial morphological gradient (TMG), defined as the maximum dissimilarity over the neighborhood, was tested using several tensor similarity measures. Experimental results illustrate which color models are more suitable to the proposed tensorial representation and which measures give best results in the TMG computation. The watershed transform was used to demonstrate that the proposed representation and the TMG can be applied to segment color images. A quantitative analysis of segmentation results was also conducted.

2.2 Introduction

The image edge enhancement by gradient computation is an important step in morphological image segmentation via watershed [Beucher and Meyer, 1992, Soille and Vincent, 1990, Falcão et al., 2004, Cousty et al., 2009]. For grayscale images, the morphological gradient [Dougherty and Lotufo, 2003] is a very good option and its computation is simple: for each point in the image, a structuring element is centered to it and the difference between the maximum and the minimum graylevels inside the structuring element is computed. For grayscale images, it is possible to compare the intensities among themselves in order to find the maximum and the minimum in a set of intensities. Such intensities are usually represented by integers, and the set of integers has a total order relation, i.e., any two integers are comparable and one of them is greater than or equal to the other one. The dissimilarity information exploited to compute the morphological gradient is the intensity difference among pixels inside the structuring element.

Color information lacks a total order relation - it is not possible to compare two colors, for instance red and blue, and conclude which of them is the greatest one. Therefore, such concept does not extend naturally to color images. Although the dissimilarity information is richer in color images than in grayscale ones, the design of methods to edge enhancement in color images is complex. Also note that if one considers the color space as a complete lattice [Talbot et al., 1998, Chanussot and Lambert, 1998], the order relation is not total and even if a total order is imposed to this space, it will be not natural for the human eye.

One option to construct color gradients relies on the design of measures to compute them [Flores et al., 2004, Flores et al., 2006]. Such measures exploit the dissimilarity information in color images, usually collected from each band, and then compute the gradient based on the distance of the colors inside a given connected region: the higher the dissimilarity among the colors inside

this region, the higher is its gradient. The dissimilarity measures impose a total order relation and the gradient may be computed.

An alternative measure is the one based on tensorial algebra [Danielson, 2003, Bishop and Goldberg, 1980]. Using tensors to represent colors in images bring us the possibility to make use of all the tensor theory. Given a tensorial representation of colors, it is possible to compute the gradient of a color image by computing the dissimilarity among the tensors. Some approaches of color representation based on tensors can be found in the literature. The gradient of Di Zenzo [Zenzo, 1986] is a well known application of tensor to compute color gradient. Others utilize the Structure Tensor (or a modified version of it) to represent *RGB* color images and use this representation to comply different tasks, such as: feature extraction [van de Weijer and Gevers, 2004, van de Weijer et al., 2006], computation of optical flow [Bigün et al., 1991] and segmentation [de Luis Garcia et al., 2005].

This paper proposes a new tensorial framework for color images. Based on a tensorial representation of color images using the *HSL* color model [Rittner et al., 2007], new color representations are obtained by building a correspondence between some color models and tensors. The tensorial morphological gradient (TMG) for color images is also a new proposal to compute color gradients based on tensorial algebra. Several ways to compute the dissimilarity between tensors have been published [Pierpaoli and Basser, 1996, Alexander et al., 1999, Jones et al., 1999, Basser and Pajevic, 2000, Wiegell et al., 2003, Ziyan et al., 2006, Pennec et al., 2006]. Six of them are used in this work to compute the tensorial morphological gradient.

Previously, the TMG was applied to compute gradients of diffusion tensor images and segment them [Rittner and Lotufo, 2008]. Now, segmentation of color images is performed using the watershed transform on the computed TMG. Quantitative analysis is conducted to compare segmentations obtained by different TMGs.

This paper is organized as follows: Section 2.3 describes the proposed tensorial representation of color images based on *HSL* color model. Section 2.4 discusses the behavior of the proposed representation applied to other color models. Section 2.5 presents dissimilarity measures commonly used to compare tensors and introduces the TMG, based on tensors and their dissimilarities. Section 2.6 compares the segmentation results obtained by watershed applied on several TMGs, obtained by different combinations of color model representation and similarity functions. Finally, Section 2.7 concludes the paper.

2.3 Tensorial representation of color images based on *HSL* color model

A tensor is the mathematical idealization of a geometric or physical quantity whose analytic description, relative to a fixed frame of reference, consists of an array of numbers. In other words, it is an abstract object expressing some definite type of multi-linear concept. Their well-known properties can be derived from their definitions and the rules for manipulation of tensors arise as an extension of linear algebra to multilinear algebra [Danielson, 2003].

Our tensorial framework for color images is based on second order tensors. In practice, a bi-dimensional second order tensor is denoted by a 2×2 matrix of values:

$$\mathbf{T} = \begin{pmatrix} T_{11} & T_{12} \\ T_{21} & T_{22} \end{pmatrix}, \tag{2.1}$$

and can be reduced to principal axes (eigenvalue and eigenvector decomposition) by solving the characteristic equation:

$$\mathbf{T} - (\lambda \cdot \mathbf{I})e = 0, \tag{2.2}$$

where $\mathbf{I}$ is the identity matrix, λ are the eigenvalues of the tensor and e are the normalized eigenvectors. If the tensor is symmetric, i.e., $T_{12} = T_{21}$, the eigenvalues will always be real. Moreover, the corresponding eigenvectors are perpendicular [Bishop and Goldberg, 1980]. In this case, the tensor can be represented by an ellipse, where the main axes lengths are proportional to the eigenvalues λ_1 and λ_2 ($\lambda_1 \geq \lambda_2$) and their direction correspond to the respective eigenvectors (Fig. 2.1).

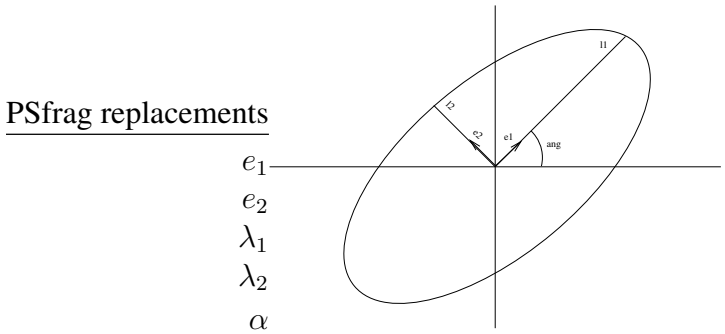

Fig. 2.1: Ellipse representing a tensor

It is possible to describe an ellipse by choosing its attributes from the corresponding tensor. The ratio between eigenvalues of a tensor determines the shape (eccentricity) of the ellipse that represents

it, their sum defines the scale (also called trace) of the ellipse and its principal eigenvector direction defines the angle of the ellipse in relation to the reference axis. Put differently, for a given 2×2 tensor, the shape and trace of the ellipse can be calculated as follows:

$$\text{Shape} = 1 - \frac{\lambda_2}{\lambda_1}, \tag{2.3}$$

$$\text{Trace} = (\lambda_1 + \lambda_2). \tag{2.4}$$

By establishing a relationship between the ellipse attributes (principal eigenvector direction, shape and trace) and the attributes of the *HSL* color model (hue, saturation and luminance), it is possible to represent a color in terms of a tensor [Rittner et al., 2007]. In other words, interpreting the hue of a color as the principal eigenvector direction (PED) of the tensor, the saturation as the shape of the ellipse and the luminance as the trace, for each color of the *HSL* model there will be a tensor for its description. Fig. 2.2 depicts this representation proposal.

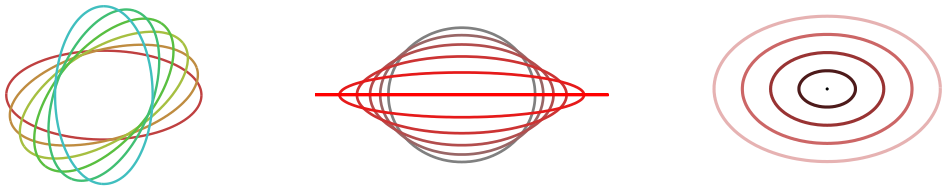

(a) Hue (b) Saturation (c) Luminance

Fig. 2.2: Tensorial representation of *HSL* color information

Fig. 2.2(a) shows the tensorial representation of different colors $(0 \leqslant h \leqslant \pi/2)$, with same saturation $(s = 0.5)$ and same luminance $(l = 0.5)$. Starting at red color $(hue = 0)$, represented by an ellipse oriented along the horizontal axis, changes in color (hue) keeping the same saturation and luminance cause changes only in the orientation of the ellipse. Fig. 2.2(b) depicts colors with same hue $(h = 0)$ and luminance $(l = 0.5)$ and different saturation values $(0 \leqslant s \leqslant 1)$. In this case, changes in saturation determine changes in the shape of the ellipse. The more saturated is the color, the more elliptical is the tensor that represents it. In one extreme $(s = 1)$, the color (red) is represented by a line segment. In the other extreme, color with no saturation (grayscale) is represented by a circle $(s = 0)$, meaning that the orientation of the ellipse (h) does not matter. Finally, Fig. 2.2(c) presents colors with fixed hue $(h = 0)$ and saturation $(s = 0.5)$ and luminance varying between 0 and 1 $(0 \leqslant l \leqslant 1)$. Colors with null luminance (black) are represented by a point. Once again the orientation of the ellipse (h) does not matter. As the luminance rises, the trace of the ellipse also

grows (without changing its shape).

Fig. 2.3 illustrates the proposed tensorial representation of colors through an example. Color information, given by its red, green and blue components (under the *RGB* color model) or by its hue, saturation and luminance values (under the *HSL* color model), is now represented by a tensor. This tensor is described in terms of ellipses attributes: PED, shape and trace. Fig. 2.3(b) depicts the tensorial representation for a small region indicated by a white square in the original image (Fig. 2.3(a)). For each pixel of the selected region there is an ellipse representing the tensor that describes its color.

(a) Selected region in the original image

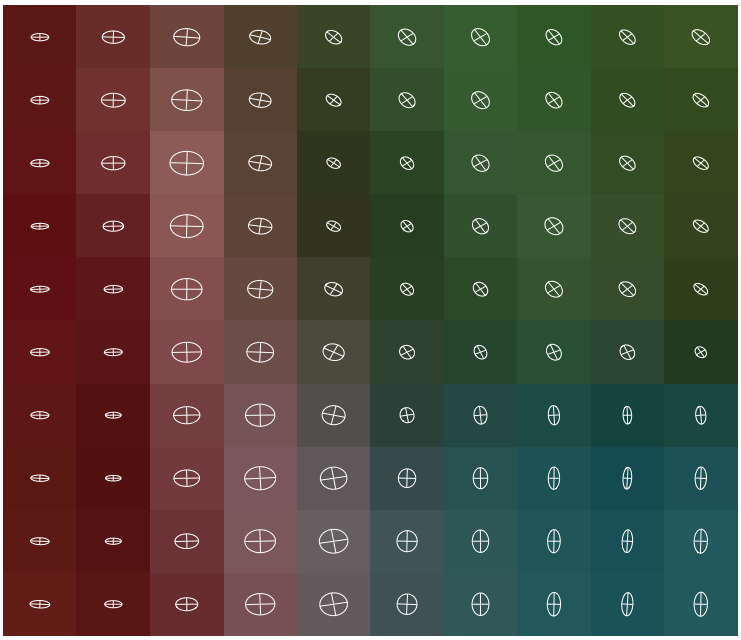

(b) Tensorial representation of colors for the selected region

Fig. 2.3: Example of the tensorial representation of a color image

Looking carefully, it is possible to distinguish four major regions in Fig. 2.3(b): a red region in the left side, a green region in the upper right corner, a blue one, in the bottom right corner and a transition

region in the middle of the figure. Ellipses in the red border (left side) of Fig. 2.3(b) are similar in shape, size and PED. They represent colors with high saturation (ellipses with high eccentricity) and relative low luminance (small ellipses). In the green border (up right) ellipses are similar in shape and size to the ones in the red region. This means that the saturation and luminance of the green pixels are similar to the red ones. The only difference between the ellipses representing them are their PED, responsible to define the color (in this case, red or green). The bottom right[1] corner contain bigger and less eccentric ellipses, indicating that the blue represented by them is not so saturated and more intense. Their PED are different too, corresponding to the blue color. The fourth region can be found moving toward the center of Fig. 2.3(b), where the ellipses become more circular, losing therefore its principal direction. That is because they are responsible for the transition effect between the three other regions and represent less saturated colors (almost achromatic ones).

2.4 Tensorial representation of color images based on other color models

A color model is an abstract mathematical model describing the way to represent a color using a tuple of numbers, typically as three or four values or color components. There are a considerable number of color models in common usage depending on the particular industry and/or application involved. For example, human vision determines color by parameters such as brightness, hue, and saturation. On computers it is more common to describe color by three components, normally red, green, and blue. Another similar system geared more towards the printing industry uses cyan, magenta, and yellow to specify color [Gonzalez and Woods, 1992].

Although the tensorial representation proposed in Section 2.3 was first designed for color images using the *HSL* color model [Rittner et al., 2007], any other color model with three color components could be used. By creating a direct correspondence between the ellipse attributes and the color model components, any color described by the chosen color model can be represented by a tensor. But, some color models are more suitable to the tensorial representation than others. Because of the angular attribute of the ellipse (PED), any color model that has an angular component (hue, for example, in *HSL* color model) is more likely to be well represented by an ellipse.

In order to extend the tensorial representation concept to other color models it suffices to establish a relation between the ellipse attributes (PED, shape and trace) and the attributes of the desired color model. In the case of the *HSV* and *IHSL* color models, hue, saturation and value (or luminance) have to be associated to PED, shape and trace, respectively. The *HSV* (hue, saturation, value) can

[1] errata: “right” substitui “left” (versão publicada)

be thought of conceptually as an inverted cone of colors (with a black point at the bottom, and fully-saturated colors around a circle at the top). The *IHSL* color model was proposed by Hanbury [Hanbury, 2003] to guarantee that the saturation is independent of the brightness and it is low-valued for all achromatic colors, since it does not occur in cylindrically-shaped versions of the *HSL* and *HSV* spaces. While hue in *HSL*, *HSV* and *IHSL* refers to the same attribute, their definitions of saturation differ dramatically. Nevertheless, results obtained using any of these three color models are quite similar for tensorial representation purposes and their nuances will not be discussed here.

Whereas for the above mentioned color models the extension of the proposed tensorial representation is obvious, for the *RGB* color model the correspondence is not well defined. Since it has no angular component, any of the three components, R, G or B can be chosen to be associated to PED, shape and trace. In this work, we defined the R component as the PED of the ellipse, the G component as the shape and the B component as the trace of the ellipse. When $R = 0$, the ellipse is oriented parallel to the horizontal axis, and as R grows to 255, the PED grows counterclockwise until π. Its important to notice that, while in the tensorial representation of *HSL*, the minimum and maximum values of color components are coherently represented by a point, a vector or a circle, in the tensorial representation of *RGB*, the meaning of minimum values is not translatable. Therefore, we had to avoid null tensors by fixing at 1 and 256 the limits of the *RGB* components associated with shape and trace of the ellipse. Otherwise, colors with $B = 0$ and different R and G components would be all represented by a point and colors with $G = 0$, same B and distinct R would be all represented by the same circle.

By changing the channel that corresponds to PED, to the shape or to the trace of the ellipse the tensorial representation of each individual color is modified, but the representation of a color image remains conceptually the same. Experiments with different correspondence between *RGB* components and ellipse attributes leaded to similar gradient and segmentation results. Also, the correspondence between the PED of the ellipse and the color component could be made differently: the minimum value of the color component could be assigned to a null PED (parallel to horizontal axis) and the maximum value of the color component could correspond to a PED equal to $\pi/2$ (parallel to vertical axis). This could solve the problem of two distinct colors being represented by the same ellipse. For example, a color with $R = 0$ and a color with $R = 255$ would be represented by the same tensor, since both PED$= 0$ and PED$= \pi$ lead to an ellipse horizontally oriented and would be represented by distinct ellipses if $R = 255$ corresponded to PED$= \pi/2$. In the other hand, distance between colors would be shortened and could deteriorate dissimilarity measurements.

Also for the *CIELUV* color model (L^* for luminance, u^*v^* - chromaticity space), the only obvious correspondence is between the luminance component and the trace of the ellipse. Since it has no angular component, the PED has to be associated to one of the chromaticity components: u^* or v^*.

In the experiments presented in this paper, the channel u^* was associated with the PED and the v^* channel was associated with the shape of the ellipse. The minimum value of u^* corresponds to a null PED (parallel to horizontal axis) while the maximum u^* is translated as PED$= \pi$. Inversion in this association ($u = shape$ and v^* =PED) does not change the overall results.

To better illustrate these possible extensions of the proposed tensorial representation, a synthetic color vector was created and represented using three different color models: *HSL*, *RGB*, *CIELUV* (Fig. 2.4).

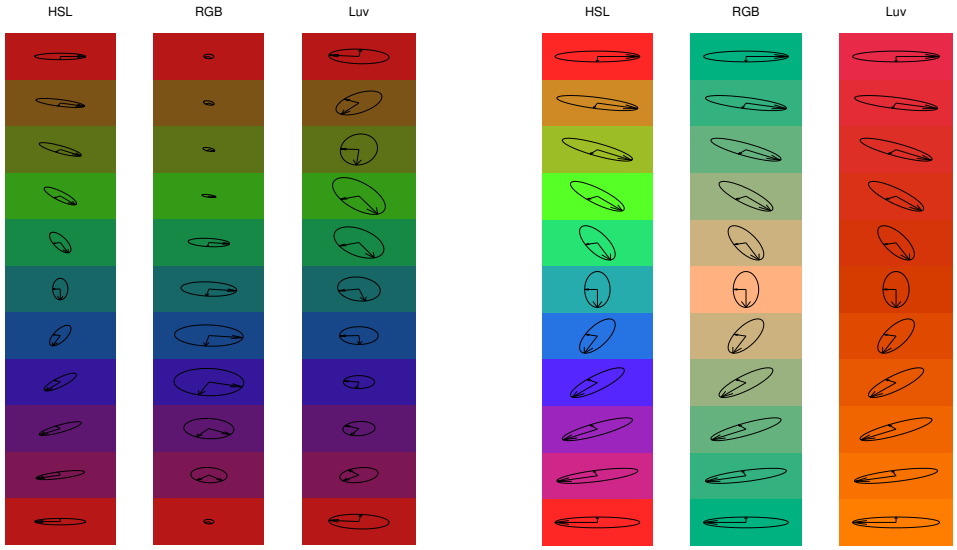

(a) Same colors (b) Same tensors

Fig. 2.4: Extension of the tensorial representation to different color models

Fig. 2.4(a) was obtained by creating a vector of colors originally in the *HSL* model, for which the saturation was set to 0.7, the luminance to 0.3 and the hue varied from 0 to 1 (in intervals of 0.1). Then, the respective color vector were converted to the two other color models (*RGB* and *CIELUV*) and a tensorial representation was obtained from the correspondence between the color components and the ellipse attributes. The established correspondence is indicated in Table 2.1. The result is a vector of fixed colors being represented by different tensors (depending on the chosen color model).

The first column is the original tensorial color representation, using the *HSL* color model, as presented in Section 2.3. In the second and third columns of Fig. 2.4(a) it is possible to observe that the obtained tensorial representations using the *RGB* and the *CIELUV* models do not demonstrate any coherence at first glance. But to affirm that these representation are not suitable for color images, it is necessary to analyze under what circumstances they would be used.

Tab. 2.1: Correspondence between ellipse attributes and color models components

	HSL	*HSV*	*IHSL*	*RGB*	*CIELUV*
PED	h	h	h	R	v^*
Shape	s	s	s	G	u^*
Trace	l	v	l	B	L^*

Similarly, first column of Fig. 2.4(b) was obtained setting saturation to 0.7 and luminance to 0.5 and varying hue from 0 to 1, in intervals of 0.1. Then, all others columns of Fig. 2.4(b) were obtained assigning the same values (0.7, 0.5 and from 0 to 1) to the first, second and third components of each color model. By doing so, the tensors are fixed and what changes are the colors represented by them. The resulting figure is composed of color tables in all three color models, generated by a single tensor color table.

Fig. 2.4(b) shows that the first color model (*HSL*) present some coherence in this tensor color table. One evidence is that the first and the last color of the first column are the same. This coherence is not preserved in the *RGB* model (Fig. 2.4(b) - second column), because when the PED varies from 0 to π, it means that the R component varies from 0 to 255. It explains why the first and the last color represented in the second column are not the same, as observed in the first column. As explained before, this could be overcome by modifying the representation of colors in *RGB* space (PED varying only between 0 and $\pi/2$), but this would cause very distinct colors to be represented by not so distinct tensors. The last column, the *CIELUV* model, shows also that the variation of π in the PED does not lead to a comprehensible color palette, since what is being changed is the v^* component, from 0 to 1.

Another way to visualize the differences between tensorial color representations based on different color models is to chose three different values for the hue component (for example: red, green and blue) and three different saturation levels for each one of the chosen hue ($s = 1$, 0.5 and 0.05). Then, the same nine resulting colors are represented by tensors using the tensorial color representation based on the three different color models previously described. Fig. 2.5 shows that the obtained tensorial representations are distinct in shape, orientation and scale. Nevertheless, some of them are intuitive or, at least, comprehensible whereas others seem uncorrelated or, at least, confusing.

By observing Fig. 2.5(a), for example, it is easy to notice that tensors representing colors with identical hue components present the same orientation. As the saturation decays, the tensor approximates to a circle.

Fig. 2.5(b) shows a completely distinct configuration, compared to the first representation. The R component corresponds to the PED, and is not trivial to infer which color has a higher R component just looking at the PED of the ellipses. The G component defines the shape of the ellipse, which explains why the green colors correspond to more elliptical tensors than the blue and red colors, represented by more circular tensors. Finally, the B component determines the trace of the ellipse.

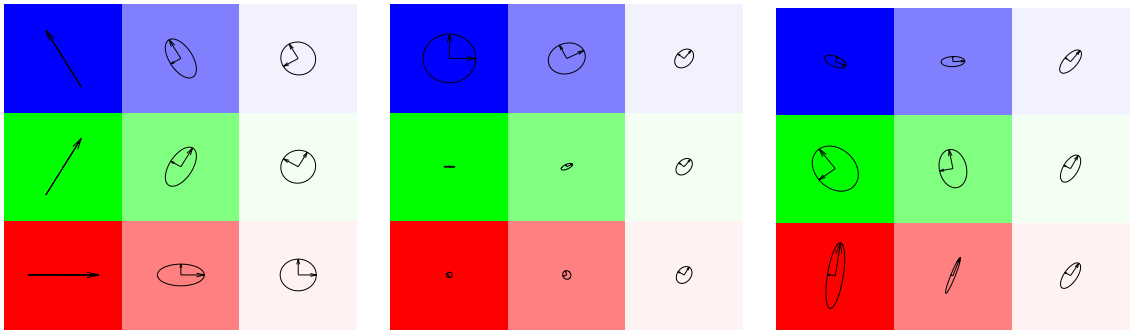

(a) *HSL* (b) *RGB* (c) *CIELUV*

Fig. 2.5: Tensorial representation of colors based on different color models

That is why the blue colors are represented by bigger tensors than the green and red tones.

The last representation (Fig. 2.5(c)) shows that the tensors obtained by the *CIELUV* color model present a coherence, although its interpretation is not intuitive. However, the validity of this color representation, as well as the remaining representations, can be confirmed after choosing a specific application and running some experiments.

2.5 Tensorial morphological gradient (TMG)

In the following we present several analysis and discussion about the choice of color models and tensorial metrics for computation of the tensorial morphological gradient. Subsection 2.5.1 describes some tensorial similarity measures. These measurements are discussed in Subsection 2.5.2 regarding to color comparison. The Tensorial Morphological Gradient (TMG) is proposed in Subsection 2.5.3, and the comparison of results achieved by the application of several similarity measures in TMG computations is shown in this Subsection as well.

2.5.1 Tensorial similarity measures

Although tensors are used in several different problems from geometry and physics, most of the tensor similarity measures discussed here derived from Diffusion Tensor Imaging (DTI) studies, a Magnetic Resonance Imaging (MRI) modality that became recently a powerful technique to investigate the tissue microstructure *in vivo* . Since a key factor in DTI analysis is the proper choice of the similarity measure to be used, several works have been published on the subject [Pierpaoli and Basser, 1996, Alexander et al., 1999, Jones et al., 1999, Ziyan et al., 2006, Basser and Pajevic, 2000, Wiegell et al., 2003, Pennec et al., 2006].

Given two tensors $\mathbf{T}_i$ e $\mathbf{T}_j$, the most simple comparison between two tensor quantities, used by [Ziyan et al., 2006] to segment the thalamic nuclei from diffusion tensor images, is the dot product between the principal eigenvector directions:

$$d_1(\mathbf{T}_i, \mathbf{T}_j) = |e_{1,i} \cdot e_{1,j}|, \tag{2.5}$$

where $e_{1,i}$ and $e_{1,j}$ are the principal eigenvectors of tensors $\mathbf{T}_i$ e $\mathbf{T}_j$, respectively. The absolute value of the dot product solves the problem with the sign ambiguity of the eigenvectors.

Another simple similarity measure, presented by [Pierpaoli and Basser, 1996] as an intervoxel anisotropy index and used by [Alexander et al., 1999], is the tensor dot product:

$$d_2(\mathbf{T}_i, \mathbf{T}_j) = \lambda_{1,i}\lambda_{1,j}(e_{1,i} \cdot e_{1,j})^2 + \lambda_{2,i}\lambda_{2,j}(e_{2,i} \cdot e_{2,j})^2. \tag{2.6}$$

In [Alexander et al., 1999] a number of tensor similarity measures are presented. Their purpose was to match pairs of diffusion tensor images (DTI) and the proposed measures were based on the diffusion tensor itself and indices derived from the diffusion tensor. One of the similarity measures proposed in that work was the following Euclidean distance measure:

$$d_3(\mathbf{T}_i, \mathbf{T}_j) = \sqrt{\text{Trace}((\mathbf{T}_i - \mathbf{T}_j)^2)}. \tag{2.7}$$

This similarity measure was also explored in other DTI studies under different names, such as generalized tensor dot product [Jones et al., 1999] and Frobenius Norm [Wiegell et al., 2003, Ziyan et al., 2006]. However, because affine invariance is a desirable property for segmentation purposes and the Frobenius Norm is not invariant to affine transformations, [Wang and Vemuri, 2005] proposed a novel definition of diffusion tensor "distance ", as the square root of the J-divergence of the corresponding Gaussian distributions, i.e.,

$$d_4(\mathbf{T}_i, \mathbf{T}_j) = \frac{1}{2}\sqrt{\text{Trace}(\mathbf{T}_i^{-1}\mathbf{T}_j - \mathbf{T}_j^{-1}\mathbf{T}_i) - 2n}. \tag{2.8}$$

Eq. 2.8 is not a true distance since it violates the triangle inequality, but it is in fact a computationally efficient approximation of Rao's distance [Wang and Vemuri, 2005]. More recently, a new approach for calculating tensor similarity has been adopted in DTI studies: the Log-Euclidean distances. Among the similarities measures proposed by [Arsigny et al., 2006], there is a measure very closely related to the Frobenius Norm, called the similarity-invariant Log-Euclidean distance, defined as:

$$d_5(\mathbf{T}_i, \mathbf{T}_j) = \sqrt{\text{Trace}((\log(\mathbf{T}_i) - \log(\mathbf{T}_j))^2)}. \tag{2.9}$$

Contrary to the classical Euclidean framework on tensors, one can see from Eq. 2.9 that symmetric matrices with null or negative eigenvalues are at an infinite distance from any tensor. To overcome this problem, in this paper we replace $\log(\mathbf{T}_i)$ by $\log(100\mathbf{T}_i + 1)$ to avoid the computation of the logarithm of null values.

Another affine-invariant metric for statistical analysis and image processing of diffusion tensor data based on the Riemannian geometry was introduced independently by different authors, such as [Batchelor et al., 2005] and [Pennec et al., 2006]:

$$d_6(\mathbf{T}_i, \mathbf{T}_j) = \sqrt{\text{Trace}(\log(D_{ij})^2)}, \tag{2.10}$$

where D_{ij} is equal to $\mathbf{T}_i^{-\frac{1}{2}}\mathbf{T}_j\mathbf{T}_i^{-\frac{1}{2}}$.

It is important to notice that the above similarity measures are not the only ones proposed in the literature, nevertheless they were chosen to be part of this study because they come from different approaches and privilege some aspects of tensors. In [Peeters et al., 2008], a classification based on the nature of the derivation of the similarity measures was presented: measures based on scalar indices; measures that make use of the angles between eigenvectors; measures based on linear algebra; measures based on Riemannian geometry; measures considering the tensors as a representation of a probability density function and measures that combine different measures from the previous classes.

So, whereas the dot product is an angular difference, the tensor dot product and the Frobenius Norm come from linear algebra, the Log-Euclidean distance and the affine-invariant Riemannian metric is based on Riemannian geometry and the J-divergence derives from statistical considerations.

2.5.2 Colors similarities based on tensorial similarity measures

As pointed out in several DTI studies, each one of the tensorial similarity measures presented in Subsection 2.5.1 has its weaknesses. However, they were evaluated only for DTI segmentation purposes. None of them was analyzed under a color image gradient perspective. So, before introducing a new color gradient based on tensorial dissimilarities it is interesting to investigate the behavior of the presented similarity measures, regarding to color comparison. However, to generate the figures which show this behavior it has to be taken into account that the hue scale limits had to be changed from $(0 \leqslant h \leqslant 2\pi)$ to $(0 \leqslant h \leqslant \pi)$, to follow the limits of the PED. Because the PED of the ellipse indicates an orientation and not a direction, ellipses rotated $\pi/4$ or $5\pi/4$ from the origin, for example, are considered identical. Therefore, without changing the hue scale limits, colors with identical saturation and luminance components and diametrically opposing hue components would be represented by the same tensor.

Vertical axes represent the computed dissimilarities and horizontal axes represent the hue scale.

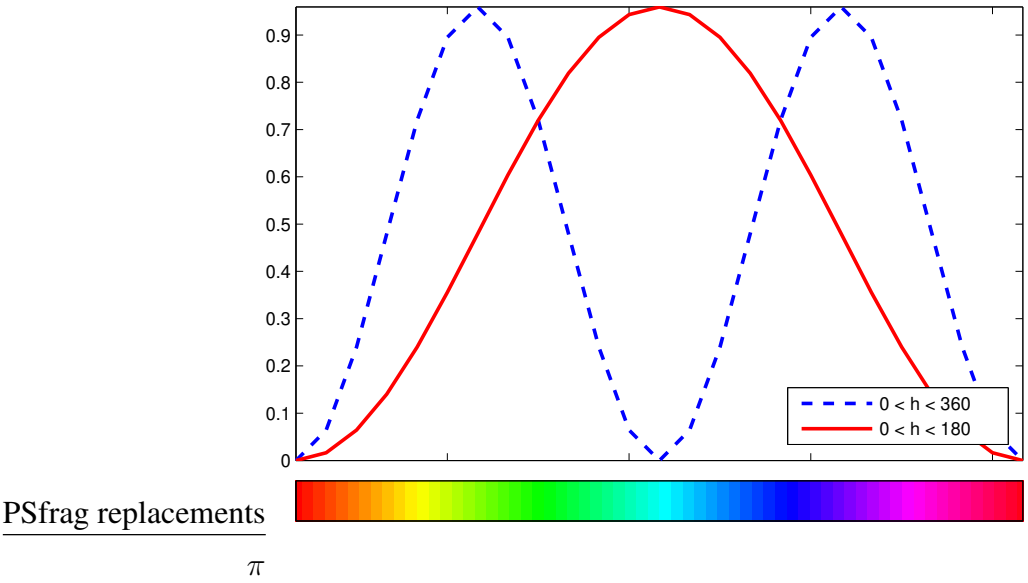

Fig. 2.6: Dissimilarity between colors comparing original and modified hue scale

According to Fig. 2.6, the red and the cyan colors are identical using the original hue scale limits (dashed blue curve), whereas adopting the modified hue scale (solid red curve), they present maximum dissimilarities.

Fig. 2.7, Fig. 2.8 and Fig. 2.9 depict the obtained dissimilarities when comparing colors under the *HSL* model using the six different similarity measures: dot product (DP), tensor dot product (TDP), Frobenius Norm (FN), J-divergence(J-div), Log-Euclidean distance (LogE) and affine-invariant Riemannian metric (Riem).

Fig. 2.7 shows all six similarity measures computed for colors with fixed saturation and luminance and variable hue. Vertical axes represent the dissimilarity between each color and the reference color. The differences presented in Fig.2.7(a)–(d) are due to different adopted reference colors. Whereas in Fig. 2.7(a) dissimilarities are computed between each color and the color red ($h_{ref} = 0$), dissimilarities are computed using as reference a color with $h_{ref} = \pi/6$ (yellow) in Fig. 2.7(b), $h_{ref} = \pi/4$ (yellow-green) in Fig. 2.7(c) and $h_{ref} = \pi/2$ (cyan) in Fig. 2.7(d).

So, given one curve in Fig. 2.7(a)($h_{ref} = 0$), two considerations can be made: it is expected that one similarity curve in Fig.2.7(a)–(d) would preserve the same shape as in Fig. 2.7(a) except for a translation in horizontal axes; and all colors which would present null dissimilarity to the reference would be the ones where $h = h_{ref} \pm \pi$. This two considerations are confirmed only for four of the six measures: DP, TDP, J-div and Riem. The other two measures, FN and LogE, do not confirm the expectations. Once h_{ref} grows from 0 to $\pi/2$, these two curves change from an unimodal (Fig. 2.7(a)) to a bimodal function (Fig. 2.7(b), Fig. 2.7(c) and Fig. 2.7(d)). This is because the Frobenius Norm, and as consequence, the Frobenius based Log-Euclidean distance, are not affine-invariant. Tensors

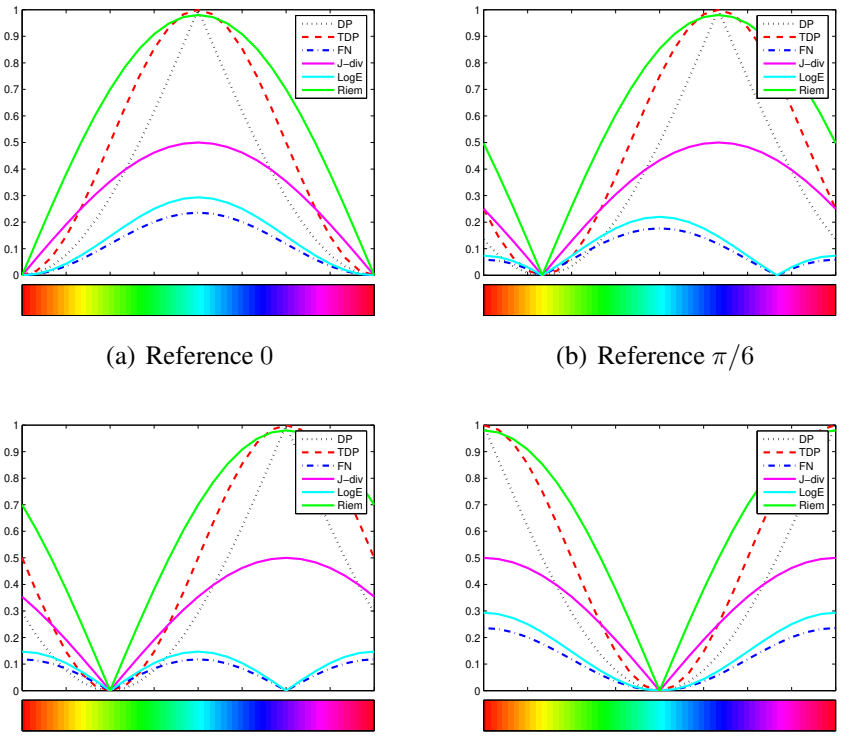

(a) Reference 0 (b) Reference $\pi/6$

(c) Reference $\pi/4$ (d) Reference $\pi/2$

Fig. 2.7: Dissimilarity between a tensor and a reference, computed for different reference angles and by different measures

aligned to cartesian axes are similar only to tensors pointing in same direction (angular distance = 0 or π), according to these measures. In contrast, tensors not aligned to cartesian axes are similar not only to tensors pointing in same direction (angular distance = 0 or π), but also in opposite direction (angular distance = $\pi/2$ or $3\pi/2$).

From Fig. 2.7 it is also possible to conclude which measure is more sensitive to small variations in colors (noise or perturbations introduced in the acquisition process) and which one is less sensitive. This can be inferred observing the derivative of each curve near the origin. The Riem and the J-div have the larger derivatives near the origin, therefore, they are more sensitive to any kind of perturbation. The LogE and the TDP are less sensitive to small variations than the J-div and the Riem, nonetheless have more sensitivity than the DP and the FN.

But even this sensitivity to noise changes, depending on the reference color. Fig. 2.7(b) shows that for a reference tensor with $h_{ref} = \pi/6$, the LogE turns out to be more sensitive to noise, followed by the FN, the J-div and the Riem. As a consequence, the TDP and the DP become the less sensitive measures. This change in sensitivity is a direct consequence of the FN not being affine-invariant, therefore, changing the curve derivative when the reference color is rotated.

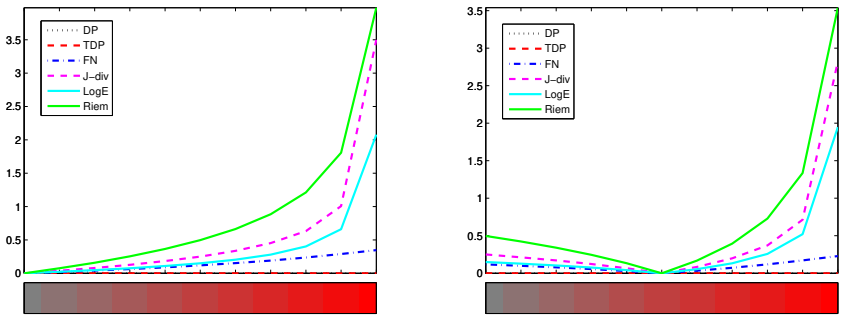

(a) Reference $s = 0$ (b) Reference $s = 0.5$

(c) Reference $s = 0.7$ (d) Reference $s = 1.0$

Fig. 2.8: Dissimilarity between a tensor and a reference, computed for different reference saturations and by different measures

Fig. 2.8 shows also all six similarity measures, this time computed for colors with fixed hue and luminance and variable saturation. Vertical axes represent the dissimilarity between each color and the reference color. Once again, the adopted reference color is different in each of the four plots (Fig.2.8(a)–(d)). Whereas in Fig. 2.8(a) dissimilarities are computed between each color and the red with null saturation ($s_{ref} = 0$), dissimilarities are computed using as reference a red color with $s_{ref} = 0.5$ in Fig. 2.8(b), $s_{ref} = 0.7$ in Fig. 2.8(c) and $s_{ref} = 1$ in Fig. 2.8(d).

The conclusion extracted from Fig. 2.8 is that measures like the DP and the TDP are not suitable for color comparison. Color with no saturation at all and full saturated are perfectly similar, according to these measures. In the other hand, the J-div, the LogE and the Riem measures present much higher derivatives in the right part of the plot ($s < 0.5$) than in the left part ($s > 0.5$). This characteristic is desirable when comparing diffusion tensors, where small saturation can be translated as low anisotropy and should be ignored in DTI analysis. But for color comparison, this increasing derivative causes a distortion in the obtained results.

Two colors with the same hue, same luminance and with a small difference in a high saturation, for example, $s = 0.9$ and $s = 0.95$ would be considered much more dissimilar by the J-div, the LogE

and the Riem measures than two other colors with the same hue, same luminance and the same small difference in a low saturation, for example, $s = 0.1$ and $s = 0.15$. That would not happen when comparing these two pairs of colors using the FN, since it presents a constant derivative, suggesting that the FN has the best behavior with respect to saturation differences.

Finally, Fig. 2.9 depicts the behavior of the similarity measures in the presence of variable luminance. The indicated figure was obtained fixing hue and saturation components and varying the luminance. Once again, vertical axes represent the dissimilarity between each color and the reference color and the adopted reference color is different in each of the four plots (Fig.2.9(a)–(d)). Whereas in Fig. 2.9(a) dissimilarities are computed between each color and the red with null luminance ($l_{ref} = 0$), dissimilarities are computed using as reference a red color with $l_{ref} = 0.5$ in Fig. 2.9(b), $l_{ref} = 0.7$ in Fig. 2.9(c) and $l_{ref} = 1$ in Fig. 2.9(d).

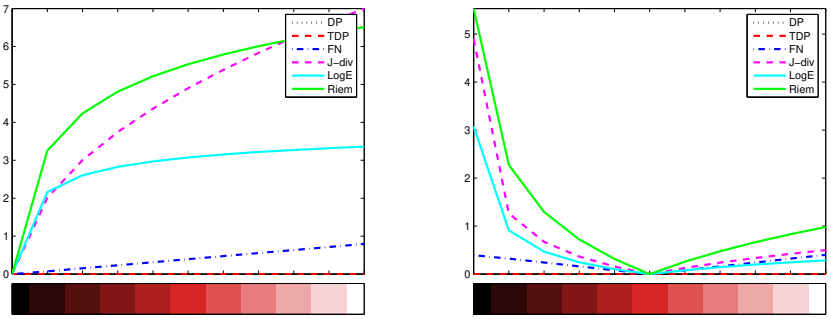

(a) Reference $l = 0$ (b) Reference $l = 0.5$

(c) Reference $l = 0.7$ (d) Reference $l = 1.0$

Fig. 2.9: Dissimilarity between a tensor and a reference, computed for different reference luminances and by different measures

Conclusions from Fig. 2.9 are similar to the ones presented for Fig. 2.8. The DP and the TDP do not seem to be ideal for color comparison, due to their null gain and the J-div, the LogE and the Riem measures, due to their decreasing derivative. The measure that presented better behavior regarding luminance variation in color comparison is the FN, because of its constant derivative.

Previous discussed plots were obtained fixing two parameters of the colors and changing only one (for example, fixed saturation and luminance and variable hue). To have a more complete idea of the behavior of the metrics applied to color comparisons, one should observe it by varying all parameters.

Fig. 2.10 depicts the Frobenius Norm computed between all colors and a chosen reference color. Axes correspond to the three color components - hue, saturation and luminance - varying from 0 to 1 [2]. The color inside the cube (grayscale) represents the computed dissimilarity, where black corresponds to null dissimilarity. Lighter the gray inside the cube, higher the dissimilarity. Although the cube is composed by several slices, only one slice per plane is shown, in order to make it more comprehensible. The lines drawn inside the cube are isocontours of the computed dissimilarity. The reference color is marked with a circle in the cube. The position of the circle is defined by its components (hue, saturation and luminance) and the color inside the circle corresponds to the reference color.

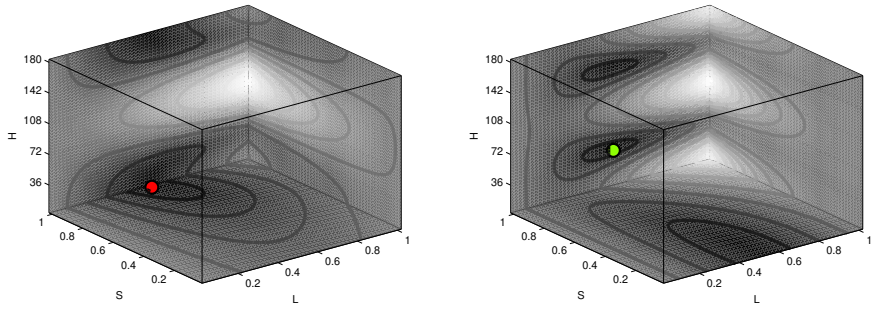

(a) FN ($h = 0$, $s = 1.0$, $l = 0.5$) (b) FN ($h = 0.25$, $s = 1$, $l = 0.5$)

Fig. 2.10: Dissimilarity between all colors and a reference, computed using the Frobenius Norm for two different color references ($h = 0$ and $h = \pi/8$)

Fig. 2.10(a) and Fig. 2.10(b) differ only by the color reference. While in Fig. 2.10(a) the color reference is a fully-saturated red ($h_{ref} = 0$, $s_{ref} = 1$ and $l_{ref} = 0.5$), in Fig. 2.10(b) the color reference is a fully-saturated green ($h_{ref} = \pi/8$, $s_{ref} = 1$ and $l_{ref} = 0.5$). Although these plots are far more complete and wide-ranged, its interpretation is much more complicate than the ones in Fig. 2.7, Fig. 2.8 and Fig. 2.9.

Fig. 2.11 was built the same way as Fig. 2.10, this time using the same color reference and computing the dissimilarities by three distinct measures: Fig. 2.11(a) shows the Frobenius Norm, Fig. 2.11(b) shows the Log-Euclidean distance and Fig. 2.11(c), the affine-invariant Riemannian metric. Once again, the purpose of inserting this plot is to show how complex this comparison can be.

[2]The hue scale was converted to degrees only to make the graph more intuitive.

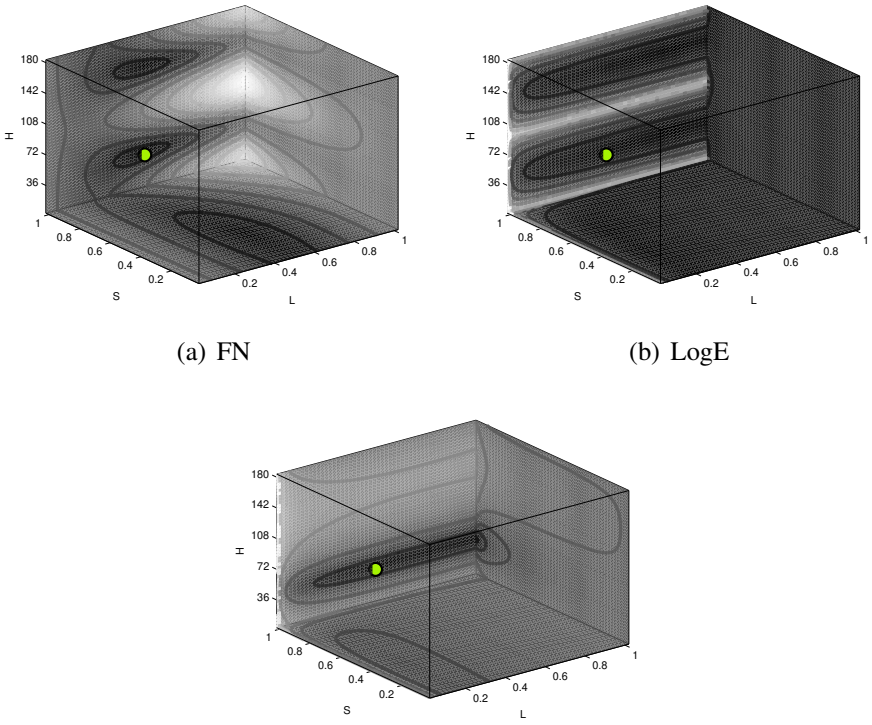

(a) FN (b) LogE

(c) Riemannian

Fig. 2.11: Dissimilarity between all colors and a reference ($h = \pi/8$, $s = 1$, $l = 0.5$), computed by different measures

In a recent study, [Peeters et al., 2008] classified and summarize the different measures that have been presented in diffusion tensor literature, and also presented a framework to analyze and compare the behavior of the measures according to several selected properties (size, shape, orientation, robustness and metric). The measures behavior were illustrated through several plots and required carefully careful[3] interpretation.

Despite the different applications of both studies (diffusion tensors versus tensors representing colors), results obtained here are consistent with conclusions in [Peeters et al., 2008]. According to Peeters *et al.*, the Frobenius Norm proved to be the most robust measure, and it states that although the FN measure is relatively simple, it showed good behavior. They show also that, when using measures like the J-div, the LogE and the Riem, one has to be careful with the sensitivity to small shape and size changes close to the degenerate cases.

[3]errata: “careful” substitui “carefully” (versão publicada)

2.5.3 Definition of the tensorial morphological gradient (TMG)

Let $E = \mathbb{Z} \times \mathbb{Z}$ be the set of all points in the color image f. The proposed TMG based on the tensorial representation of Section 2.3 is defined by

$$\nabla_B^T(f)(x) = \bigvee_{y,z \in B_x} d_n(\mathbf{T}_y, \mathbf{T}_z), \tag{2.11}$$

$\forall x \in E$, where d_n represents any of the similarity functions presented in Subsection 2.5.1, $B \subset E$ is a structuring[4] element centered at the origin of E, $\mathbf{T}_y$ is the tensor that represents the color in y, and $\mathbf{T}_z$ is the tensor that represents the color located in z (y and z are in the neighborhood of x, defined by B_x). ∇_B^T is the proposed TMG. Because the chosen measures are already comparisons between neighbors, the proposed gradient is not the difference between the maximum and the minimum values, but only the maximum value. In other words, the computed gradient in a neighborhood given by a structuring element is the maximum dissimilarity among all pairwise dissimilarities.

Fig. 2.12 depicts the original image and the TMGs computed by DP, TDP, FN, J-div, LogE and Riem. All gradients were computed using a 3×3 diamond structuring element and using the tensorial representation based on the *HSL* model and were negated for a better presentation. The gradients based on DP (Fig. 2.12(b)) and TDP (Fig. 2.12(c)) presented smoother borders and lost important parts (such as the left parrots head), therefore it is expected that the segmentation result provided by them will not be good. The borders in the TMG using the FN (Fig. 2.12(d)), the J-div (Fig. 2.12(e)), the LogE (Fig. 2.12(f)) and the Riem (Fig. 2.12(g)) were sharper and should provide better results in the application of watershed technique.

Fig. 2.13 contains TMGs computed by different measures and based on different color model representations. First row of the referred figure (Fig.2.13(a)–(c)) shows computed TMGs using the TDP measure, based in *HSL*, *IHSL* and *CIELUV* tensorial representations, respectively. Although all three gradients are similar, i.e., present the same borders of the original image, the first two (Fig. 2.13(a) and Fig. 2.13(b)) are much more stronger than the third one. This result can be explained by the nature of the TDP measure and the characteristic of the *CIELUV* color model. The TDP measure compares basically the eigenvectors directions of the tensors and in the *HSL* and the *IHSL* tensorial representation the eigenvectors directions have a significant meaning, due to their angular component (hue). In contrast, in the *CIELUV* tensorial representation, eigenvectors directions have a questionable meaning, since they are associated to the v component (not an angular information).

The same conclusion can not be extended to the other two lines of Fig. 2.13. That is because they were obtained using the FN and the LogE measures, functions that take into account not only the eigenvectors directions, but also the shape and trace of the ellipse representing colors. Therefore,

[4]errata: “structuring” substitui “structured” (versão publicada)

(a) Original

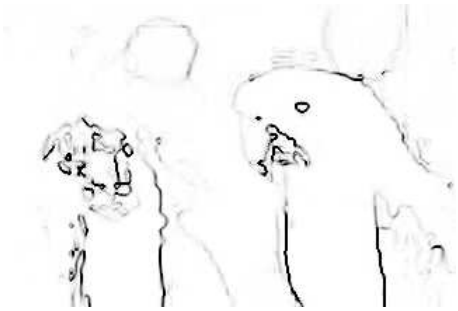

(b) Dot product

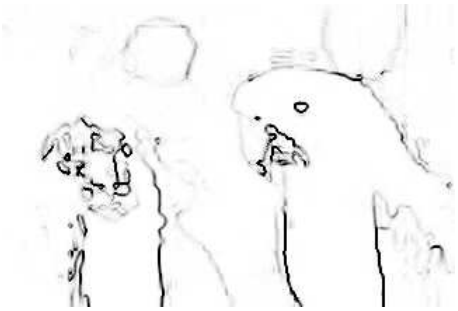

(c) Tensorial dot product

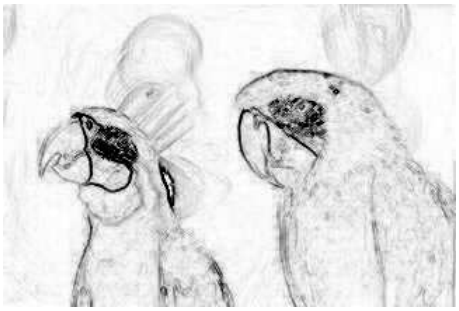

(d) Frobenius Norm

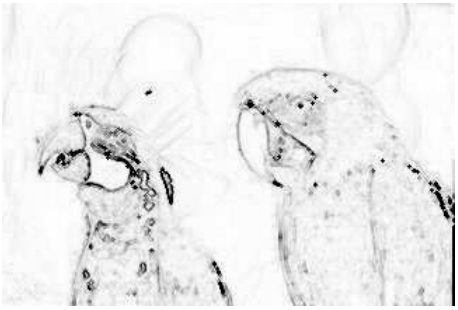

(e) J-divergence

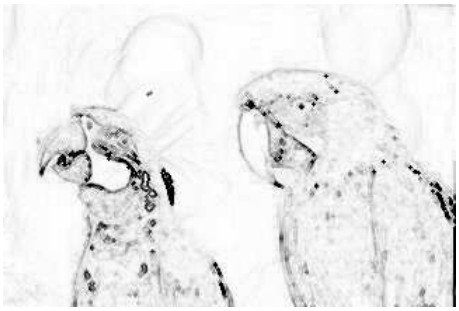

(f) Log-Euclidean distance

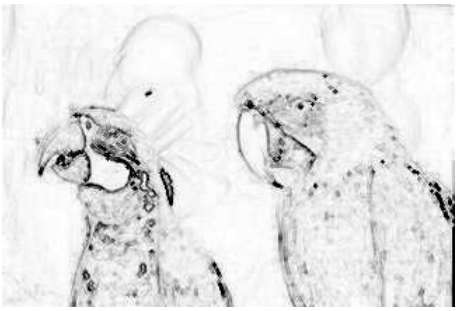

(g) Riemannian distance

Fig. 2.12: Tensorial morphological gradients (TMGs) using different similarity measures

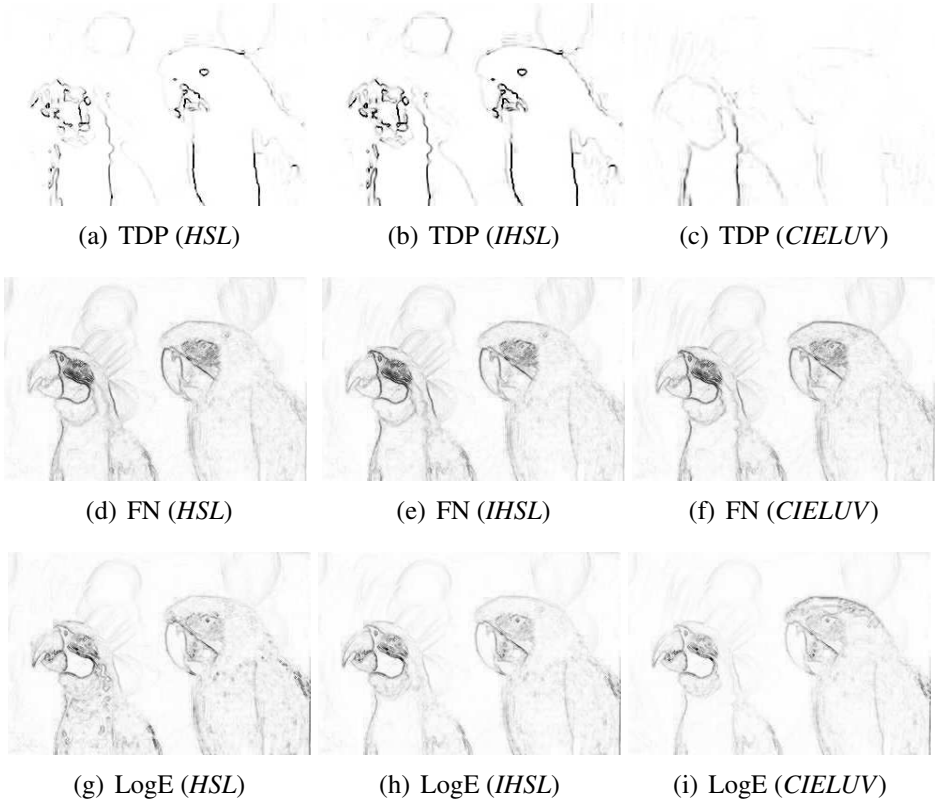

(a) TDP (*HSL*) (b) TDP (*IHSL*) (c) TDP (*CIELUV*)

(d) FN (*HSL*) (e) FN (*IHSL*) (f) FN (*CIELUV*)

(g) LogE (*HSL*) (h) LogE (*IHSL*) (i) LogE (*CIELUV*)

Fig. 2.13: Tensorial morphological gradients (TMGs) using different similarity measures and different color models

gradients based on the *CIELUV* tensorial representation are more likely to present satisfactory segmentation results, when computed using the FN and the LogE measures. In contrast, gradients based on *HSL* and *IHSL* tensorial representations computed using different similarity measures look very similar and is not possible to make any statement about their segmentation performance just looking at them.

2.6 Segmentation experiments

This section presents the hierarchical segmentation achieved by the combination of tensorial representation of colors, tensorial morphological gradient, watershed from markers [Beucher and Meyer, 1992, Vincent and Soille, 1991, Falcão et al., 2004, Cousty et al., 2009] and extinction values computation [Vachier and Meyer, 1995, Najman and Schmitt, 1996, Meyer, 1996]. The images used in this section were obtained from the Berkeley Segmentation Dataset (BSDS) [Martin et al., 2001], a database of 300 natural images, manually segmented by a number of different subjects. The watershed transform, the extinction functions and other morphological functions can

be found in the "SDC Morphology Toolbox for MATLAB" [Dougherty and Lotufo, 2003]. The hierarchical segmentation is done by classifying structures in the TMG image according to an extinction function and selecting them - by marker imposition - in order to compute the watershed from markers.

In the first experiment, images were segmented by the watershed transform over the TMG computed using all six similarity functions. After calculating the TMG of the original image, the n structures in the image which have the greatest volume extinction values were automatically selected. The n markers assigned to these regions were then used in the watershed transform, which segmented the TMG in n regions.

Different color models were used and all tensorial measures presented were applied to the TMG computation. Likewise Section 2.4, that showed that each one of the tensorial color representation based on distinct color models has significant differences and Subsection 2.5.2, that analyzed several aspects of the different tensorial similarity functions, pointing out their divergences, this section has the intention to show the differences in segmentation resulting from distinct similarity measures associated to different tensorial color representations. As in Subsection 2.5.3, all gradients were computed using a 3×3 diamond structuring element, except the gradient proposed by [Zenzo, 1986], that used a 3×3 square.

Fig. 2.14 depicts watershed segmentation results obtained applying all similarity measures in a *HSL* tensorial representation of the "parrots" image. The image was segmented in 25 regions and the results confirmed what was expected by analyzing Fig. 2.12 (Subsection 2.5.3). The TMG using the FN (Fig. 2.14(c)) resulted in a better segmentation, in comparison to the DP (Fig. 2.14(a)), TDP (Fig. 2.14(b)) and J-div (Fig. 2.14(d)) measures. The TMGs using the LogE (Fig. 2.14(e)) and the Riem (Fig. 2.14(f)) had a good performance too, although inferior to the one using the FN. Basically, the three measures were able to segment the parrot from the right, but only the segmentation obtained by the FN was able to delineate the head of the parrot from the left.

The number of regions - 25 - was chosen because, taking into account the complexity of the Parrots image, 25 regions was a reasonable number to illustrate the impact of the TMG choice in the segmentation of such image. A greater number of regions would not highlight the differences among the TMGs and a lesser number would not provide a meaningful segmentation to be discussed.

In Fig. 2.15 only a detail of the "parrots" image is segmented. Fig. 2.15(a) shows the original image and the selected region to be segmented is in Fig. 2.15(b). The selected image detail was segmented in three regions using the five distinct similarity measures applied to the *HSL* tensorial representation. Fig. 2.15(c) depicts the five TMGs obtained and the respective segmentation obtained by each one. The gradients were negated for a better presentation. Because the three main regions are represented by tensors with very distinct PEDs, all similarity measures were able to segment them,

(a) Dot product (b) Tensorial dot product

(c) Frobenius Norm (d) J-divergence

(e) Log-Euclidean distance (f) Riemannian distance

Fig. 2.14: Watershed segmentation of the “parrots” image with 25 regions using TMGs

even the DP and the TDP, that do not take into account the full tensor information. The obtained watershed lines were a little bit distinct, nonetheless all segmentations presented satisfactory results.

The first line of Fig. 2.15(d) shows different TMGs obtained by the same measure (FN) applied to tensorial representations using three different color models. The second line of the same figure contains the segmentation results obtained for each of the three computed TMGs. It shows that the obtained watershed lines differ from each other, nevertheless all are able to correctly segment the three regions.

Another detail of the "parrots" image can be seen in Fig. 2.16, this time to better illustrate the differences among the TMGs computed by distinct measures. It helps also to understand why some segmentation results are superior than others and in which circumstances this happens.

Fig. 2.16(a) shows the original image, where the detail is marked by a white rectangle. Fig. 2.16(b) depicts only the chosen detail with the tensorial representation for each pixel (ellipses). Although there are significant differences among ellipses, an easier way to identify and analyze the differences is to plot separately each property of the ellipses - PED, shape and trace - i.e., the color components - hue, saturation and luminance. They can be found in Fig. 2.16(c), Fig. 2.16(d) and Fig. 2.16(e), respectively. Based on Fig. 2.16(c), it can be observed that, although in the image the colors from the blue neck of the parrot look very different from the colors of the white background, their hue are almost the same. That means that any measure that only takes into account the hue of the color, i.e., the PED of the tensors, would not be able to segment it. Fig. 2.16(h) and Fig. 2.16(i) confirm that, showing that the TMG computed using the DP or the TDP preserve only the border between the yellow and the blue part of the neck, because is where Fig. 2.16(c) presents a strong border, dividing the two regions with distinct hues.

Fig. 2.16(f) and Fig. 2.16(g) present the results of the segmentation based on the TMG computed using the Frobenius Norm and the affine-invariant Riemannian metric, respectively. The lines obtained by the watershed over the FN-TMG contain the border between the neck and the background, as opposed to the Riemannian-TMG, that does not contain it. The explanation comes from analyzing Fig. 2.16(d), Fig. 2.16(e), Fig. 2.16(j) and Fig. 2.16(m).

Fig. 2.16(d) shows that the saturation of colors that belong to the blue region is not constant, on the contrary, presents small variations. The same can be observed inside the white region, where the saturation of colors assume a range of values significantly lower than the ones from the blue region. In Fig. 2.16(j) it is possible to identify that the TMG obtained using the FN contains a strong gradient (lighter line) where the border of the neck and the background should be. It confirms that the FN recognizes that the saturation oscillation inside the regions are not so strong as the saturation difference between the regions, thanks to the constant derivative of the FN previously discussed (Fig. 2.8). On the other hand, Fig. 2.16(m) shows that the gradient computed by the Riemannian

(a) Original image

(b) Selected region

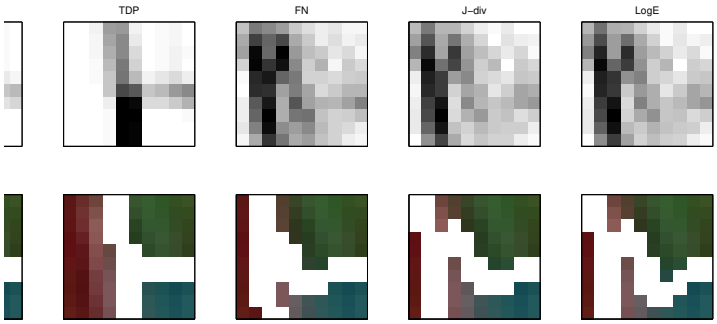

(c) HSL tensorial representation and different similarity measures

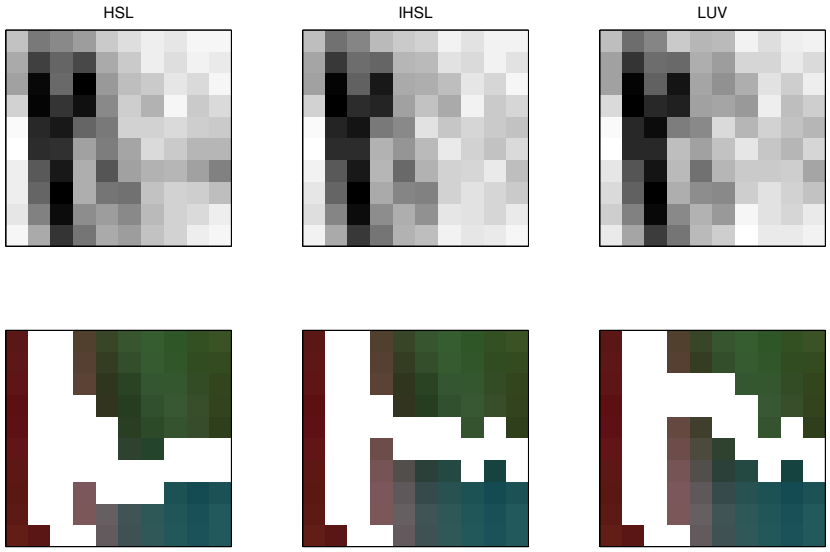

(d) Different color models for tensorial representation and FN measure

Fig. 2.15: Negated TMGs and segmentation results of a detail of the “parrots” image. The TMGs were computed using different similarity measures and different color models

(a) Selected region

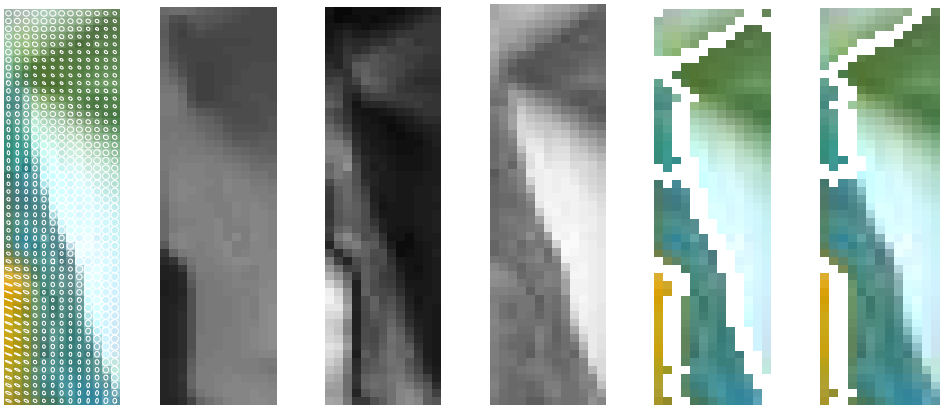

(b) Tensors (c) Hue (d) Sat (e) Lum (f) FN (g) Riem

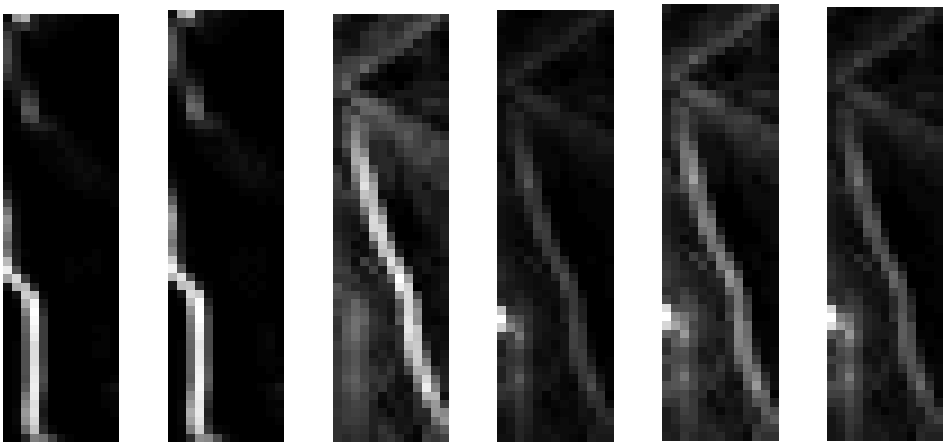

(h) DP (i) TDP (j) FN (k) Jdiv (l) LogE (m) Riem

Fig. 2.16: Detail of the parrot image - color components, watershed results and TMGs

metric inside the blue region (high saturation) is almost as strong as the gradient in the border between the blue and the white regions. That is due to the high derivative of the Riemannian metric with the saturation (Fig. 2.8). The same behavior is observed in Fig. 2.16(k) and Fig. 2.16(l), consequence of their high derivatives as well. Similar reasoning can be done for the luminance (Fig. 2.16(e)).

It is important to note that the Frobenius Norm would not be able to segment object and background if their color were perpendicular and have identical saturation and luminance. Despite of that, it presented the best segmentation results, mainly because real images are unlikely to have objects and background with completely uniform colors (null variation of hue, saturation and luminance). And probably if the color of some pixels of the object were perpendicular to the color of some pixels of the background, the TMG computed for the pixels in that region (using the FN) would not be null, since the TMG takes into account the dissimilarities not only between a pair of pixels but within a neighborhood (defined by the structuring element) and takes the maximum.

Fig. 2.17 presents segmentation results using some possible combinations of similarity measures and tensorial representation using different color models. The image was segmented in 25 regions for every combination and the watershed lines were overlaid on the original image. The obtained results confirm the expectations. Aside from certain combinations of tensorial representation and similarity measure that are not adequate (for example, Fig. 2.17(c)), all obtained segmentation can be considered satisfactory. Naturally, some specific combinations presented superior results than the rest (Fig. 2.17(d) and Fig. 2.17(e)), however, this superiority can vary according to the image to be segmented. In other words, for a coarse segmentation, almost any combination of a tensorial representation and a similarity measure can be used. Conversely, for a fine segmentation, the combination should be carefully chosen. Anyway, the best segmentations would most likely result from combinations of tensorial representations containing angular components (*HSL*, *HSV* e *IHSL*) and measures using full tensor information (FN, J-div, LogE and Riem).

To confirm our observations about the segmentation results using TMGs based on different similarity measures, quantitative evaluation tests were performed. The segmentation evaluations conducted were proposed by [Borsotti et al., 1998]. Segmentation results using different measures for the computation of the TMG were compared. Hierarchical segmentations using the color gradient proposed by Di Zenzo [Zenzo, 1986] were also performed, and these segmentation were evaluated as well. A qualitative analysis of the TMG was done, using as benchmarking segmentation algorithms contained at the Berkeley Segmentation Dataset (BSDS) [Martin et al., 2001]. Fig. 2.18 presents two examples of images of this Dataset.

The segmentation evaluations were done by applying two functions proposed by [Borsotti et al., 1998] to assess segmentation of color images. Both functions assess segmentation of color images according to heuristic criteria such as homogeneity and simplicity. When comparing

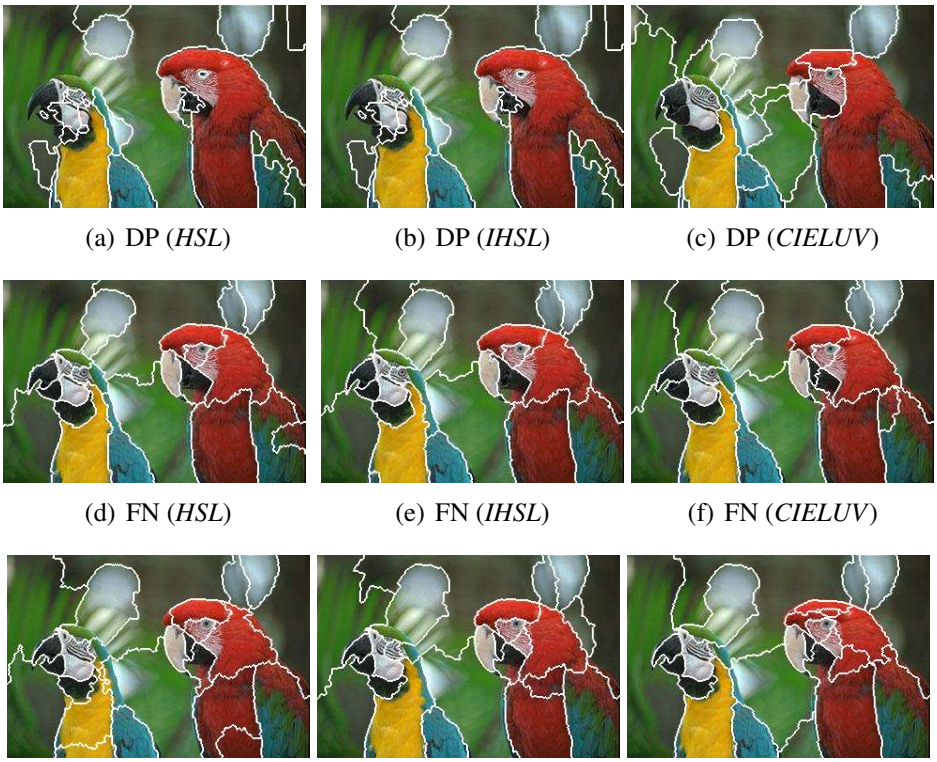

(a) DP (*HSL*) (b) DP (*IHSL*) (c) DP (*CIELUV*)

(d) FN (*HSL*) (e) FN (*IHSL*) (f) FN (*CIELUV*)

(g) LogE (*HSL*) (h) LogE (*IHSL*) (i) LogE (*CIELUV*)

Fig. 2.17: Watershed segmentation results based on TMGs computed using different similarity measures and different color models

(a) 42049 (b) 227092

Fig. 2.18: Two images from the Berkeley segmentation dataset (BSDS)

segmentation results, the lower results are provided by the best segmentation. Both functions are stated as follows:

$$F'(I) = \frac{1}{10000 \times N \times M} \times \sqrt{\sum_{A=1}^{Max} R(A)^{1+1/A}} \times \sum_{i=1}^{R} \frac{e_i^2}{\sqrt{A_i}} \tag{2.12}$$

and

$$Q(I) = \frac{1}{10000 \times N \times M} \times \sqrt{R} \times \sum_{i=1}^{R} \Big[\frac{e_i^2}{1 + \log A_i} + \Big(\frac{R(A_i)}{A_i} \Big)^2 \Big], \tag{2.13}$$

where N and M are, respectively, the height and width of the image, $R(A)$ is the number of regions having area equals to A, Max is the greatest segmentation area, R is the number of regions the image was segmented, A_i is the area of region i and e_i is the average color error for region i (see [Borsotti et al., 1998] for more details).

Fig. 2.19 shows an example of the segmentation assessment of the TMGs. The five proposed TMGs were applied to images under the *HSL*, *IHSL* and *CIELUV* color models. Hierarchical segmentations were done selecting the desired number of regions and then the values for F' and Q were computed. The comparison was done taking into account that the lesser the evaluation a segmentation receives, the better is the achieved segmentation. Under the conditions pointed above, the TMG using the Frobenius Norm achieved the best segmentations in all tested color spaces. While F' was between 30 and 39 for the Frobenius Norm, it was between 44 and 337 for all TMGs based on other measures. It also performed better than segmentations based on the Di Zenzo gradient ($F' = 223.6813$ and $Q = 3641.596$). Similar results were obtained for the Q value, that ranged from 371 to 585 for the TMG using the Frobenius Norm and from 658 and 6374 for all other TMGs. The superiority of the Frobenius Norm over other TMGs was confirmed in all segmentation experiments conducted for other images from the same dataset.

From Fig. 2.19 it is also possible to observe that there was almost no difference between the *HSL* and the *IHSL* color model representation , and that they performed better than the *CIELUV*. In all other segmentation experiments, TMGs in the *HSL* and the *IHSL* color models presented better F' and Q values than the correspondent TMG in the *CIELUV* model.

Fig. 2.20 shows the quantitative assessment of 22 images from the Berkeley dataset. The TMG gradients were computed from the tensorial representation of the dataset images under the HSL color space model. Fig. 2.20 shows the segmentation error from application of four metrics: Frobenius Norm, J-divergence, Log-Euclidean and Riemannian. The dot product and the tensor dot product results are not shown in the Fig. 2.20 because the segmentation errors computed by those metrics were very high compared to the other ones.

Fig. 2.20(a) shows the segmentation error computed by the Borsotti F' metric for each one of the

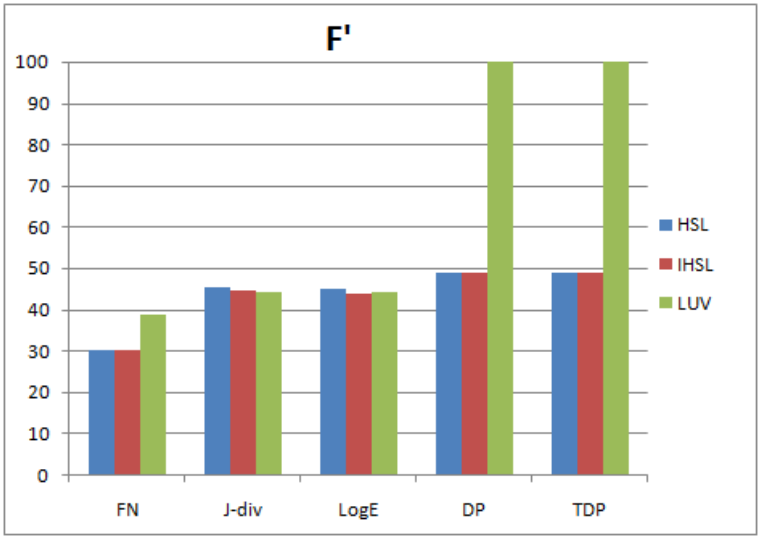

Fig. 2.19: Evaluation of segmentation results for image 42049

22 images taken from the dataset. Each value in the x-axis represents an image and the values in the y-axis give the error computed from the segmentation provided by application of the four considered metrics. This graphic shows which metrics provided the lowest error for each image. Fig. 2.20(c) shows the amount of the images where a given metric provided the lowest segmentation errors. See that Frobenius Norm won 72.73% of the test cases: it provided the lowest errors in 16 test cases. J-divergence won in three cases. Log-Euclidean won in two cases and the Riemannian metric won in just one test case.

The plottings in Fig. 2.20(b) and Fig. 2.20(d) were drawn from the experiments done by application of the Borsotti Q metric. The meaning of these plottings is the same of Fig. 2.20(a) and Fig. 2.20(c), respectively. Again, Frobenius Norm provided the best segmentation results in 72.73% of the test cases (the other three metrics achieved the best results in two test cases each one). Frobenius Norm supported the best segmentations according the two error measurements proposed by Borsotti.

Fig. 2.21 and Fig. 2.22 show segmentation obtained from the watershed transform over the TMG in comparison to segmentations available at the Berkeley segmentation dataset.

Fig. 2.21 presents the segmentation result given by the application of TMG with Frobenius Norm to Fig. 2.18(a). The goal is to compare the obtained result to other segmentations. Berkeley database provides several segmentation results: Fig. 2.21(a) shows the segmentation provided by an human operator. This segmentation provides a kind of ground-truth to which all segmentations of Fig. 2.18(a) submitted to the dataset website are compared. Fig. 2.21(b) shows the segmentation given by the Boosted Edge Learning technique, considered the best segmentation submitted and compared to the ground-truth. Fig. 2.21(c) shows the FN-based TMG and Fig. 2.21(d) shows its segmentation

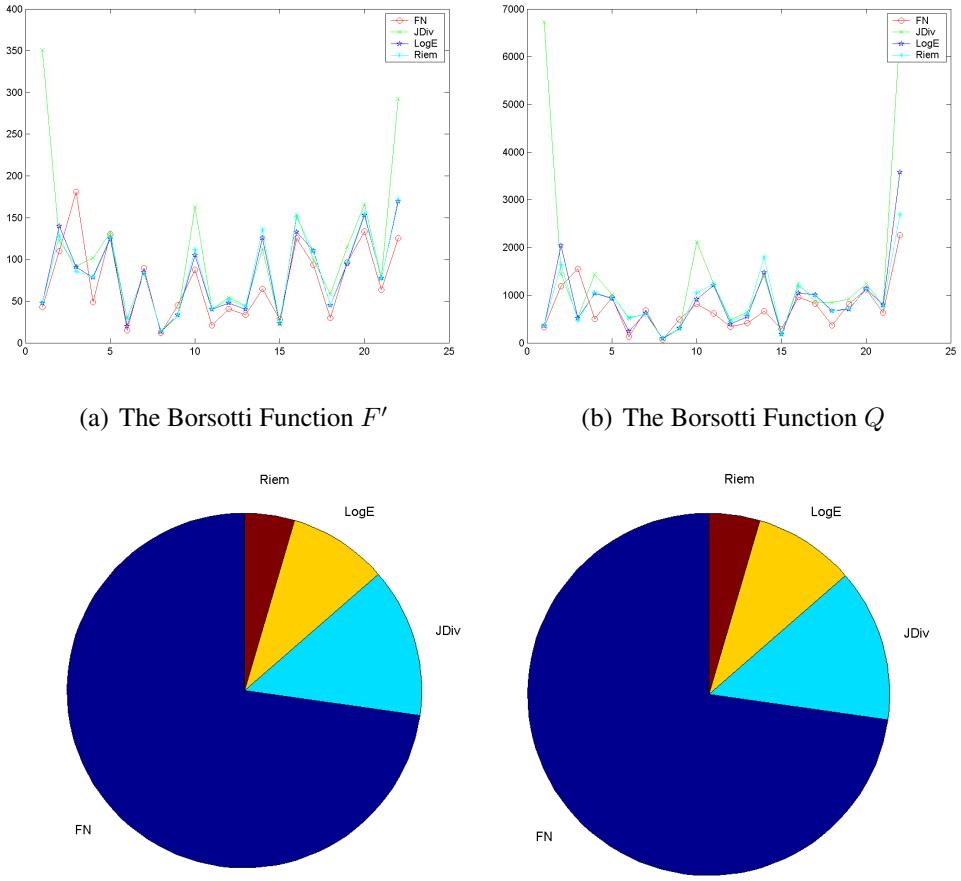

(a) The Borsotti Function F'

(b) The Borsotti Function Q

(c) Lowest Borsotti F' errors

(d) Lowest Borsotti Q errors

Fig. 2.20: Evaluation of segmentation results for 22 images. (a) and (b) Segmentation error for each test case; (c) and (d) Amount of lowest errors for each TMG metric

in 15 regions, according to the volume extinction function criterium. Figure Fig. 2.21(e) and Fig. 2.21(f) show, respectively, the Di Zenzo gradient and its segmentation in 15 regions, according to the volume extinction function criterium. Note that the Boosted segmentation does not present well defined segmentation lines. The watershed applied to FN-based TMG and Di Zenzo gradients provided a more precise segmentation. Note that these lines appear more with the lighters lines in the human segmentation that the ones in the Boosted segmentation. Segmentations in Fig. 2.21(d) and Fig. 2.21(f) are quite similar, and each one segments different regions in a more detailed way. FN-based TMG supported a detailed segmentation of the wing and the tree. Dizenzo gradient supported a better segmentation of the branches.

Fig. 2.22 presents another comparison with an image from Berkeley dataset. Fig. 2.22(a) shows the original image, a vase with several drawings. Fig. 2.22(b) and Fig. 2.22(c) show, respectively, the human segmentation and the one provided by the Global Probability of Boundary

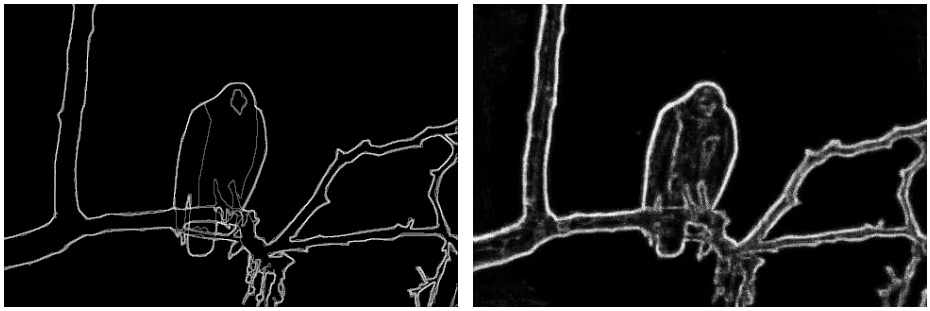

(a) Human (b) Boosted Edge Learning

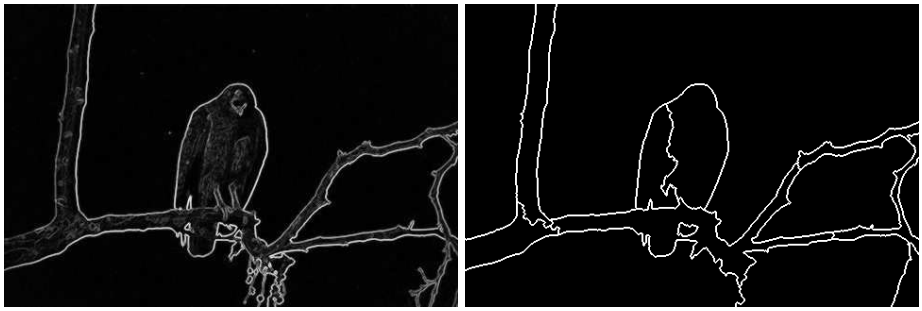

(c) TMG (FN) (d) WS - 15 regions (FN)

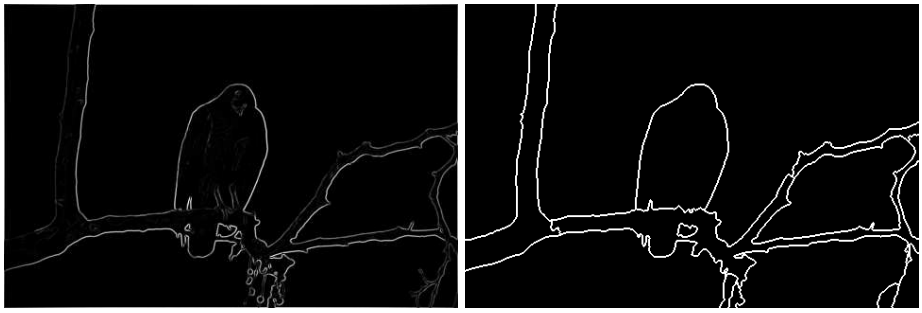

(e) DiZenzo gradient (f) WS - 15 regions (DiZenzo)

Fig. 2.21: Tensorial morphological gradients (TMGs) compared to other segmentation algorithms

technique. Fig. 2.22(d), Fig. 2.22(e) and Fig. 2.22(f) show, respectively, the FN-based TMG of the vase, and its segmentation in 30 and 120 regions, according to the volume extinction function criterium. Fig. 2.22(g), Fig. 2.22(h) and Fig. 2.22(i) show, respectively, the Di Zenzo gradient and its segmentation in 30 and 120 regions, according to the volume extinction function criterium. The goal is to visually evaluate the segmentation results and to comment the impact in the selection of the number of regions in the hierarchical segmentation. Note that Global Probability of Boundary segmentation does not enhance the main features pointed by the user in the human segmentation. Segmentations in Fig. 2.22(f) and Fig. 2.22(i) provide a better representation of the lines in the human segmentation - see the amount of details identified in these images. The segmentations with 30 and 120 images were done in order to illustrate how much information is segmented when the number of regions grows. Note that the vase is already segmented with just 30 regions with a small amount of vase details. With 120 regions, the amount of details was increased. However, Di Zenzo segmentation in both examples did not segmented the vase entirely and a small region at the bottom of the vase was segmented with a detail from the wall. FN-based TMG segmentation, however, segmented the vase entirely, with a good degree of details, but at the cost of segmenting the background in several regions as well.

2.7 Conclusions

This paper proposes a tensorial framework for color images. As part of this framework, a tensorial representation of color images and a tensorial morphological gradient (TMG) are presented.

The new tensorial representation of color images was obtained by establishing a relation between the attributes of an ellipse and the components of a color image. Representations for different color models were studied and compared, showing that color models containing an angular component are more likely to fit in the tensorial representation than the ones with no angular component.

Based on this new tensorial representation and using tensor similarity measures, a Tensorial Morphological Gradient (TMG) was proposed. Different tensorial similarity measures were implemented (the dot product, the tensor dot product, the Frobenius Norm, the J-divergence, the Log-Euclidean distance and the affine-invariant Riemannian metric) to compute the TMG. The behavior of the presented similarity measures regarding to color comparison were investigated. Noise sensitivity and affine-invariant properties were analyzed, in order to explore strengths and weaknesses of each measure.

The analysis showed that the measures based only on hue are not appropriate since they may consider that colors with different levels of saturation and/or intensity are equal. More, J-div, LogE and Riem measures do not provide a linear dissimilarity rate along the saturation and luminance values, whereas the Frobenius Norm does. And although Frobenius Norm is not affine-invariant

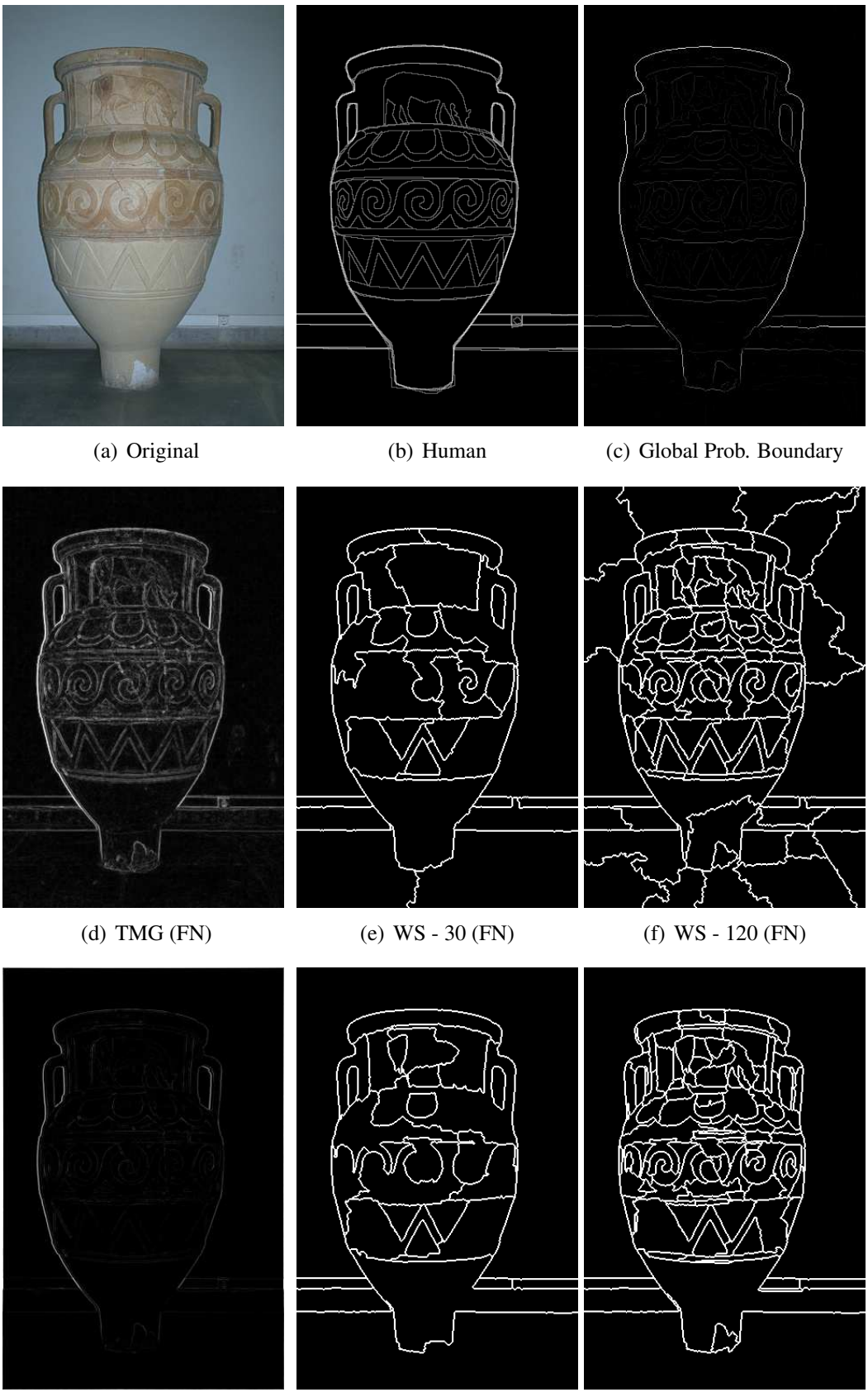

(a) Original (b) Human (c) Global Prob. Boundary

(d) TMG (FN) (e) WS - 30 (FN) (f) WS - 120 (FN)

(g) DiZenzo gradient (h) WS - 30 (DiZenzo) (i) WS - 120 (DiZenzo)

Fig. 2.22: TMGs compared to other segmentation algorithms

to rotation and is a relatively simple measure, it proved to be the most robust one and showed good performance. On the other hand, affine-invariant measures did not performed well, because of their high derivatives, that turned out to be more important in color images segmentation than the affine-invariant property.

Different combinations of color representation and similarity measures were used to compute the TMG, in order to evaluate their influence in the segmentation performance. Combinations that involved DP and TDP provided the worst results: in the *RGB* and *CIELUV* cases it were attempted to use angular information from not angular color models; in the other cases, such measures did not exploit enough information from the image. Combinations that involved *RGB* and *CIELUV* models with other measures did not provide good segmentation results since the tensorial representation do not appear suitable to represent such color models. Combinations of tensorial representations containing angular components (*HSL*, *HSV* and *IHSL*) and measures using full tensor information (FN, J-div, LogE and Riemannian) were more appropriate to computation of color images gradient.

Several research opportunities are open. Future works include: the study of alternative tensor models and dissimilarity metrics - Peeters [Peeters et al., 2008] cites several metrics that may be applied to design new TMG's; precision and recall scores proposed by the Berkeley Segmentation Dataset (BSDS) and Benchmark [Martin et al., 2001] may be computed to evaluate the segmentation results achieved by the proposed segmentation framework; the design of new applications for tensorial color images, such as the use of tensors as attributes in pattern recognition methods or the use of tensorial operations to do color image filtering.

Acknowledgments

This work was supported in part by CNPq. Franklin C. Flores is on leave from State University of Maringá - Brazil, at School of Electrical and Computer Engineering - UNICAMP - Brazil, for doctorate purposes.

Capítulo 3

Segmentação de imagens sintéticas de tensores de difusão

Este capítulo contém o artigo "Diffusion tensor imaging segmentation by watershed transform on tensorial morphological gradient" [Rittner and Lotufo, 2008], publicado nos anais do *XXI Simpósio Brasileiro de Computação Gráfica e Processamento de Imagens - SIBGRAPI'08*. Ele propõe o uso do gradiente morfológico tensorial e da transformada de *watershed* para realizar a segmentação de imagens de tensores de difusão.

Com o objetivo de discutir as diferentes medidas de similaridade propostas para o cálculo do TMG, a influência do elemento estruturante neste cálculo, bem como a robustez do TMG na presença de ruído, imagens sintéticas de tensores de difusão foram geradas e utilizadas nos experimentos. Imagens de difusão adquiridas de um *phantom* criado com espinha dorsal de ratos também foram incluídas nos experimentos.

3.1 Abstract

While scalar image segmentation has been studied extensively, diffusion tensor imaging (DTI) segmentation is a relatively new and challenging task. Either existent segmentation methods have to be adapted to deal with tensorial information or completely new segmentation methods have to be developed to accomplish this task. Alternatively, what this work proposes is the computation of a tensorial morphological gradient of DTI, and its segmentation by IFT-based watershed transform. The strength of the proposed segmentation method is its simplicity and robustness, consequences of the tensorial morphological gradient computation. It enables the use, not only of well known algorithms and tools from the mathematical morphology, but also of any other segmentation method to segment DTI, since the computation of the tensorial morphological gradient transforms tensorial images in

scalar ones. In order to validate the proposed method, synthetic diffusion tensor fields were generated, and Gaussian noise was added to them. A set of real DTI was also used in the method validation. All segmentation results confirmed that the proposed method is capable to segment different diffusion tensor images, including noisy and real ones.

3.2 Introduction

Diffusion tensor imaging (DTI) is a relatively new modality of Magnetic Resonance Imaging (MRI) able to quantify the anisotropic diffusion of water molecules in highly structured biological tissues. It is unique in its ability to quantify changes in neural tissue microstructure within the human brain non-invasively. Diffusion tensor imaging (DTI) segmentation, where regions of interest are delineated, is necessary for performing subsequent quantitative analysis and qualitative visualization. While scalar image segmentation has been studied extensively and different algorithms have been developed over a long period of time, DTI segmentation is a relatively new and challenging task and only a few different approaches for DTI segmentation have been proposed in the last decade [Zhukov et al., 2003, Ziyan et al., 2006, Weldeselassie and Hamarneh, 2007, Wang and Vemuri, 2005, Awate and Gee, 2007, Wiegell et al., 2003].

This work describes an approach to DTI segmentation using concepts from mathematical morphology [Dougherty and Lotufo, 2003] and from the Image Foresting Transform (IFT) [Falcão et al., 2004]. And the image edge enhancement by gradient computation is an important step in morphological image segmentation via IFT-based watershed transform [Lotufo and Falcão, 2000, Lotufo et al., 2002]. For scalar images, the morphological gradient [Heijmans, 1994] is a very good option and its computation is simple: for each point in the image, a structuring element is centered to it and the difference between the maximum and the minimum graylevels inside the structuring element is computed. Here, the dissimilarity information exploited is the intensity difference among pixels inside the structuring element.

Such concept does not extend naturally to tensorial images. Although the dissimilarity information is richer in tensorial images than in scalar ones, the design of methods to edge enhancement in tensorial images is complex. Note that measures that compute the dissimilarity information of tensorial images are not natural for the human eye. Not to mention that information contained in the diffusion tensors is complex, and is still unknown which information is important for segmentation purposes and which can (and should) be ignored. Furthermore, either existing segmentation methods have to be adapted to deal with tensorial information or completely new segmentation methods have to be developed to accomplish this task.

Alternatively, what this work proposes is the computation of a gradient, that transforms the

diffusion tensor image into a scalar image, and makes possible the use of any existing segmentation method in order to perform the DTI segmentation. With this in mind, the tensorial morphological gradient is employed. The tensorial morphological gradient was first applied to tensorial images representing color images [Rittner et al., 2007], but its concept can be extended and applied to any kind of tensorial image.

This paper is organized as follows: Section 3.3 describes the tensorial morphological gradient (TMG) after presenting a summary of basic concepts related to it. Section 3.4 presents the TMG applied to diffusion tensor images, through examples of synthetic and real tensorial images. Section 3.5 contains the segmentation results, obtained by the application of well-known segmentation techniques, such as IFT-based watershed transform and threshold, on the tensorial morphological gradient of diffusion tensor images. Finally, conclusions are summarized in Section 3.6.

3.3 Tensorial Morphological Gradient (TMG)

Although measures that computes the dissimilarity information of tensorial images are not natural for the human eye, by using them to compute a tensorial morphological gradient, it is possible to obtain an scalar image that can be interpreted as a border enhancement of the original tensorial image. Before explaining the tensorial morphological gradient (TMG), basic concepts regarding diffusion tensors, tensorial similarity measures and morphological gradient are briefly described.

3.3.1 Diffusion Tensors

A tensor is the mathematical idealization of a geometric or physical quantity whose analytic description, relative to a fixed frame of reference, consists of an array of numbers. In other words, it is an abstract object expressing some definite type of multi-linear concept. Its well-known properties can be derived from its definitions and the rules for manipulation of tensors arise as an extension of linear algebra to multilinear algebra [Danielson, 2003].

Diffusion Tensor Imaging (DTI) is based on second order tensors. In practice, a 3-dimensional second order tensor is denoted by a 3×3 matrix of values:

$$\mathbf{T} = \begin{pmatrix} T_{xx} & T_{xy} & T_{xz} \\ T_{yx} & T_{yy} & T_{yz} \\ T_{zx} & T_{zy} & T_{zz} \end{pmatrix}, \tag{3.1}$$

and can be reduced to principal axes (eigenvalue and eigenvector decomposition) by solving the

characteristic equation:

$$\mathbf{T} - (\lambda \cdot \mathbf{I})e = 0, \tag{3.2}$$

where $\mathbf{I}$ is the identity matrix, λ are the eigenvalues of the tensor and e are the normalized eigenvectors. Because de diffusion tensor is a symmetric positive definite matrix,i.e., $T_{xy} = T_{yx}$, $T_{yz} = T_{zy}$ and $T_{xz} = T_{zx}$ the eigenvalues are always real. Moreover, the corresponding eigenvectors are orthogonal [Bishop and Goldberg, 1980]. In this case, the tensor can be represented by an ellipsoid, where the main hemiaxis lengths are proportional to the square roots of the tensor eigenvalues λ_1, λ_2 and λ_3 ($\lambda_1 \geq \lambda_2 \geq \lambda_3$) and their direction correspond to the respective eigenvectors (Fig. 3.1).

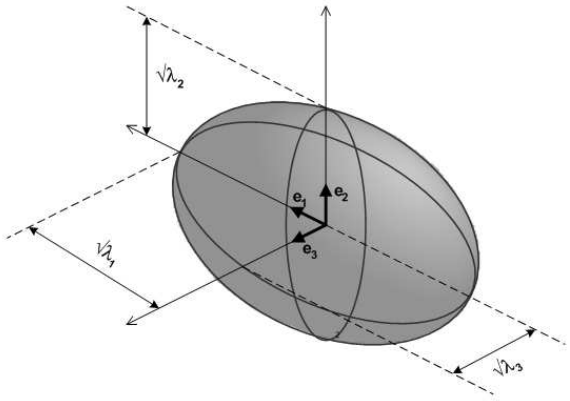

Fig. 3.1: Ellipsoid representing a tensor

The degree of anisotropy in the diffusion ellipsoid, as represented by the tensor, can be quantified in a single number called a diffusion anisotropy index. The most widely used diffusion anisotropy index is probably the fractional anisotropy (*FA*), described by Basser and Pierpaoli in [Basser and Pierpaoli, 1996]. It ranges from 0 (isotropic diffusion) to 1 (completely anisotropic diffusion) and is defined by:

$$FA = \sqrt{\frac{3[(\lambda_1 - \mathbf{T}_{av})^2 + (\lambda_2 - \mathbf{T}_{av})^2 + (\lambda_3 - \mathbf{T}_{av})^2]}{2(\lambda_1^2 + \lambda_2^2 + \lambda_3^2)}}, \tag{3.3}$$

where

$$\mathbf{T}_{av} = \frac{\lambda_1 + \lambda_2 + \lambda_3}{3}. \tag{3.4}$$

The fractional anisotropy of a diffusion tensor, as proposed in [Basser and Pierpaoli, 1996], characterize geometrically the shape of the ellipsoid, but not its size or orientation.

The sum of the diagonal elements, also called trace, is another property of the diffusion tensor,

and can be useful in comparing different tensors and ellipsoids. For a given 3×3 tensor, the trace of the ellipsoid can be calculated as follows:

$$\text{Trace} = (\lambda_1 + \lambda_2 + \lambda_3). \tag{3.5}$$

The trace of a diffusion tensor can be geometrically interpreted as the size of the ellipsoid, independent of shape and orientation.

3.3.2 Tensorial similarity measures

Since a key factor in DTI analysis is the proper choice of the similarity measure to be used, several works have been published on the subject. Given two tensors $\mathbf{T}_i$ e $\mathbf{T}_j$, the most simple comparison between two tensor quantities is the dot product between the principal eigenvector directions:

$$d_1(\mathbf{T}_i, \mathbf{T}_j) = |e_{1,i} \cdot e_{1,j}|, \tag{3.6}$$

where $e_{1,i}$ and $e_{1,j}$ are the principal eigenvectors of tensors $\mathbf{T}_i$ e $\mathbf{T}_j$, respectively. The absolute value of the dot product solves the problem with the sign ambiguity of the eigenvectors. This measure was used by Ziyan *et al.* to segment the thalamic nuclei from diffusion tensor images [Ziyan et al., 2006].

Another simple similarity measure, presented by Pierpaoli *et al.* as an intervoxel anisotropy index [Pierpaoli and Basser, 1996] and used by Alexander *et al.* [Alexander et al., 1999], is the tensor dot product:

$$d_2(\mathbf{T}_i, \mathbf{T}_j) = \lambda_{1,i}\lambda_{1,j}(e_{1,i} \cdot e_{1,j})^2 + \lambda_{2,i}\lambda_{2,j}(e_{2,i} \cdot e_{2,j})^2. \tag{3.7}$$

In [Alexander et al., 1999] Alexander *et al.* proposed another similarity measures. Their purpose was to match pairs of diffusion tensor images (DTI) and the proposed measures were based on the diffusion tensor itself and indices derived from the diffusion tensor. One of the similarity measures proposed by them was obtained negating the following Euclidean distance metric:

$$d_3(\mathbf{T}_i, \mathbf{T}_j) = \sqrt{\text{Trace}((\mathbf{T}_i - \mathbf{T}_j)^2)}. \tag{3.8}$$

This similarity metric was also explored in other DTI studies under different names, such as generalized tensor dot product [Jones et al., 1999] and Frobenius norm [Wiegell et al., 2003, Ziyan et al., 2006]. But because affine invariance is a desirable property for segmentation purposes and the Frobenius norm is not invariant to affine transformations, Wang and Vemuri [Wang and Vemuri, 2005] proposed a novel definition of diffusion tensor "distance", as the square root of the J-divergence of the corresponding Gaussian distributions, i.e.,

$$d_4(\mathbf{T}_i, \mathbf{T}_j) = \frac{1}{2}\sqrt{\text{Trace}(\mathbf{T}_i^{-1}\mathbf{T}_j - \mathbf{T}_j^{-1}\mathbf{T}_i) - 2n}. \tag{3.9}$$

Eq. 3.9 is not a true distance since it violates the triangle inequality, but it is in fact a computationally efficient approximation of Rao's distance [Wang and Vemuri, 2005].

The above similarity measures are not the only ones proposed in the literature, but they were chosen to be part of this study because of their simplicity and/or their good performance, when dealing with diffusion tensor imaging applications. It is important to notice that each one of them come from different approaches and privileges some aspects of tensors. For example, whereas the dot product takes in account only the principal eigenvector direction, the tensor dot product and the Frobenius norm use the full tensor information.

3.3.3 Morphological gradient

Several distinct gradients are used in image processing to detect edges. One of them is called the morphological gradient, that depends on the size and shape of the chosen structuring element. Using a flat structuring element at each point, the morphological gradient yields the difference between the maximum and the minimum values over the neighborhood at the point determined by the flat structuring element [Heijmans, 1994]. The use of a three-dimensional structuring element leads to a morphological gradient that takes into account the neighborhood in all directions, and not only in an specific plane.

3.3.4 Tensorial morphological gradient (TMG)

The tensorial morphological gradient (TMG) was first described in [Rittner et al., 2007] and used, together with a tensorial representation of colors, to segment color images. Let $E = \mathbb{Z} \times \mathbb{Z}$ be the set of all points in the tensorial image f. The tensorial morphological gradient (TMG) is defined by

$$\nabla_B^T(f)(x) = \bigvee_{y,z \in B_x} d_n(\mathbf{T}_y, \mathbf{T}_z), \tag{3.10}$$

$\forall x \in E$, where d_n represent any of the similarity measures presented in Subsection 3.3.2, $B \subset E$ is a structured element centered at the origin of E, $\mathbf{T}_y$ is the tensor that represents the diffusion in y, and $\mathbf{T}_z$ is the tensor that represents the diffusion in z (y and z are in the neighborhood of x, defined by B_x[1]). ∇_B^T is the proposed TMG.

Because the chosen measures are already comparisons between neighbors, the proposed gradient is not the difference between the maximum and the minimum values, as in the classical morphological

[1] errata: "B_x" substitui "E" (versão publicada)

gradient, but only the maximum value. In other words, the computed gradient in a neighborhood given by an structuring element is the maximum dissimilarity among all pairwise dissimilarities.

So the main requirement of the TMG is that it must retain as much information from the tensors as possible. In other words, in order to compute the TMG the chosen similarity measure must take into account the most important characteristics of diffusion tensors, when compared to one another.

3.4 Tensorial morphological gradient of diffusion tensor images

As stated before, the tensorial morphological gradient (TMG) was first applied to tensorial images representing color images [Rittner et al., 2007], but its concept can be extended and applied to any kind of tensorial image.

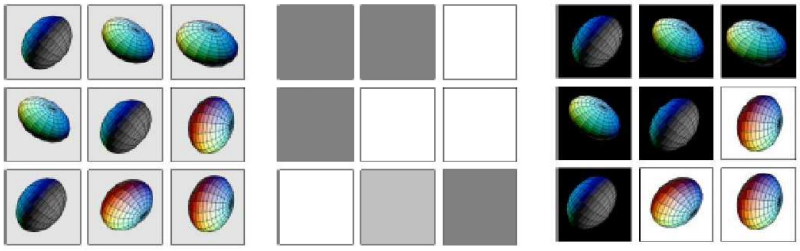

(a) Tensorial image (b) TMG (c) Segmented image

Fig. 3.2: Representation of a tensorial image segmentation based on TMG

Fig. 3.2 depicts the idea behind the proposed tensorial morphological gradient (TMG) [2]. Fig. 3.2(a) shows an example of a 3×3 tensorial image, where instead of scalar values, each pixel of the image contains a tensor, i.e., a symmetric positive definite 3×3 matrix of values. Therefore, each pixel of the image is represented by an ellipsoid and not by a gray level. The segmentation of such an image is not a trivial task, not even for a human. Which ellipsoids should be together in a cluster and which ones do not belong to the first cluster and should form a second cluster? So, instead of trying to answer this question by looking to the tensorial image, the TMG is computed. This step translates the tensorial information into scalars, resulting in a gray-level image (Fig. 3.2(b)). Finally, all the image analysis, in this example the segmentation (Fig. 3.2(c)), can be done over an scalar image.

To illustrate the computation of the tensorial morphological gradient of diffusion tensor images, some synthetic tensor fields were created. Real diffusion data was also used. First, results of TMG computation using different tensorial similarity metrics are presented in Section 3.4.1. Second, distinct structuring elements were tested to compute TMG and the results can be found

[2] Fig.1 partially extracted from [Weldeselassie and Hamarneh, 2007]

in Section 3.4.2. And finally, noise was added to synthetic data. Resulting tensor field and its TMG are shown in Section 3.4.3 .

3.4.1 Distinct similarity measures

To run our first experiment, a synthetic diffusion data-set were created. The synthetic diffusion tensor field (Fig. 3.3(a)) is a 20 X 20 X 20 image where the tensors follow the tangent of the center-line of a torus and share the same eigenvalues. TMG was computed using all similarity measures presented in Section 3.3.2. Fig. 3.3(b) and Fig. 3.3(c) show the TMG computed for the synthetic torus using only two similarity measures: Dot product and Frobenius norm. Both TMG were computed using a 6-connected structuring element (3D).

Looking at Fig. 3.3 it is possible to conclude that, for this specific tensor field (torus), all similarity measures tested are adequate to compute the TMG. The dot product (Fig. 3.3(b)), unappropriate to compute TMG in a tensor field where changes in eigenvalues are more relevant than in eigenvectors, works fine in this example. Since the torus present tensors with constant eigenvalues and the only changes are in eigenvectors directions, it is an special circumstance where the TMG using the dot product preserves all necessary information to perform subsequent image processing. Similar behavior is expected from the TMG computed by the tensorial dot product, confirmed by Fig. 3.3(c).

Although the Frobenius norm was found as being the most suitable measure to compute the TMG for color images [Rittner et al., 2007], it presents some distortions, as can be seen in Fig. 3.3(d). The four light gray regions inside the torus derive from the fact that the Frobenius norm is not affine invariant, that is, dissimilarity computed between tensors that are aligned to cartesian axes are different from dissimilarity computed between tensors not aligned to cartesian axes. Conversely, Fig. 3.3(e) shows that, since the J-divergence is an affine invariant metric, the gray region inside the torus is homogeneously distributed, meaning that the TMG computed presents no distortions due to rotation of the tensors.

Another example of TMG calculation can be found in Fig. 3.4. Again, the TMG was computed using the same four tensorial similarity measures, but this time the entry was a real diffusion tensor data acquired from a rat spinal cords phantom (Fig. 3.4(a)) [Campbell et al., 2005]. In this case, computed TMGs using different measures look very distinct. Fig. 3.4(b) and Fig. 3.4(c) show that the dot product and the tensorial dot product are not appropriated to compute TMG in a precise manner when dealing with real data, since they take into account only the direction of the principal eigenvector of tensors. Conversely, Fig. 3.4(d) and Fig. 3.4(e) confirm that the Frobenius norm and the J-divergence are both more adequate measures to compute the TMG, since they consider the full tensor information. But, unlike previous experiment, it is not clear which measure leads to a better TMG: the Frobenius Norm or the J-divergence. Distortions due to the affine variant characteristic of

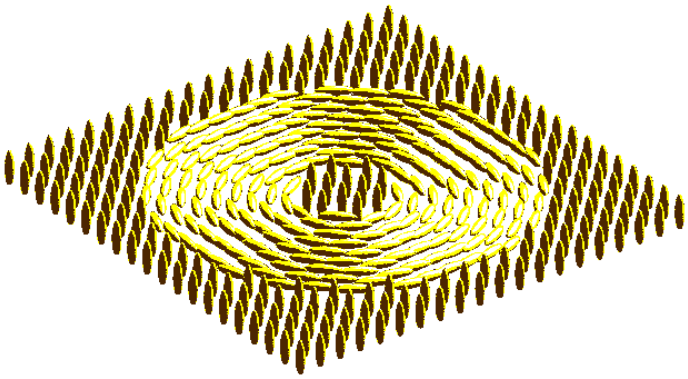

(a) Central slice of synthetic tensor field

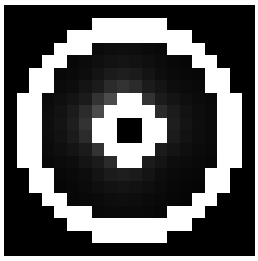

(b) Dot Product TMG

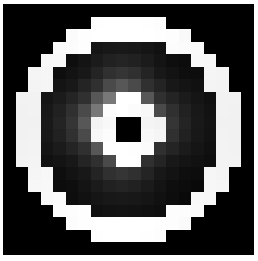

(c) Tensorial Dot Product TMG

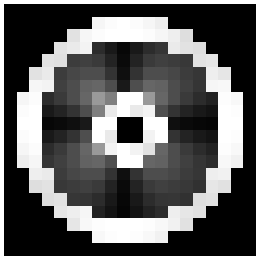

(d) Frobenius Norm TMG

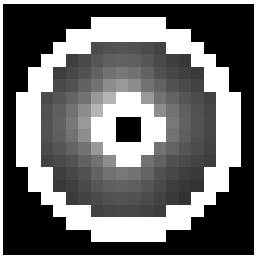

(e) J-divergence TMG

Fig. 3.3: One slice of the a synthetic tensor field (trace and anisotropy constant) and the computed TMGs using four different similarity measures: Dot product, Tensorial dot product, Frobenius norm and J-divergence

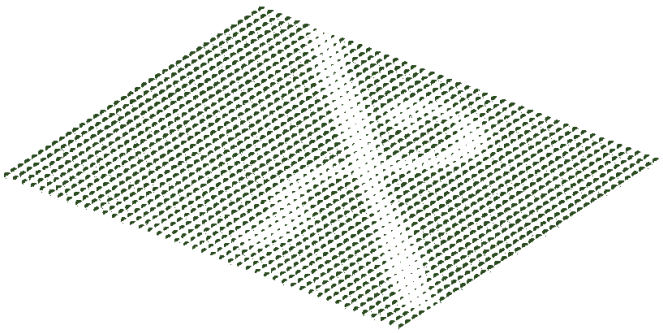

(a) One slice of real DTI (rat spinal cords phantom)

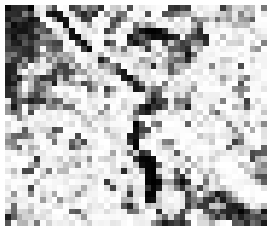

(b) Dot Product TMG

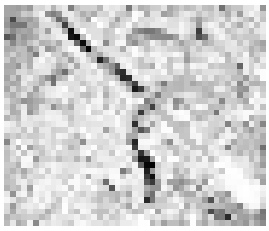

(c) Tensorial Dot Product TMG

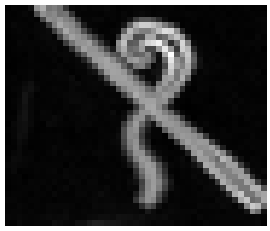

(d) Frobenius Norm TMG

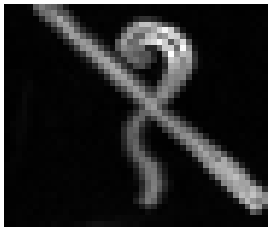

(e) J-divergence TMG

Fig. 3.4: One slice of a real diffusion tensor field (rat spinal cords phantom) and the computed TMGs using four different similarity measures: Dot product, Tensorial dot product, Frobenius norm and J-divergence

the Frobenius norm can not be detected. At least, not by a qualitative evaluation of the TMG.

3.4.2 Distinct structuring elements

All tensorial morphological gradient results presented in previous sections were computed using a 3D 6-connected structuring element. But it is also possible to choose a different neighborhood to compute the tensorial morphological gradient, by changing the structuring element used in the calculation. Any structuring element is admissible, but just a few ones make sense in this application. To illustrate the influence of the structuring element in the TMG computation, three different structuring elements where used: a 4-connected structuring element (2D), a 6-connected structuring element (3D) and a 26-connected structuring element (3D). All TMGs were computed using the Frobenius norm to measure the dissimilarities between tensors.

Fig. 3.5 depicts the representation of the three structuring elements that were used in this experiment (Fig. 3.5(a), Fig. 3.5(c) and Fig. 3.5(e)). Remember that the gradient is computed for the central voxel, taking into account information contained in the neighborhood defined by the structuring element. Fig. 3.5(b), Fig. 3.5(d) and Fig. 3.5(f) presents the resulting TMGs computed with the different structuring elements, where the influence of the chosen structuring element in the computed gradient can be easily identified. Using the 4-connected structuring element (Fig. 3.5(a)), the obtained TMG (Fig. 3.5(b)) takes only into account each slice of data separately, since the structuring element is bi-dimensional. The result is a thin TMG, good in preserving details of small structures. As the structuring element becomes bigger, or in a higher dimension (Fig. 3.5(c) and Fig. 3.5(e)), the borders of the computed tensorial morphological gradient becomes thicker (Fig. 3.5(d) and Fig. 3.5(f)). These TMGs are not suitable for detailed structures, but perform better if the object to be delineate presents a considerable volume (considerable number of voxels, in comparison to the structuring element) and three-dimensional information is important.

3.4.3 Noisy data

When dealing with real diffusion tensor images (DTI), noise is one factor that should be taken into account. To test the behavior of the TMG in presence of noise, random Gaussian noise was added independently to the three eigenvalues of the synthetic tensor field (torus) in addition to random rotation (in azimuth and elevation) perturbing the three eigenvectors by the same amount to retain orthogonality. This noise addition method adopted here was first reported by Weldeselassie in [Weldeselassie and Hamarneh, 2007]. In fact, addition of random noise was reported by several DTI segmentation works ([Jonasson et al., 2003], [Rousson et al., 2004], [Wang and Vemuri, 2005], [Freidlin et al., 2007]), and although the parameters of the noise and the way it is added to tensors

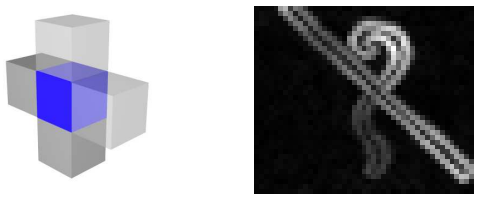

(a) 4-connected (2D) (b) 4-connected TMG

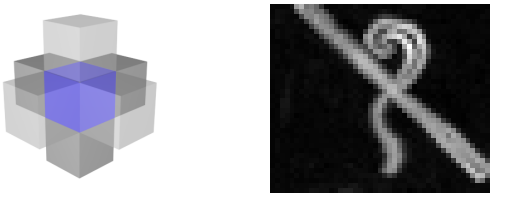

(c) 6-connected (3D) (d) 6-connected TMG

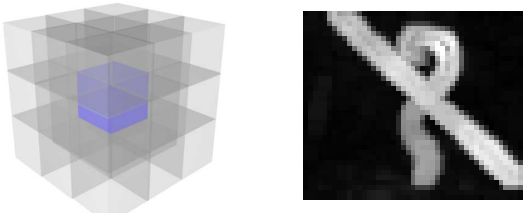

(e) 26-connected (3D) (f) 26-connected TMG

Fig. 3.5: Different structuring elements and resulting TMGs using each one of the structuring elements

vary considerably, the main idea behind is the same. The purpose is not to simulate real noisy data, but to test the robustness of the segmentation methods in the presence of noise.

Fig. 3.6(a) and Fig. 3.6(b) show one slice of the synthetic tensor field without and with noise, respectively. Results of the TMG computed using the Frobenius norm for the synthetic torus without and with noise can be seen in Fig. 3.6(c) and Fig. 3.6(d). Despite of the noise added to the tensor field, the obtained TMGs preserved all relevant information, in this case, the borders.

3.5 Segmentation of diffusion tensor images

Diffusion tensor image segmentation is a challenging task exactly because it has as input a tensorial image and the segmentation method has to decide which information should be considered in segmentation. Furthermore, either existing segmentation methods have to be adapted to deal with tensorial information or completely new segmentation methods have to be developed to accomplish

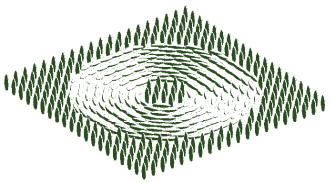

(a) Without noise

(b) With gaussian noise

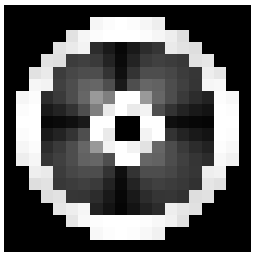

(c) TMG of torus

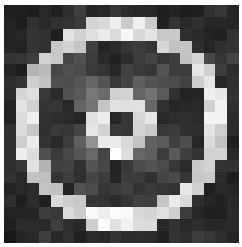

(d) TMG of noisy torus

Fig. 3.6: One slice of the torus without and with noise and resulting TMGs

this task. Alternatively, what this work proposes is the computation of a gradient, that transforms the diffusion tensor image into an scalar image, and makes possible the use of any existing method in order to perform the segmentation.

To address the DTI segmentation problem, the IFT-based watershed transform was the method of choice in the field of mathematical morphology. The image foresting transform (IFT) may be seen as a generic approach to project image processing operators, unifying methods such as fuzzy connectedness, watershed transforms, connected operations, distance transforms, and boundary tracking, normally with efficiency gains [Falcão et al., 2001].

In summary, the IFT [Falcão et al., 2004] models the image as a graph, and starting from a given set of seed pixels, uses a given path cost function to partition the image into a minimum-cost path forest. The IFT outputs three parameters for every input pixel, namely: a label corresponding to the closest seed pixel; the predecessor, or parent pixel, in the path; and the cost of that path from the seed up to the pixel. Different IFT-based applications normally use one or a combination of these parameters. In IFT-based watershed transforms [Lotufo and Falcão, 2000] the label image represents the influence zones of all the seeds in the optimal image partition.

Fig. 3.7 illustrates the use of the tensorial morphological gradient and the watershed transform to segment diffusion tensor images. The computed TMG shown in Fig. 3.7(a) was obtained using a

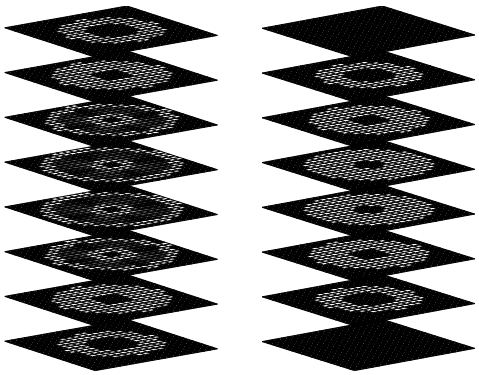

(a) TMG (b) Segmentation result

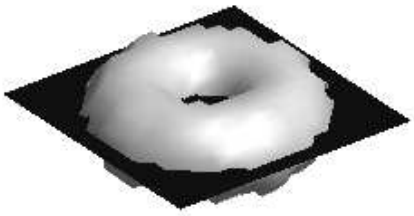

(c) Rendered segmentation result

Fig. 3.7: Computed TMG and watershed segmentation result for a synthetic tensor field (torus) using a 6-neighbor (3D) as the structuring element

3D 6-connected structuring element and the Frobenius norm as the tensorial similarity measure. The segmentation was then performed by the watershed transform from markers and its result can be seen in Fig. 3.7(b). Here the markers used were the regional minima of the TMG. Fig. 3.7(c) shows the rendered segmentation result.

Although this procedure of computing the TMG of the tensor field and then segmenting it using the watershed transform works well, depending on the data to be segmented, another segmentation method could obtain better results. Fig. 3.8(a) shows the TMG computed for the real data set already presented in Section 3.4.1 (Fig. 3.4(a)). Because the data is composed of thin objects (rat spinal cords), the watershed transform encounters some difficulties, like, for example, finding inner markers. In this case, segmenting by choosing a simple threshold turns out to be more efficient than using the watershed transform. Fig. 3.8(b) presents the segmentation result using 40 as the threshold value.

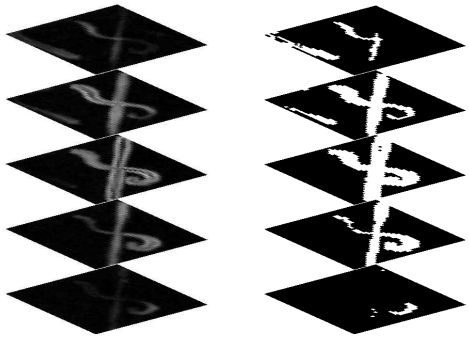

(a) TMG (b) Segmentation result

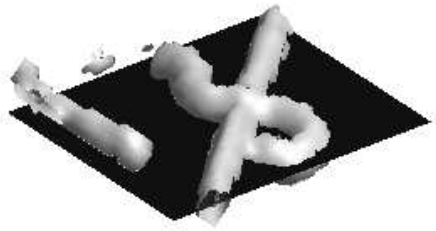

(c) Rendered segmentation result

Fig. 3.8: Computed TMG and threshold segmentation result for real data (rat spinal cords phantom) using a 6-neighbor (3D) as the structuring elements

3.6 Conclusions

This paper proposes the tensorial morphological gradient (TMG) computation of diffusion tensor images, in order to segment them. The TMG processes the tensorial information and transforms it into a scalar image, making possible the use of well known operators from mathematical morphology to segment tensorial images. Experiments were conducted using synthetic and real tensor fields. Distinct similarity functions and structuring elements were tested, and segmentation performed well in all instances.

The strength of the proposed segmentation method is its simplicity and robustness, consequences of the tensorial morphological gradient computation. It enables the use, not only of well known algorithms and tools from the mathematical morphology, but also of any other segmentation method to segment DTI, since the computation of the tensorial morphological gradient transforms tensorial images into scalar ones.

Acknowledgments

The authors would like to thank Jennifer Campbell of the McConnell Brain Imaging Centre, Montreal Neurological Institute, McGill University, for the real DTI data sets.

Capítulo 4

Segmentação de imagens de tensores de difusão do cérebro

O artigo "Segmentation of brain structures by watershed transform on tensorial morphological gradient of diffusion tensor imaging" [Rittner et al., 2009a] apresentado neste capítulo foi publicado nos anais do *XXII Simpósio Brasileiro de Computação Gráfica e Processamento de Imagens - SIBGRAPI'09*. Ele comprova a validade do método de segmentação de imagens de tensores de difusão utilizando-se o gradiente morfológico tensorial e a transformada de *watershed*. Para tanto, imagens de tensores de difusão do cérebro foram utilizadas e diversas estruturas cerebrais foram segmentadas.

A segmentação resultante foi ainda comparada com um método de segmentação automático baseado em atlas e em imagens de ressonância magnéticas ponderadas em T1 e T2, além de imagem de densidade de próton (PD). A comparação mostra que a segmentação obtida pela transformada de *watershed* aplicada ao TMG é consistente com a segmentação baseada em atlas.

Além disso, fez-se também uma comparação do método proposto com os demais métodos de segmentação baseados em DTI, desta vez, não quanto aos resultados obtidos, mas quanto à necessidade de escolha dos parâmetros de inicialização e à necessidade de interação do usuário. O método baseado no TMG é o que menos requer ajuste por conta do usuário, bastando escolher o número de regiões em que se quer segmentar a imagem de tensores de difusão.

4.1 Abstract

Watershed transform on tensorial morphological gradient (TMG) is a new approach to segment diffusion tensor images (DTI). Since the TMG is able to express the tensorial dissimilarities in a single scalar image, the segmentation problem of DTI is then reduced to a scalar image segmentation

problem. Therefore, it can be addressed by well-known segmentation techniques, such as the watershed transform. In other words, by computing the TMG of a DTI, and then using the hierarchical watershed transform, it is possible to segment brain structures, such as the corpus callosum, the ventricles and the cortico-spinal tracts, and use the results for subsequent quantitative analysis of DTI parameters. Experiments showed that segmentations obtained with the proposed approach are similar to the ones obtained by other segmentation techniques based on DTI and also segmentation methods based on other Magnetic Resonance Imaging (MRI) modalities. Since the proposed method, as opposed to the majority of the DTI based segmentation methods, does not require manual seed and/or surface placement, its results are highly repeatable. And unlike other methods that have sometimes four parameters to be adjusted, the only adjustable parameter is the number of regions in which the image should be segmented, making it simple and robust.

4.2 Introduction

Diffusion tensor imaging (DTI) is a relatively new Magnetic Resonance Imaging (MRI) modality of able to quantify the anisotropic diffusion of water molecules in highly structured biological tissues. It is unique in its non-invasive ability to quantify changes in neural tissue microstructure within the human brain.

Delineation of a region of interest (ROI) is usually necessary for performing subsequent quantitative analysis of DTI. However methods for delineate the ROI are normally manual and subjective, very time consuming and requiring considerable expertise.

Usually, when acquiring DT-MRI of a subject, other MR images are also acquired, such as T1-weighted and T2-weighted MRI. Therefore, one option to delineate a region of interest in DT images, is to perform the segmentation of structural images, such as T1-weighted or T2-weighted segmentation, for which several algorithms are available [Broit, 1981, Kapouleas, 1990, Gerig et al., 1991, Brummer et al., 1993, Miller et al., 1993, Collins et al., 1995, Collins et al., 1999]. Then, by registering the DT image to the T1 or T2 image, is possible to use the result of the segmentation made on T1 or T2 to segment the DT image.

Without a doubt, it would be desirable to have a method that segment directly the DTI, instead of segmenting it indirectly, based on T1 or T2 weighted images. First of all, because it would not be necessary to acquire T1 or T2 weighted images. Second, because segmentation methods based on T1 or T2 are not trivial and are usually time consuming. In addition, registration of segmentation result to DT images introduces errors.

Initially several DTI segmentation methods were proposed to address the problem of finding individual fiber paths. Only in the last decade recent papers have addressed the problem of region

based segmentation of DT-MRI.

Zhukov *et al.* in [Zhukov et al., 2003] applied a level-set modeling and segmentation techniques to the derived scalar volumes to create geometric models of specific brain structures. The geometric models were then used for quantitative analysis, including volume and surface area calculations. Their level set segmentation approach consisted of defining a set of suitable preprocessing techniques for initialization and selecting/tuning different feature-extracting terms in the level set equation to produce a surface deformation. Because level set models move using gradient descent, they seek local solutions, and therefore the results are strongly dependent on the initialization, i.e., the starting position of the surface. Additionally this method fails to distinguish between regions with same diffusion anisotropy magnitude but oriented in different directions.

Zhizhou and Vemuri [Wang and Vemuri, 2005] proposed also a DTI segmentation based on a level-set curve evolution technique, that operates on the diffusion tensor fields. However, these variational formulations with iterative gradient descent based solutions are sensitive to parameter settings and initialization, and hence may get stuck at suboptimal local minima of the energy functional.

Another level-set based front-propagation scheme was presented by Jonasson *et al.* [Jonasson et al., 2005], in which the front propagates to a new voxel based on the similarity between the tensor at that voxel and a few tensors inside the current segment lying along the surface normal. Such an approach might encounter problems at sharp bends in thin tracts like, for example, the cingulum.

In [Weldeselassie and Hamarneh, 2007], Weldeselassie and Hamarneh extended the graph cuts scalar field segmentation technique proposed by Boykov and Jolly [Boykov and Jolly, 2001] to DTI. In their extension, the graph vertices correspond to the tensor voxels in the DT-MR image and the graph connectivity edge weights are computed using tensor dissimilarity metrics. Seed points provided by the user give clues about the location of the object of interest and the background and often, the user needs to interactively modify the seed points in order to improve the segmentation results.

Lenglet *et al.* [Lenglet et al., 2006] presented a statistical surface evolution framework for the segmentation of diffusion tensor images and introduced a Riemannian distance measure between tensors, modeling each class by a single Gaussian in the Riemannian space. The proposed method extends their modeling approach by incorporating a generic nonparametric model for each class that is able to accurately model tensor statistics in fiber bundles.

Recently, Niogi *et al.* [Niogi et al., 2007] proposed a semiautomated region-growing and chain-linking to produce 3D regions of interest of white matter tracts without explicitly performing fiber tracking. It fails to segment a structure that contains a lesion, since it will not select cerebrospinal

fluid or gray matter as boundary pixels. And because it was designed to terminate segmentation when the principal direction of diffusion changes to an orthogonal direction, in structures with high curvature areas, its segmentation will terminate prematurely.

All cited algorithms require previous knowledge of the structure to be segmented and depend on seed placement, initial surface delineation and/or parameter adjustments, making the segmentation process very susceptible to initialization.

In order to reduce the influence of user choices, what this work proposes is a segmentation algorithm based on the watershed transform and the tensorial morphological gradient (TMG) of a diffusion tensor image (DTI). The tensorial morphological gradient was first applied to segment tensorial images representing color images [Rittner et al., 2007] and then, its concept was extended and applied to synthetic diffusion tensor images [Rittner and Lotufo, 2008]. It computes the tensorial morphological gradient based on the similarity between tensors and segments it using the watershed transform. The only parameter to be chosen is the number of regions in which the image should be segmented.

This paper is organized as follows: Section 4.3 describes the DTI segmentation algorithm based on TMG and compares it to other DTI segmentation methods . Section 4.4 presents the segmentation of brain structures, such as the corpus callosum, the ventricules and the cortico-spinal tract. Finally, conclusions are summarized in Section 4.5.

4.3 DTI Segmentation of brain structures

Diffusion tensor image segmentation is a challenging task exactly because it has as input a tensorial image and the segmentation method has to decide which information should be considered for segmentation purposes. Furthermore, either existing segmentation methods have to be adapted to deal with tensorial information or completely new segmentation methods have to be developed to accomplish this task. Alternatively, what this work proposes is the computation of a gradient, that transforms the diffusion tensor image into an scalar image, and makes possible the use of a wide range of existing segmentation methods in order to perform the segmentation. In this case, the segmentation method chosen to accomplish the task was the hierarchical watershed transform.

4.3.1 TMG based segmentation

The present work proposes the computation of the tensorial morphological gradient (TMG) of a diffusion tensor image (DTI) as the initial step to segment it. Inspired on the morphological gradient, a tensorial morphological gradient (TMG) was defined and first described in [Rittner et al., 2007]. It

was used at that time, together with a tensorial representation of colors, to segment color images. In [Rittner and Lotufo, 2008], the concept was expanded, applying it to segment synthetic diffusion tensor images.

The morphological gradient is one of the several existing gradients used in image processing to detect edges and depends on the size and shape of the chosen structuring element. Using a flat structuring element at each point, the morphological gradient yields the difference between the maximum and the minimum values over the neighborhood at the point determined by the flat structuring element [Heijmans, 1994]. The use of a three-dimensional structuring element leads to a morphological gradient that takes into account the neighborhood in all directions, and not only in an specific plane.

Let $E = \mathbb{Z} \times \mathbb{Z}$ be the set of all points in the tensorial image f. The tensorial morphological gradient (TMG) is defined by

$$\nabla_B^T(f)(x) = \bigvee_{y,z \in B_x} d_n(\mathbf{T}_y, \mathbf{T}_z), \tag{4.1}$$

$\forall x \in E$, where $\bigvee$ is the supremum of a subset, $B \subset E$ is a structuring[1] element centered at the origin of E, d_n represents any of the similarity measures presented in DTI literature [Pierpaoli and Basser, 1996, Alexander et al., 1999, Jones et al., 1999, Wiegell et al., 2003, Wang and Vemuri, 2005, Ziyan et al., 2006], $\mathbf{T}_y$ is the tensor that represents the diffusion in y, and $\mathbf{T}_z$ is the tensor that represents the diffusion in z (y and z are in the neighborhood of x, defined by E[2]). ∇_B^T is the proposed TMG.

Once the tensorial information is translated into a scalar image, namely the TMG, the next step is to segment it using the watershed transform from markers [Beucher and Meyer, 1992, Vincent and Soille, 1991].

The critical part in the watershed segmentation is the proper choice of markers. The classical watershed places the markers automatically in each regional minima of the image. This usually leads to a over-segmentation and is not adequate for medical imaging applications. To solve the over-segmentation problem, hierarchical approaches are considered in order to retain the most significant regions of the image at different scales [Meyer, 2001].

The dynamics of the regional minima have been used to build the hierarchy. Essentially, this hierarchy can be interpreted as a set of region adjacencies, wherein an ordering is determined by a valuation, which can be controlled by the relative altitudes of the regional minima. The contrast dynamics of a regional minimum is defined as the minimal climb required for a path starting from a regional minimum to reach another one with strictly lower altitude, the climb being the difference

[1] errata: "structuring" substitui "structured" (versão publicada)

[2] errata: "B_x" substitui "E" (versão publicada)

in altitude between the highest point of the path and the regional minimum under study. Regional minima with highest dynamics will be used as markers for watershed segmentation.

In this work, after calculating the TMG of the original image, the n structures in the image which has the greatest volume extinction values are automatically selected. The n markers assigned to these regions are then used in the watershed transform, which segmented the TMG in n regions.

4.3.2 Comparison to other DTI segmentation methods

As described in Section 4.2, a few region based segmentation of DT-MRI have been proposed in the last decade, most of them based on level-set, statistical surface evolution and region growing techniques. Some of them were designed to segment only fiber bundles, while others focused on segmenting white matter structures, such as the corpus callosum and the cortico-spinal tract.

Considering some of the most recent techniques that were proposed in the literature to segment the corpus callosum, an analysis of the requirements of each algorithm was done and summarized below, in an effort to demonstrate the strength of the proposed methodology regarding initialization and parameters dependency.

Jonasson *et al.* [Jonasson et al., 2005] proposed a front propagation algorithm to segment white matter fiber tract based on DTI. To perform the segmentation a initial surface has to be placed inside the tract to be segmented. The surface is then propagated using a chosen similarity measure. A curvature dependent speed is added to regularize the flow and its weighting parameter have to be assigned. Also, a threshold value for the speed is necessary, to prevent unwanted propagation.

In [Lenglet et al., 2006], Lenglet *et al.* proposed a surface evolution algorithm for DTI segmentation that also requires a initialization of the surface evolution. It addresses the segmentation problem as the maximization of a posteriori segmentation probability. There are two parameters that have to be chosen: the first one is the value of ν in the term that expresses the probability of the interface to represent the structure of interest. It constrains the smoothness of the surface and is usually set in the range 1 to 10. The second parameter is a threshold for the variance which, whenever reached, induces the end of the update for the statistical parameters.

To segment a white matter structure by the semi-automated segmentation method proposed in [Niogi et al., 2007], first one has to select a pixel within the structure to be segmented, that will be used as a sample of the structure. Second, the computation of a magnification array requires values selection for the three constants α, β and γ. Then, pixels are labeled, after being transformed by this magnification matrix and according to a threshold value, that also has to be chosen.

Table 4.1 summarizes the requirements and limitations of each segmentation method. While all the other DTI segmentation methods cited here require seed placement or initial surface delineation, there is no initialization needed in the proposed method. Moreover, the segmentation technique

based on the TMG has as only input parameter the number of regions to segment, in opposition to 2 required parameters in [Jonasson et al., 2005] and [Lenglet et al., 2006], and 4 parameters in [Niogi et al., 2007].

It is important to point out that the choice of a different number of regions n does not mandatorily deteriorate the segmentation result. At best, the segmentation of the desired structure could be not affected at all. Otherwise, a lower number of regions would make the desired structure to be merged with an adjacent structure. In that case, the user would have to run the watershed again, increasing the number of regions. In the other hand, a higher number of regions would only cause the desired structure to receive two or more distinct labels instead of only one. In this case, the user would only have to group the respective labels in order to obtain the whole structure.

Tab. 4.1: Requirements of DTI-based segmentation methods

	Jonasson [Jonasson et al., 2005]	Lenglet [Lenglet et al., 2006]	Niogi [Niogi et al., 2007]	TMG
Initial surface	yes	yes	no	no
Seed pixel	no	no	yes	no
Nr. of parameters	2^a	2^b	4^c	1^d
Postprocessing	no	no	yes	yes
Designed for	white matter	white matter	white matter	all

[a] regularization weighting parameter and threshold for the speed
[b] smoothness of the surface and threshold for the variance
[c] constants of magnification array and threshold for diffusion components
[d] number of regions

4.4 Results

4.4.1 MRI data acquisition and preprocessing

The data used in our experiments were acquired on a Siemens 3T Trio MR scanner (Siemens Medical Systems, Erlangen, Germany) using an 8-channel phased array head coil. Diffusion encoding was achieved using a single-shot spin-echo echo planar sequence with twice-refocused balanced diffusion encoding gradients. The datasets acquired contained: a T1 weighted image, 176 slices, 1 mm isotropic voxel size, TE = 2.98 ms, TR = 2.3 s; a T2 weighted image, 77 slices, 1.0 mm ×1.0 mm ×2.0 mm, TE = 84ms, TR = 14.6 s and a PD image [3], 77 slices, 1.0 mm ×1.0 mm ×2.0 mm, TE = 19 ms, TR = 3.2 s; diffusion images with $N = 30$ diffusion encoding directions with 63 slices, 2.0 mm ×2.0 mm ×2.0 mm, TE = 95 ms, TR = 8.7 s and $b = 1000$s/mm^2 (the b value describes

[3] An MR image dependent primarily on the density of protons in the imaging volume. Proton density contrast is a quantitative summary of the number of protons per unit tissue.

the degree of diffusion weighting, determined by the duration and strength of the sensitizing pulsed gradients in the MR experiment).

The diffusion data was first linearly interpolated before tensor estimation. The **MINC tools** from the Montreal Neurological Institute, McGill University, were used for all diffusion image preprocessing.

4.4.2 TMG computation and segmentation results

In our segmentation experiments the TMG of the DTI was computed using the Frobenius Norm as the similarity measure and the hierarchical watershed was then used to segment desired structures of the brain. The watershed transform, the extinction functions and other morphological functions used can be found in the "SDC Morphology Toolbox for MATLAB" [Dougherty and Lotufo, 2003]. The TMG computation and the segmentation algorithm was implemented in MATLAB 7.0 .

Fig. 4.1 shows one slice of the tensorial information, already cropped around the desired structure (corpus callosum) and overlayed on a T1-weighted image. The information contained in each pixel in the front image is the ellipsoid representing each diffusion tensor, colored according to the orientation of the principal eigenvectors. Although it is possible to distinguish the corpus callosum by observing the ellipsoids in Fig. 4.1, it is not obvious to automatically segment it without giving any prior information, specially because one have to deal with a tensorial information, containing both magnitude and direction of the diffusion.

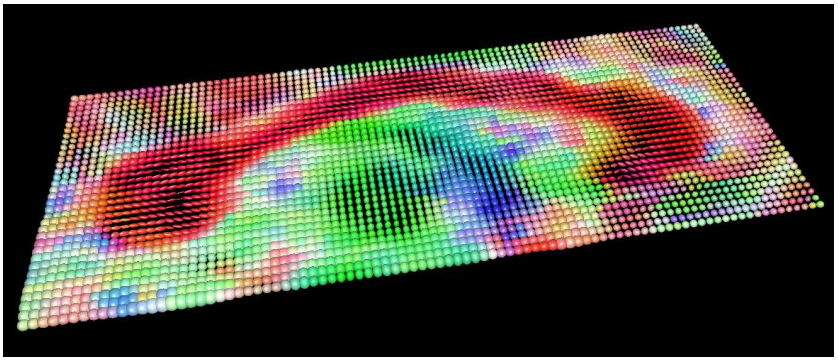

Fig. 4.1: Ellipsoids representing the diffusion tensors in the region containing the corpus callosum

To automatically segment the corpus callosum shown in Fig. 4.1, first the tensorial morphological gradient (TMG) was computed using the Frobenius Norm as the tensorial similarity measure. The structuring element chosen to define the neighborhood to be considered in the TMG computation was a 6-connected structuring element (3D). Once computed, the TMG was then used by the watershed transform to segment the corpus callosum. The used criteria to chose the watershed markers was to fix the number of regions, in which the image should be segmented. In this specific case, markers

were imposed to the basins with the 60 greatest volume extinction values, i.e., the watershed operator segmented the TMG of the DTI in the 60 most significant regions.

Fig. 4.2 presents three steps of the segmentation process: Fig. 4.2(a) shows one slice of the computed TMG, Fig. 4.2(b) contains the same slice labeled according to the watershed result and Fig. 4.2(b) depicts finally the 3D segmentation result. As can be seen in Fig. 4.2(a) the TMG was able to detect the borders of the corpus callosum, and the dark area inside it shows that the diffusion tensors inside this structure are very homogenous, leading to a very low gradient. Fig. 4.2(b) shows the labels assigned to one slice by the watershed transform, where each color represents one label. The watershed transform was able to assign one single label to the corpus callosum, in this case, the dark red area in the upper part of the image.

It is important to notice that, although Fig. 4.2(a) and Fig. 4.2(b) depicts only one slice of the TMG and of the watershed result, the TMG and the watershed transform were computed taking into account the three-dimensional information. This is guaranteed by the choice of the structuring element (in this case, a 6-connected structuring element). For another specific application or structure, a bi-dimensional structuring element could be more adequate. This could be easily chosen by the user without any modification of the algorithm. Finally, Fig. 4.2(c) shows the whole segmented volume (3D result), from which is possible to conclude that the hierarchical watershed successfully segmented the corpus callosum.

To confirm our segmentation result, we segmented the corpus callosum of the same subject using the ANIMAL+INSECT [Collins et al., 1999], an algorithm for improved automatic segmentation of gross anatomical structures of the human brain. It merges the output of a tissue classification process (INSECT) with gross anatomical region masks, automatically defined by non-linear registration of a given data set with a probabilistic anatomical atlas (ANIMAL). The ANIMAL (Automated Non-Linear Registration Package for Stereotaxic Transformation of MRI data) is a completely automatic method, based on multi-scale, three dimensional (3D) cross-correlation, to non-linearly register two MRI volumes together [Collins et al., 1995]. Instead of using diffusion images to perform the segmentation, it combines information from T1, T2 and PD images to accomplish the task.

In Fig. 4.3 results from the TMG segmentation and from the ANIMAL+INSECT segmentation are presented. Segmentation results are similar, although the first was based on the diffusion data Fig. 4.3(a) and the second on the T1, T2 and PD images Fig. 4.3(b). By plotting both segmentation results in the same figure (Fig. 4.3(c)) it is possible to confirm their consistency. It is important to point out that the segmentation result of the ANIMAL+INSECT method is not the ground truth, and it was used only for comparison purposes.

Fig. 4.4 depicts what happens when the user chooses a higher number of regions ($n = 100$). Even though the corpus callosum was segmented in three distinct regions, is still possible to distinguish it

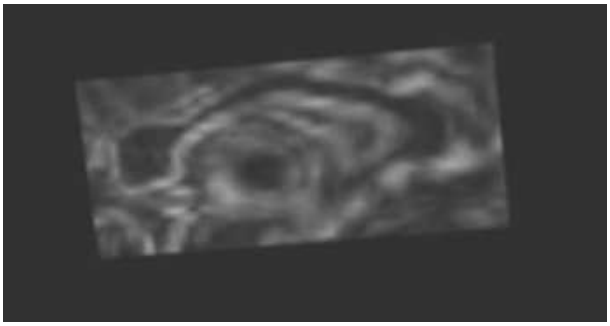

(a) Tensorial morphological gradient (TMG)

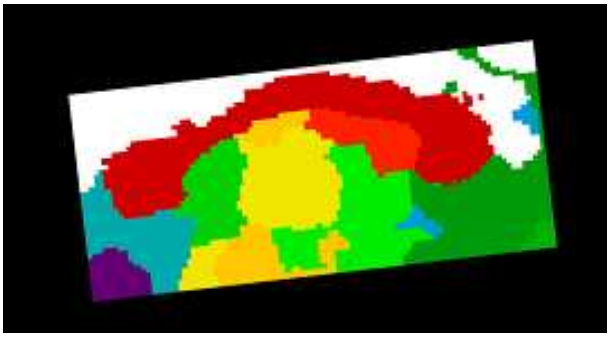

(b) Resulting labeled regions from Watershed on TMG

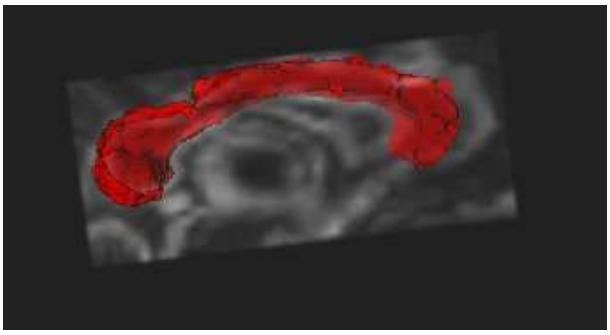

(c) Corpus callosum (3D) segmented by the watershed on the TMG

Fig. 4.2: Segmenting the corpus callosum: the computed TMG (one slice), the hierarchical watershed transform (one slice) and the 3D segmentation result

as one structure by selecting all three regions and throwing away the rest.

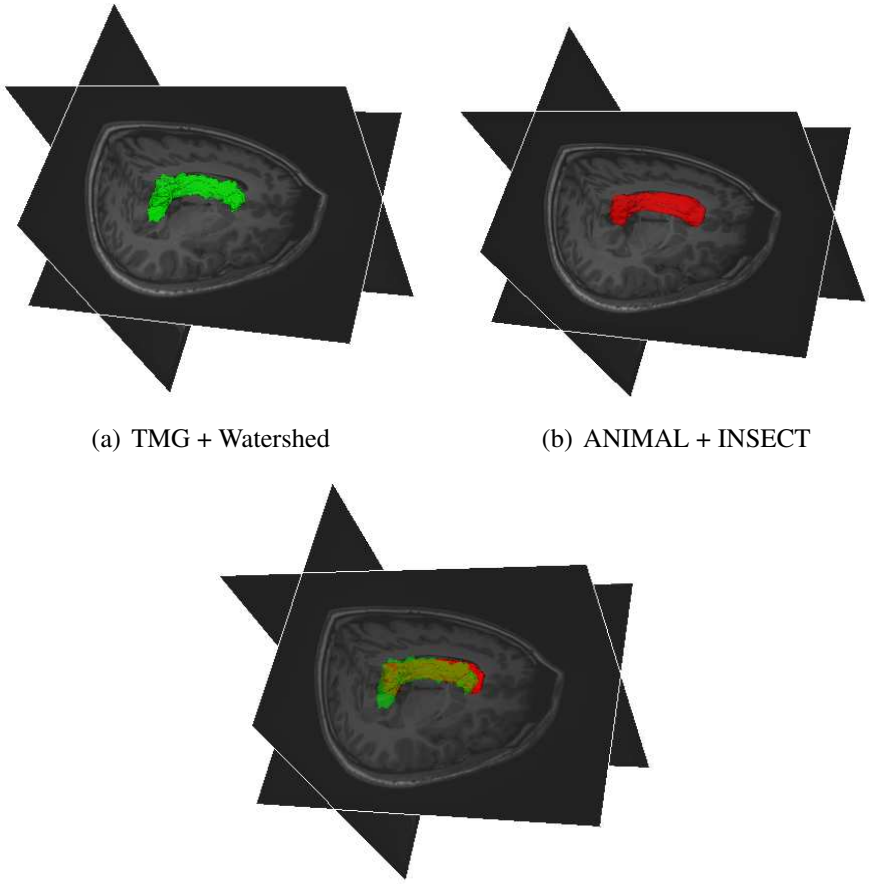

(a) TMG + Watershed (b) ANIMAL + INSECT

(c) Both results (overlaid)

Fig. 4.3: Comparison of corpus callosum obtained by different segmentation methods: In green, the TMG + Watershed performed on DTI and in red, the ANIMAL + INSECT performed on T1, T2 and PD images

The same experiment was repeated with different subjects to segment the corpus callosum. In all cases, the corpus callosum was successfully segmented from DTI and the results were comparable to the results of ANIMAL+INSECT algorithm. Similar experiments were also conducted in order to segment distinct brain structures.

Fig. 4.5 shows the 3D segmentation result of the ventricles. Again, the TMG was computed using the Frobenius Norm as the similarity metric and a 6-connected structuring element. By choosing the same number of regions ($n = 60$) used for the corpus callosum, the proposed algorithm was able to segment the left and right ventricles. Although segmenting the ventricles could be eventually accomplished by a threshold applied in a fractional anisotropy (*FA*) map, their separation in right and left ventricles would not be straightforward.

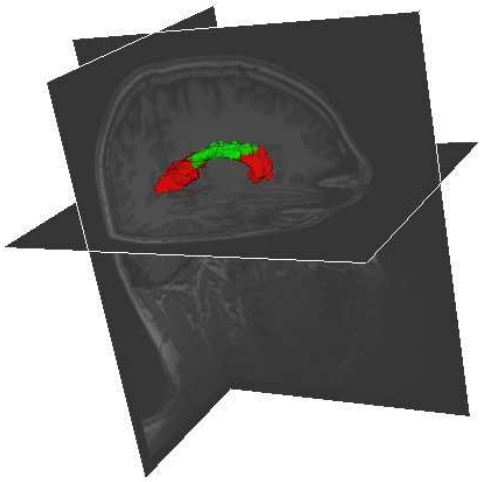

Fig. 4.4: 3D segmentation result of corpus callosum, when increasing the number n of regions. Instead of only one label, three labels were assigned to the corpus callosum by the watershed transform.

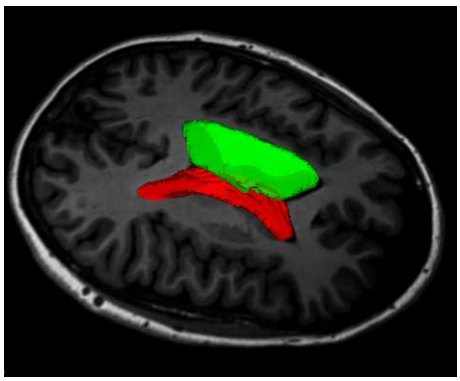

(a) ANIMAL

Fig. 4.5: Left and right ventricles, segmented by the watershed transform on the TMG

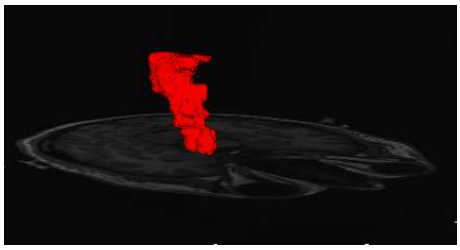

Fig. 4.6: Segmentation of cortico-spinal tract by the proposed method

Fig. 4.6 presents the result for the cortico-spinal tract segmentation. It was done by TMG computation using the Frobenius Norm and new markers were placed in the 120 most significant regions of the image. Again, the hierarchical watershed transform was used to perform segmentation and the obtained result is as expected.

Because there is no gold standard available for comparison, a quantitative assessment is difficult. All segmentation results were visually compared with neuroanatomical atlas, results from the ANIMAL+INSECT algorithm and results from papers cited in Subsection 4.3.2. From this comparison it is possible to confirm that the proposed algorithm succeed segmenting the above mentioned structures.

4.5 Conclusions

This paper proposes the segmentation of brain structures by running the watershed transform over the tensorial morphological gradient (TMG) computed from diffusion tensor images. The TMG processes the tensorial information and transforms it into an scalar image, making possible the use of the hierarchical watershed to segment it. As opposed to other DTI based segmentation algorithms, the proposed method requires no manual seed placement and/or initial surface delineation. The only parameter is the number of regions in which the image should be segmented, in contrast to other methods, that require sometimes 4 parameters to perform segmentation. Experiments with real DTI were conducted, where different brain structures, such as the corpus callosum, the cortico-spinal tracts and the ventricles, were successfully segmented.

Capítulo 5

Mapas escalares de difusão

O artigo apresentado neste capítulo, cujo título é "Segmentation of diffusion tensor fields based on scalar maps and mathematical morphology", submetido ao periódico *IEEE Transactions on Medical Imaging*, descreve as diversas medidas escalares de difusão, sob a perspectiva da segmentação.

Em uma primeira etapa, o artigo faz uma revisão das medidas intra e intervoxel já existentes, agrupando-as e listando suas principais características. Esta análise não só leva a uma melhor compreensão dos mapas escalares já propostos na literatura, como aponta suas deficiências e dá indícios de como estes mapas poderiam ser adaptados para melhor atender à tarefa de segmentação.

Em seguida, duas abordagens para a utilização de conceitos da morfologia matemática no problema de segmentação de DTI são apresentadas. A primeira delas propõe o cálculo de gradiente morfológico de medidas de difusão intravoxel, como a difusividade média (*DM*) e anisotropia fracional (*FA*), entre outras. Como as imagens das medidas de difusão intravoxel são escalares, a definição clássica de gradiente morfológico pode ser utilizada. A segunda abordagem prevê o uso das medidas de difusão intervoxel, como por exemplo o produto escalar (DP) e o índice de reticulado (LI), como base para o cálculo do gradiente morfológico tensorial.

Ambas abordagens oferecem como produto final uma imagem de gradiente que pode servir como base para o uso de métodos de segmentação convencionais, desde uma simples limiarização até a transformada de *watershed*. A questão é então a escolha da combinação *medida + gradiente + método de segmentação* mais adequada para segmentar a estrutura que se deseja.

5.1 Abstract

This paper describes an approach to perform diffusion tensor fields segmentation using the watershed transform. Instead of adapting the existing segmentation method to tensorial images, the idea is to transform the tensorial image into a scalar map and then apply the original technique.

A comparison between existing intravoxel and intervoxel measures is conducted, concerning segmentation purposes. New scalar maps, inspired on mathematical morphology concepts and on the tensorial morphological gradient (TMG), are proposed and also included in the comparison, confirming their superiority. Watershed transform is then applied to segment some structures of the brain, based on the computed scalar maps.

5.2 Introduction

Diffusion tensor imaging (DTI) is a relatively new modality of MRI able to generate contrasts that are sensitive to fiber orientations. It carries rich information about intra-white-matter axonal anatomy, which cannot be seen in conventional MRI. DTI-based segmentation, where regions of interest are delineated, is necessary for performing subsequent quantitative analysis and qualitative visualization. While scalar image segmentation has been studied extensively and different algorithms have been developed over the last decades, DTI-based segmentation is a relatively new and challenging task.

The use of DTI properties to perform the clustering of brain tissue was initially described by Pierpaoli *et al.* [Pierpaoli and Basser, 1996]. More recently, DTI-based clustering strategies have been described [Zhukov et al., 2003, Wang and Vemuri, 2005, Lenglet et al., 2006, Ziyan et al., 2006, Weldeselassie and Hamarneh, 2007, Awate and Gee, 2007, Niogi et al., 2007] and have been applied in many studies, including the thalamic nuclei [Wiegell et al., 2003, Johansen-Berg et al., 2005, Ziyan et al., 2006, Duan et al., 2007, Jonasson et al., 2007], the thalamocortical projections [Behrens et al., 2003] and the fetal brain [Maas et al., 2004]. Although the strategies are based in well-known segmentation algorithms, such as level-sets, region growing and graph-cuts, they were actually developed exclusively for DTI. Significant modifications in the original algorithms, conceived to work with scalar images, had to be done in order to deal with tensorial information.

Instead of defining a new segmentation method, this work proposes to explore and transform diffusion tensor data into scalar maps and then, use these scalar maps, together with the watershed transform, to segment diffusion tensor fields. The watershed transform is a region-based segmentation approach and has been successfully applied to the solution of many medical imaging problems, such as the segmentation of blood cells [Falcão et al., 2001], neuromorphometry [Falcão et al., 2002] and characterization of human cortex [Rettmann et al., 2002, Castellano et al., 2003]. It is a powerful segmentation method, simple and efficient, that does not require, neither previous knowledge of the structures to be segmented, nor surface initialization or manual seed placement.

A crucial step of the watershed-based segmentation is the computation of a gradient of the image to be segmented. A gradient can be seen as a scalar map that contains edge information. In the

diffusion tensor field context, it is desirable that the gradient help to find edges between regions with distinct diffusion characteristics. In other words, the gradient should be strong where diffusion changes are significant and weak where diffusion changes are imperceptible.

Several scalar maps based on diffusion measures can be found in the literature. Among the intravoxel measures are the mean diffusivity (*MD*), the fractional anisotropy (*FA*) and the volume ratio (*VR*). Other measures, such as the lattice index (*LI*) and the coherence index (*CI*) can be classified as intervoxel measures. It is important to point out that none of the cited scalar maps were conceived for segmentation purposes and, therefore, do not necessarily contain enough information to distinguish regions with distinct diffusion characteristics.

In previous work [Rittner and Lotufo, 2008], a tensorial morphological gradient (TMG) was presented as a technique to transform the diffusion tensor image into a scalar map with meaningful values to detect borders between brain structures. The tensorial morphological gradient uses diffusion intervoxel measures and combines them to compute a gradient using concepts from mathematical morphology.

In order to choose a convenient scalar map to be used by the watershed transform, this work classifies the existing scalar maps as intra or intervoxel measures and analyzes them, taking into account their adherence to the segmentation task. Based on this analysis, new scalar maps are proposed by combining mathematical morphology operators and existing measures. Segmentation experiments using the watershed transform help to understand the main differences between scalar maps. They also show that the choice of scalar map to perform the segmentation by watershed should be based on the diffusion characteristics of the brain structure to be segmented.

This paper is organized as follows: Section 5.3 presents intravoxel DTI measures used for quantitative analysis of diffusion. Section 5.4 describes intervoxel measures, classified into *distances*, *neighborhood measures* and *gradients*. The experiments are described in Section 5.5 and results are presented in Section 5.6. Finally, Section 5.7 discusses the obtained results and Section 5.8 concludes the paper.

5.3 Intravoxel diffusion measures

Several properties of the diffusion tensor are rotationally invariant and are useful in deriving quantitative information from the diffusion tensor and in comparing different tensors and ellipsoids. The most simple invariant measures obtained from DTI is the trace and the mean diffusivity of the diffusion tensor. The trace (T) is the sum of the three diagonal elements of the diffusion tensor (i.e. $Dxx + Dyy + Dzz$), which can be shown to be equal to the sum of its three eigenvalues:

$$T = \lambda_1 + \lambda_2 + \lambda_3. \tag{5.1}$$

Furthermore, the mean diffusivity (*MD*) is defined as:

$$MD = \frac{\lambda_1 + \lambda_2 + \lambda_3}{3} = \frac{\mathbf{T}}{3}. \tag{5.2}$$

Another simple kind of rotationally invariant measure is the 'diffusion anisotropy index' or DAI, that gives an idea of the degree of anisotropy of a given diffusion tensor. The common DAIs range from 0 to 1 and do not require eigenvalue sorting. The simplest anisotropy index is the variance of the three eigenvalues about their mean. The variance alone, however, needs to be normalized to account for regional differences in the overall magnitude of diffusivity. The most popular index based on this logic is the fractional anisotropy (*FA*) [Basser and Pierpaoli, 1996] given by:

$$FA = \sqrt{\frac{3}{2}} \frac{\sqrt{(\lambda_1 - MD)^2 + (\lambda_2 - MD)^2 + (\lambda_3 - MD)^2}}{\sqrt{\lambda_1^2 + \lambda_2^2 + \lambda_3^2}}, \tag{5.3}$$

where *MD* is one third of the trace of the tensor. It normalizes the variance by the magnitude of the tensor as a whole. In other words, *FA* measures the fraction of the tensor that can be assigned to anisotropic diffusion. The *FA* index is appropriately normalized so that it takes values from zero (isotropic diffusion) to one (anisotropic diffusion).

There are many other ways to represent the anisotropy, such as:

$$sRA = \frac{\sqrt{(\lambda_1 - MD)^2 + (\lambda_2 - MD)^2 + (\lambda_3 - MD)^2}}{\sqrt{6} MD} \tag{5.4}$$

and

$$VF = 1 - VR = 1 - \frac{\lambda_1 \lambda_2 \lambda_3}{MD^3}, \tag{5.5}$$

where *sRA* stands for scaled relative anisotropy and *VF* for volume fraction. *RA* was transformed into *sRA* (multiplication by a constant) and *VF* was obtained by subtracting the volume ratio (*VR*) from 1, in order to scale the anisotropy indices from 0 to 1 [Kingsley, 2006].

Another DAI, not very used as an intravoxel measure, is the Lattice Index (*LI*). Although the *LI* was first introduced as an intervoxel measure [Pierpaoli and Basser, 1996], it can be computed for a single voxel by:

$$LI = \frac{FA + FA^2}{2}. \tag{5.6}$$

5.4 Intervoxel diffusion measures

The rotationally invariant properties mentioned in previous section are usually computed for a single voxel and therefore, can be interpreted as a intravoxel measure. Further interesting information can be obtained by looking at how the tensor parameters estimated in a given voxel compare with those in neighboring voxels. The simplest way to do this is to use measures that quantify the distance (or the difference) between two neighboring tensors. Another approach is to compute the differences (or coherences) within a neighborhood of a tensor and combine all the obtained quantities into a single measure, that can be interpreted as a homogeneity (or inhomogeneity) index.

5.4.1 Diffusion tensors distances

Distance between tensors can also be viewed as intervoxel measures. Given two tensors $\mathbf{T}_i$ and $\mathbf{T}_j$, the most simple comparison between two tensor quantities, used by Ziyan *et al.* [Ziyan et al., 2006], is the dot product between the principal eigenvector directions:

$$d_1(\mathbf{T}_i, \mathbf{T}_j) = |e_{1,i} \cdot e_{1,j}|, \tag{5.7}$$

where $e_{1,i}$ and $e_{1,j}$ are the principal eigenvectors of tensors $\mathbf{T}_i$ e $\mathbf{T}_j$, respectively. The absolute value of the dot product solves the problem with the sign ambiguity of the eigenvectors.

Another simple similarity measure, presented by Pierpaoli *et al.* [Pierpaoli and Basser, 1996] as an intervoxel anisotropy index, is the tensor dot product:

$$d_2(\mathbf{T}_i, \mathbf{T}_j) = \mathbf{T}_i : \mathbf{T}_j = \sum_{k=1}^{3}\sum_{l=1}^{3} \sqrt{\lambda_{k,i}}\sqrt{\lambda_{l,j}}(e_{k,i} \cdot e_{l,j})^2. \tag{5.8}$$

Alexander *et al.* [Alexander et al., 1999] proposed a number of tensor similarity measures. Their purpose was to match pairs of diffusion tensor images (DTI) and the proposed measures were based on the diffusion tensor itself and indices derived from the diffusion tensor. One of the similarity measures proposed by them was obtained negating the following Euclidean distance metric:

$$d_3(\mathbf{T}_i, \mathbf{T}_j) = \sqrt{\text{Trace}((\mathbf{T}_i - \mathbf{T}_j)^2)}. \tag{5.9}$$

This similarity metric was also explored in other DTI studies under different names, such as generalized tensor dot product [Jones et al., 1999] and Frobenius norm [Wiegell et al., 2003, Ziyan et al., 2006]. But because affine invariance is a desirable property for segmentation purposes and the Frobenius norm is not invariant to affine transformations, Wang and Vemuri [Wang and Vemuri, 2005] proposed a novel definition of diffusion tensor "distance", as the

square root of the J-divergence of the corresponding Gaussian distributions, i.e.,

$$d_4(\mathbf{T}_i, \mathbf{T}_j) = \frac{1}{2}\sqrt{\text{Trace}(\mathbf{T}_i^{-1}\mathbf{T}_j - \mathbf{T}_j^{-1}\mathbf{T}_i) - 2n}, \tag{5.10}$$

where n is the matrix size that represents the tensor. Eq. 5.10 is not a true distance since it violates the triangle inequality, but it is in fact a computationally efficient approximation of Rao's distance [Wang and Vemuri, 2005]. More recently, a new approach for calculating tensor similarity has been adopted in DTI studies: the Log-Euclidean distances. Among the similarities metrics proposed by Arsigny *et al.* [Arsigny et al., 2006], there is a metric very close related to the Frobenius norm, called the similarity-invariant Log-Euclidean distance, defined as :

$$d_5(\mathbf{T}_i, \mathbf{T}_j) = \sqrt{\text{Trace}((\log(\mathbf{T}_i) - \log(\mathbf{T}_j))^2)}. \tag{5.11}$$

Contrary to the classical Euclidean framework on tensors, one can see from Eq. 5.11 that symmetric matrices with null or negative eigenvalues are at an infinite distance from any tensor. To overcome this problem, in this paper we replace $\log(\mathbf{T}_i)$ by $\log(100 * \mathbf{T}_i + 1)$ to avoid the computation of the logarithm of null values.

Another affine invariant metric for statistical analysis and image processing of diffusion tensor data based on the Riemannian geometry was introduced independently by different authors [Batchelor et al., 2005, Pennec et al., 2006]:

$$d_6(\mathbf{T}_i, \mathbf{T}_j) = \sqrt{\text{Trace}(\log(D_{ij})^2)}, \tag{5.12}$$

where D_{ij} is equal to $\mathbf{T}_i^{-\frac{1}{2}}\mathbf{T}_j\mathbf{T}_i^{-\frac{1}{2}}$.

It is important to notice that the above intervoxel distance measures are not the only ones proposed in the literature, nevertheless they were chosen to be part of this study because they come from different approaches and privileges some aspects of tensors. A classification based on the nature of the derivation of the intervoxel measures was presented by Peeters *et al.* [Peeters et al., 2008]: measures based on scalar indices; measures that make use of the angles between eigenvectors; measures based on linear algebra; measures based on Riemannian geometry; measures considering the tensors as a representation of a probability density function and measures that combine different measures from the previous classes.

So, whereas the dot product is an angular difference, the tensor dot product and the Frobenius norm come from linear algebra, the Log-Euclidean distance and the affine-invariant Riemannian metric is based on Riemannian geometry and the J-divergence derives from statistical considerations.

5.4.2 Neighborhood anisotropy measures

Intervoxel anisotropy features were introduced by Pierpaoli and Basser [Pierpaoli and Basser, 1996] and extended by Skare et al. [Skare et al., 2000] to reduce the effect of noise. The principle is to perform spatial averaging of indices based on both eigenvalues and eigenvectors. One example of doing this is the lattice index (*LI*), already cited as an alternative intravoxel measure, although it was first presented as an intervoxel measure. *LI* measures how much the directions of the tensor eigenvectors differ between a given voxel and its neighbors. It is defined by:

$$LI = \frac{\sum a_N LI_N}{\sum a_N}, \tag{5.13}$$

where a_N is a weighting factor whose value is 1 for voxels that share a side with the reference voxel and $1/\sqrt{2}$ for voxels that share only a vertex with the reference voxel. LI_N is the basic element of the lattice index and is defined as:

$$LI_N = \sqrt{\frac{3}{8}}\frac{\sqrt{\boldsymbol{T}_i : \boldsymbol{T}_j}}{\sqrt{\mathbf{T}_i : \mathbf{T}_j}} + \frac{3}{4}\frac{\boldsymbol{T}_i : \boldsymbol{T}_j}{\sqrt{\mathbf{T}_i : \mathbf{T}_i}\sqrt{\mathbf{T}_j : \mathbf{T}_j}}, \tag{5.14}$$

where $\mathbf{T}_i : \mathbf{T}_j$ is called the "tensor dot product" between the reference diffusion tensor $\mathbf{T}_i$ and the neighboring diffusion tensor $\mathbf{T}_j$ (see Eq. 5.8) and $\boldsymbol{T}_i : \boldsymbol{T}_j$ is given by:

$$\boldsymbol{T}_i : \boldsymbol{T}_j = \mathbf{T}_i : \mathbf{T}_j - \frac{1}{3}\text{Trace}(\mathbf{T}_i)\text{Trace}(\mathbf{T}_j), \tag{5.15}$$

and can be seen as the tensor dot product between the anisotropic parts of the tensor[1]. A similar diffusion anisotropy index is the A_{dd}, defined as:

$$A_{dd} = \frac{\sum_1^8 a_N A_{dd}^N}{\sum a_N}, \tag{5.16}$$

where

$$A_{dd}^N = \frac{\boldsymbol{T}_i : \boldsymbol{T}_j}{\mathbf{T}_i : \mathbf{T}_j}. \tag{5.17}$$

Both *LI* and A_{dd} are weighted means of all adjacent neighbors, differing only by the definition of the basic element. Another index, first described by Klingberg et al [Klingberg et al., 1999], is the coherence index (*CI*). The *CI* in a voxel is the mean dot-product of the primary eigenvector of the reference voxel and the primary eigenvector of each one of its eight neighboring voxels. When

[1]Note that, it is important not to mix up $\mathbf{T}_i : \mathbf{T}_j$ with $\boldsymbol{T}_i : \boldsymbol{T}_j$, although notation is confusing

the eigenvectors are of unity length, the dot product is the cosine of the angle between the primary eigenvectors of both tensors and has a value between 0 and 1.

5.4.3 Gradients

Another class of intervoxel diffusion measures are the gradients based on mathematical morphology. The most common gradient based on mathematical morphology used in image processing is called the morphological gradient [Heijmans, 1994], that depends on the size and shape of the chosen structuring element. Using a flat structuring element at each point the morphological gradient (MG) yells the difference between the maximum and the minimum values over the neighborhood at the point determined by the flat structuring element:

$$\nabla_B^I(f) = \bigvee_{y \in B_x} \mathbf{I}_y - \bigwedge_{y \in B_x} \mathbf{I}_y, \tag{5.18}$$

where ∇_B^I is the morphological gradient. $B \subset E$ is a structured element centered at the origin of E and $\mathbf{I}_y$ is the intensity value in y (y is in the neighborhood of x, defined by B_x).

Because the diffusion tensor image does not have a single intensity value to be considered, the proposed solution is to compute the morphological gradient of any intravoxel measure presented in Section 5.3. As an example, by taking the fractional anisotropy FA_y as the $\mathbf{I}_y$, it is possible to compute the morphological gradient of the fractional anisotropy (MGFA):

$$\nabla_B^{FA}(f) = \bigvee_{y \in B_x} FA_y - \bigwedge_{y \in B_x} FA_y, \tag{5.19}$$

Another intervoxel diffusion gradient is the tensorial morphological gradient (TMG). It was first applied to segment tensorial images representing color images [Rittner et al., 2007] and then, its concept was extended and applied to synthetic diffusion tensor images [Rittner and Lotufo, 2008]. It is based on mathematical morphology and intervoxel distances between neighboring tensors.

While the classical morphological gradient at each point of a scalar image yields the difference between the maximum and the minimum values over the neighborhood at the point determined by a structuring element, the tensorial morphological gradient (TMG) of a tensorial image is defined by:

$$\nabla_B^T(f)(x) = \bigvee_{y,z \in B_x} d_n(\mathbf{T}_y, \mathbf{T}_z), \tag{5.20}$$

$\forall x \in E$, where d_n represents any of the intervoxel distances presented in Subsection 5.4.1, $B \subset E$ is a structuring element centered at the origin of E, $\mathbf{T}_y$ is the tensor that represents the diffusion in y, and $\mathbf{T}_z$ is the tensor that represents the diffusion in z (y and z are in the neighborhood of x, defined by B_x). ∇_B^T is the proposed TMG. Because the intervoxel measures are already comparisons between

neighbors, the proposed gradient is not the difference between the maximum and the minimum values, but only the maximum value.

Likewise the TMG, all neighborhood intervoxel measures presented in Subsection 5.4.2 (*LI*, A_{dd} and *CI*) result from comparison between tensors belonging to a neighborhood using intervoxel measures. The main difference between them and the TMG is that the TMG takes the maximum between the computed intervoxel measurements while the *LI*, the A_{dd} and the *CI* take the average of the measurements (weighted or not by the distance of each neighbor).

So, it is possible to extend the definition of the TMG to the Lattice Index (*LI*), for example, defining a new index, called morphological lattice index (*MLI*):

$$MLI = \bigvee_{y,z \in B_x} LI_N(\mathbf{T}_y, \mathbf{T}_z). \tag{5.21}$$

The same extension is valid to A_{dd}, resulting in:

$$MA_{dd} = \bigvee_{y,z \in B_x} A_{dd}(\mathbf{T}_y, \mathbf{T}_z). \tag{5.22}$$

By using the same reasoning, it is easy to conclude that the extension of the Coherence Index (*CI*), originally computed as the mean value of the dot product within a defined neighborhood, is the TMG based on the dot product (d_1). Furthermore, whereas the neighboring in the *CI* computation is fixed as a square around the voxel (8 neighbors), the neighborhood in the DP-TMG computation is defined by the structuring element and can be chosen accordingly to the application.

Table 5.1 and Table 5.2 summarize all presented intravoxel and intervoxel measures. Table 5.1 list the voxelwise measures and points out whether the intravoxel and intervoxel measures are rotationally invariant or not, based on the eigenvalues and/or based on the eigenvectors. Table 5.2 lists each neighborhood measure and identify which measure it is based on, and whether it is an average of the measure within a neighborhood ($mean$), the biggest difference between neighbors ($max - min$) or it is the maximum measure found in the neighborhood (max). It is valuable to note that the measures listed in the last two columns (MG and TMG) are the ones based on mathematical morphology and being proposed in this paper.

5.5 Methods

5.5.1 Synthetic data

In order to analyze the previously mentioned scalar maps synthetic grids were used. First, plots were generated, where the x-axis corresponds to λ_1 and the y-axis to λ_2 ($\lambda_1 \geq \lambda_2$). The third

Tab. 5.1: Summary of voxelwise measures

	Measure	Rot.Inv.	Eigenvalues	Eigenvectors
Intravoxel	*MD*	yes	yes	no
	FA	yes	yes	no
	VF	yes	yes	no
	sRA	yes	yes	no
	LI	yes	yes	no
Intervoxel	DP	yes	no	yes
	TDP	yes	yes	yes
	FN	no	yes	yes
	Jdiv	yes	yes	yes
	Riem	yes	yes	yes
	LogE	no	yes	yes
	A_{dd}^N	yes	yes	yes
	LI_N	yes	yes	yes

Tab. 5.2: Summary of neighboring measures

	Meas.	*LI*	A_{dd}	*CI*	MG[a]	TMG[a]
Intravoxel	*MD*				max-min	
	FA				max-min	
	VF				max-min	
	sRA				max-min	
	LI				max-min	
Intervoxel	DP			mean		max
	TDP					max
	FN					max
	Jdiv					max
	Riem					max
	LogE					max
	A_{dd}^N		mean			max
	LI_N	mean				max

[a]Proposed by the authors

eigenvalue (λ_3) was set to 0. The color (gray-level) corresponds to the measure computed for the tensor with eigenvalues equal to λ_1, λ_2 and λ_3.

The second kind of plot were generated to illustrate the distinct nature of some of the existing intervoxel measures, regarding to diffusion tensors comparison. Each grid consisted of a bi-dimensional matrix M, where each position M_{ij} contained the dissimilarity value between tensor T_i and tensor T_j, computed using one of the four intervoxel measure: Dot Product (DP), Tensor Dot Product (TDP), Frobenius Norm (FN) and J-divergence (J-div). For each measure, three tensors groups were analyzed: tensors with fixed trace and orientation and varying *FA*, tensors with fixed orientation and *FA* and varying trace, and finally tensors with fixed trace and *FA* and varying orientation.

5.5.2 Data acquisition

The diffusion data used in our segmentation experiment were acquired on a Siemens 3T Trio MR scanner with $N = 30$ diffusion encoding directions with 63 slices, 2.0 mm $\times 2.0$ mm $\times 2.0$ mm, TE $= 95$ ms, TR $= 8.7$ s and $b = 1000$s/mm^2. The diffusion data was first linearly interpolated before tensor estimation.

5.5.3 Scalar maps visualization

The data were first cropped around the corpus callosum. Intravoxel and intervoxel maps were computed and visualized. All morphological gradients were computed using a 3×3 diamond structuring element and the measures based on the average used the 8 neighbors contained in a square around the reference tensor.

5.5.4 Segmentation experiments

After computation of the scalar maps, the hierarchical segmentation was achieved by the application of the watershed from markers [Beucher and Meyer, 1992, Vincent and Soille, 1991, Falcão et al., 2004, Cousty et al., 2009] and extinction values computation [Vachier and Meyer, 1995, Grimaud, 1992, Najman and Schmitt, 1996, Meyer, 1996]. In other words, after calculating the scalar map of the original image, the n structures in the image which has the greatest volume extinction values were automatically selected. The n markers assigned to these regions were then used in the watershed transform, which segmented the scalar map in n regions [Rittner and Lotufo, 2009].

In the first segmentation experiment, the corpus callosum was segmented from the original

diffusion image using the scalar maps computed in previous section. The second experiment was done using the same set of diffusion images, this time cropped around the thalamus. All processing was done in a 3D image, but only a slice is presented, to make it more comprehensible.

To confirm our segmentation result, we segmented the thalamus of the same subject using the ANIMAL+INSECT [Collins et al., 1999], an algorithm for improved automatic segmentation of gross anatomical structures of the human brain. It merges the output of a tissue classification process (INSECT) with gross anatomical region masks, automatically defined by non-linear registration of a given data set with a probabilistic anatomical atlas (ANIMAL). Instead of using diffusion images to perform the segmentation, it combines information from T1, T2 and PD images to accomplish the task.

5.6 Results

5.6.1 Synthetic data

Fig. 5.1 shows the behavior of the intravoxel scalar maps: *MD*, *FA*, *VF*, *sRA* and *LI*. All measures are rotationally invariant. Although the four anisotropy index showed in Fig. 5.1(b)–(e) present slightly different behavior, all of them quantify the anisotropy degree of a tensor, varying from 0 ($\lambda_1 = \lambda_2 = \lambda_3$) to 1 ($\lambda_1 = 1$, $\lambda_2 = \lambda_3 = 0$). However, *sRA* appears to have some advantage in that for cylindrical symmetry, its value is a linear function of the largest eigenvalue, whereas *FA* is concave down and *VF* has a sigmoid shape.

(a) *MD* (b) *FA* (c) *VF* (d) *sRA* (e) *LI*

Fig. 5.1: Diffusion anisotropy index computed for a synthetic DT, where λ_1 and λ_2 are gradually increased and λ_3 is constant ($\lambda_1 \geq \lambda_2$).

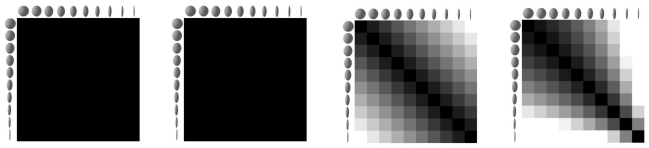

(a) DP (b) TDP (c) FN (d) Jdiv

Fig. 5.2: Computed distance between tensors with varying fractional anisotropy (orientation and trace constant) using four different intravoxel measures

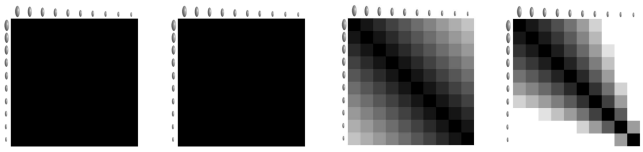

(a) DP (b) TDP (c) FN (d) Jdiv

Fig. 5.3: Computed distance between tensors with varying trace (orientation and fractional anisotropy constant) using four different intravoxel measures

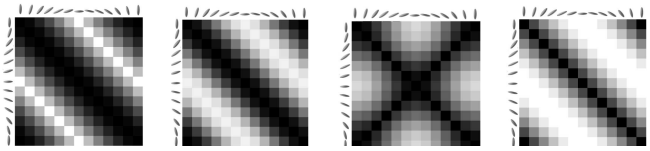

(a) DP (b) TDP (c) FN (d) Jdiv

Fig. 5.4: Computed distance between tensors with varying orientation (trace and fractional anisotropy constant) using four different intravoxel measures

Fig. 5.2, Fig. 5.3 and Fig. 5.4 depict the obtained dissimilarities when comparing tensors using the four different similarity measures: dot product (DP), tensorial dot product (TDP), Frobenius norm (FN) and J-divergence (Jdiv).

Fig. 5.2 shows dissimilarities computed for tensors with fixed trace and orientation and variable *FA* using all four similarity measures. Fig. 5.2(a), for example, shows dissimilarities between tensors computed using the DP. From left to right, tensors present same orientation and trace. The only changing parameter is the *FA*. The same tensor represented in the first column is represented also in the first line, the tensor in the second column is the same of the second line, and so on. So, each square of Fig. 5.2(a) contains the dissimilarity value between the tensor represented in that column and the tensor in that line, computed using the DP as intravoxel measure. The computed dissimilarities are represented using a gray scale, where black represents the minimum and white represents the maximum dissimilarity.

Fig. 5.2(b)–(d) were obtained exactly the same way as Fig. 5.2(a), the only difference is the measure used to compute the dissimilarity. Fig. 5.2(b) used the TDP, Fig. 5.2(c) used the FN and Fig. 5.2(d) used the Jdiv.

Exactly the same concept was used to build Fig. 5.3. It shows dissimilarities computed for tensors with fixed *FA* and orientation and variable trace using all four similarity measures. Fig. 5.3(a)–(d) shows dissimilarities between tensors computed using respectively the DP, the TDP, the FN and the Jdiv. Finally Fig. 5.4 shows dissimilarities computed for tensors with fixed trace and *FA* and variable orientation using all four intravoxel measures. Fig. 5.4(a) shows distances between tensors computed

using the DP, Fig. 5.4(b) used the TDP, Fig. 5.4(c) used the FN and Fig. 5.4(d) used the Jdiv.

5.6.2 Scalar maps visualization

Fig. 5.5 presents an example of a DT image and the intravoxel and intervoxel measures computed for it. Fig. 5.5(a) depicts the original image: a DT image of the brain cropped around the corpus callosum. Although the cropped image is a $91 \times 40 \times 66$, only one slice is presented, in order to facilitate visualization. Fig. 5.5(b)–(d) show the eigenvalues from the DTI (λ_1, λ_2 and λ_3, respectively) and Fig. 5.5(e), the principal eigenvector direction (color-coded map).

First row of Fig. 5.6 depicts the intravoxel measures computed for Fig. 5.5(a). The intervoxel measures based on the morphological gradient ($max - min$) of intravoxel measures are presented in the second row of Fig. 5.6. Fig. 5.7(a)–(h) show the tensorial morphological gradients, based on intervoxel measures (Jdiv, TDP, FN, Riem, LogE, DP, A_{dd}^N and LI_N). Finally Fig.5.8(a)–(c) present neighborhood anisotropy measures based on average: *CI*, A_{dd} and *LI*, respectively.

(a) DTI (b) $\lambda 1$ (c) $\lambda 2$ (d) $\lambda 3$ (e) PED

Fig. 5.5: Corpus Callosum: the diffusion tensors represented by ellipsoids, each eigenvalue (λ_1, λ_2 and λ_3) shown separately and the principal eigenvector direction (e_1). Small λ_2 and λ_3 and uniform color of e_1 confirm that the corpus callosum is a highly oriented structure.

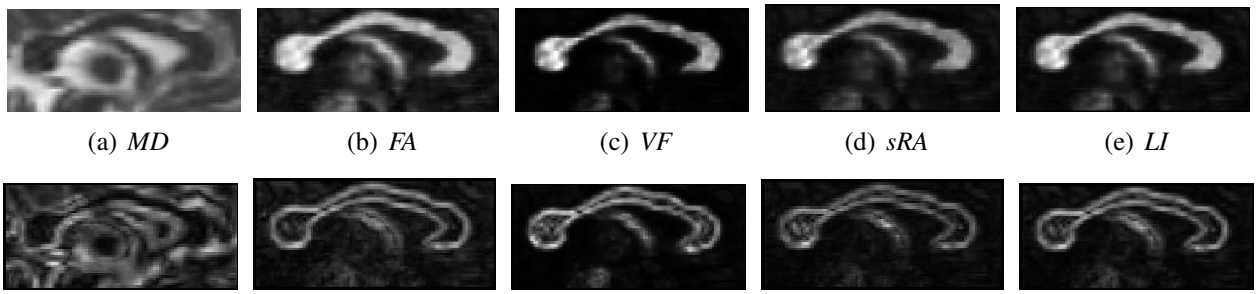

(a) *MD* (b) *FA* (c) *VF* (d) *sRA* (e) *LI*

(f) MG-*MD* (g) MG-*FA* (h) MG-*VF* (i) MG-*sRA* (j) MG-*LI*

Fig. 5.6: Intravoxel measures: *MD*, *FA*, *VF*, *sRA* and *LI* and respective morphological gradient(MG). The MGs were computed using a 6-connected neighborhood as structuring element.

Fig. 5.9(a) the same original image from Fig. 5.5(a), with a detail selected on it. The scalar maps computed for the selected detail can be seen in Fig. 5.9(b)–(d), while Fig. 5.9(e)–(g) depict the DP computed between each voxel of the image and its neighbor in each direction (right-left,

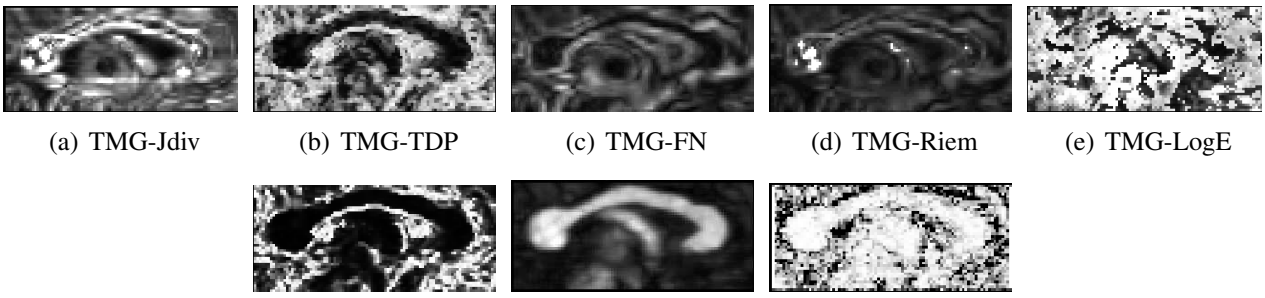

(a) TMG-Jdiv (b) TMG-TDP (c) TMG-FN (d) TMG-Riem (e) TMG-LogE

(f) TMG-DP (g) TMG-A_{dd} (max) (h) TMG-LI_n (max)

Fig. 5.7: TMGs computed using each intervoxel measure presented in Sec.5.4.

(a) CI (b) A_{dd} (mean) (c) LI_n (mean)

Fig. 5.8: Neighborhood anisotropy measures computed for the corpus callosum.

anterior-posterior and superior-inferior). Fig. 5.10 contains the *CI* for the same detail, computed using two distinct neighborhood.

5.6.3 Segmentation experiments

Fig. 5.11 shows segmentation results based on measures from different groups. Fig. 5.11(a) presents the intravoxel measure *FA* and Fig. 5.11(d) the respective segmentation result. It was obtained by applying a simple thresholding on the *FA*. Fig. 5.11(b) and Fig. 5.11(e) depicts the MG-*FA* and the segmentation result obtained from the watershed transform. And in Fig. 5.11(c) and Fig. 5.11(f) are the TMG based on the Frobenius Norm and the resulting watershed segmentation.

As opposed to the corpus callosum, the thalamus has neither a high anisotropy, nor a high diffusivity, making the DTI-based segmentation task harder. The distinct diffusion characteristics of both brain structures can be seen in Fig. 5.12(a) and Fig. 5.12(b). To validate our segmentation result, we segmented the thalamus of the same subject using the ANIMAL+INSECT. The line in red in the first, third and fourth rows of Fig. 5.13 is the segmentation result obtained with the ANIMAL algorithm.

The first row of Fig. 5.13 contains the intravoxel measures of the thalamus. Fig. 5.13(f)–(j) were obtained by applying a threshold in the scalar measures, Fig. 5.13(k)–(o) contain the MG of each scalar map from the first row and finally Fig. 5.13(f)–(j) depict segmentation labels resulting from the watershed over the MGs from third row.

Fig. 5.14 presents another segmentation experiment for the thalamus. Fig. 5.14(a) presents one

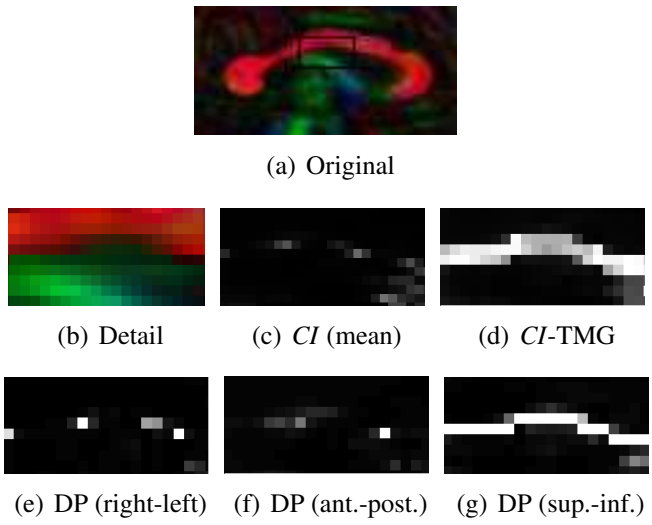

(a) Original

(b) Detail (c) *CI* (mean) (d) *CI*-TMG

(e) DP (right-left) (f) DP (ant.-post.) (g) DP (sup.-inf.)

Fig. 5.9: Comparison of the coherence index (*CI*) computed by mean and computed using the TMG. Only a detail of the original image is shown. The dot product (DP) was computed separately for neighbors in each direction (right-left, anterior-posterior, superior-inferior).

(a) 8 neighbors (2D) (b) 6 neighbors (3D)

Fig. 5.10: Comparison of the coherence index (*CI*) computed using different neighborhood: 8-connected structuring element (2D) and 6-connected structuring element (3D).

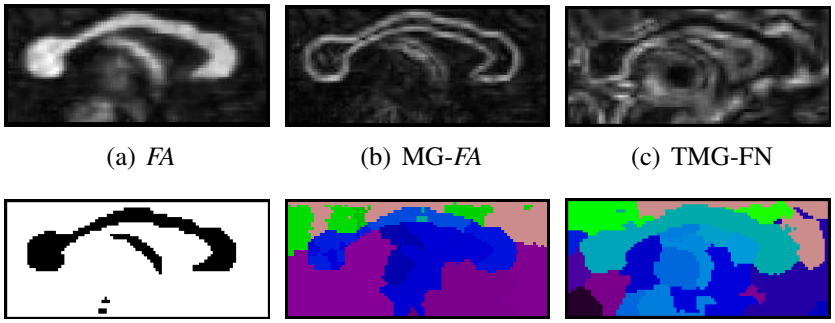

(a) *FA* (b) MG-*FA* (c) TMG-FN

(d) *FA* + Threshold (e) MG-*FA* + WS (f) TMG-FN + WS

Fig. 5.11: Segmentation of Corpus Callosum using different measures and different segmentation techniques: Threshold over the *FA*; Watershed over the morphological gradient of *FA*; Watershed over the tensorial morphological gradient computed using the Frobenius Norm.

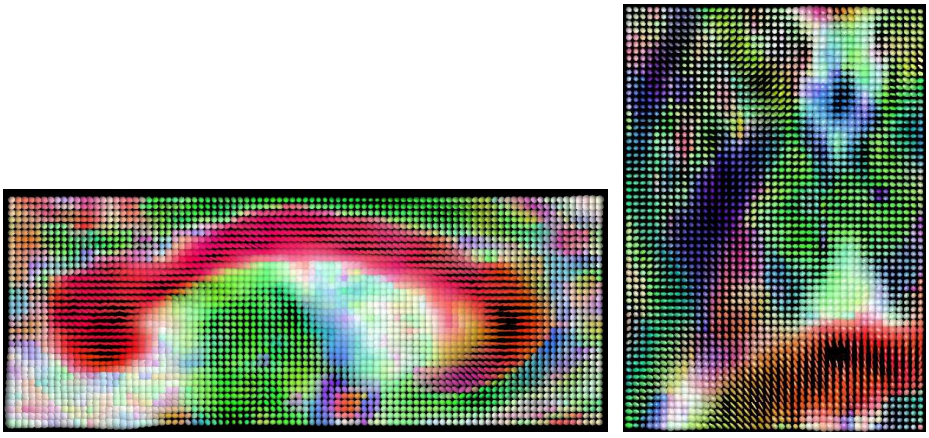

(a) DTI (b) DTI

Fig. 5.12: One slice of the diffusion tensor field in the region of the corpus callosum and of the thalamus.

slice of the original DTI, Fig. 5.14(b) and Fig. 5.14(c) contains the computed *FA* and TMG-FN, respectively. The second row of Fig. 5.14 depicts segmentation results performed by distinct methods: Fig. 5.14(d) shows the ANIMAL segmentation, Fig. 5.14(e) was obtained from watershed applied to MG-*FA* and Fig. 5.14(f) resulted from watershed on TMG-FN. The same results can be visualized in 3D in Fig. 5.14(g)–(i). Fig. 5.15 show the same segmentation results from Fig. 5.14, but overlaid to ANIMAL segmentation, in order to facilitate comparisons.

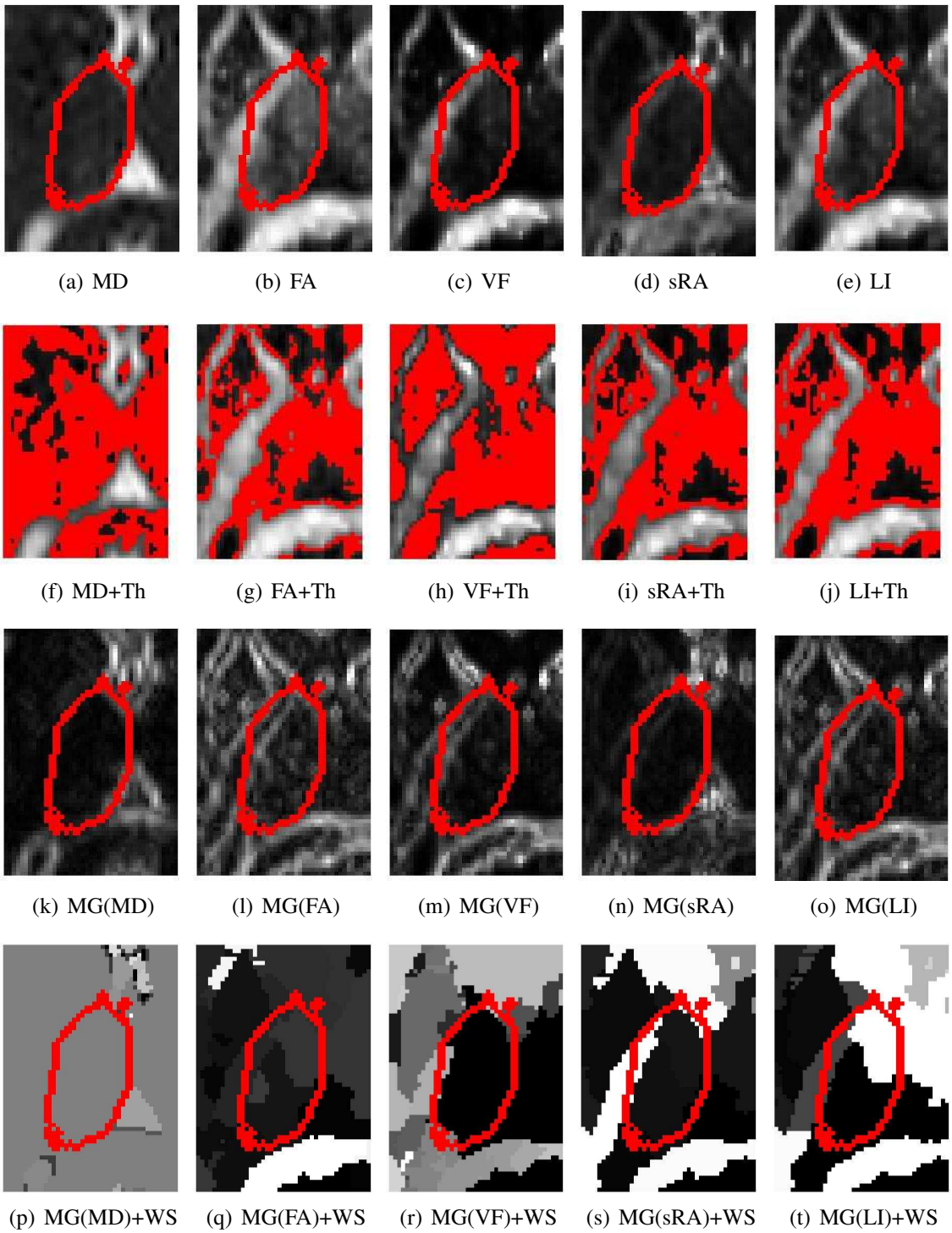

(a) MD (b) FA (c) VF (d) sRA (e) LI

(f) MD+Th (g) FA+Th (h) VF+Th (i) sRA+Th (j) LI+Th

(k) MG(MD) (l) MG(FA) (m) MG(VF) (n) MG(sRA) (o) MG(LI)

(p) MG(MD)+WS (q) MG(FA)+WS (r) MG(VF)+WS (s) MG(sRA)+WS (t) MG(LI)+WS

Fig. 5.13: Segmentation experiments of the thalamus based on intravoxel measures and morphological gradients. Thresholds over the intravoxel measures were not able to segment the thalamus. Not even the morphological gradient of intravoxel measures were able to preserve borders and allow segmentation by the watershed.

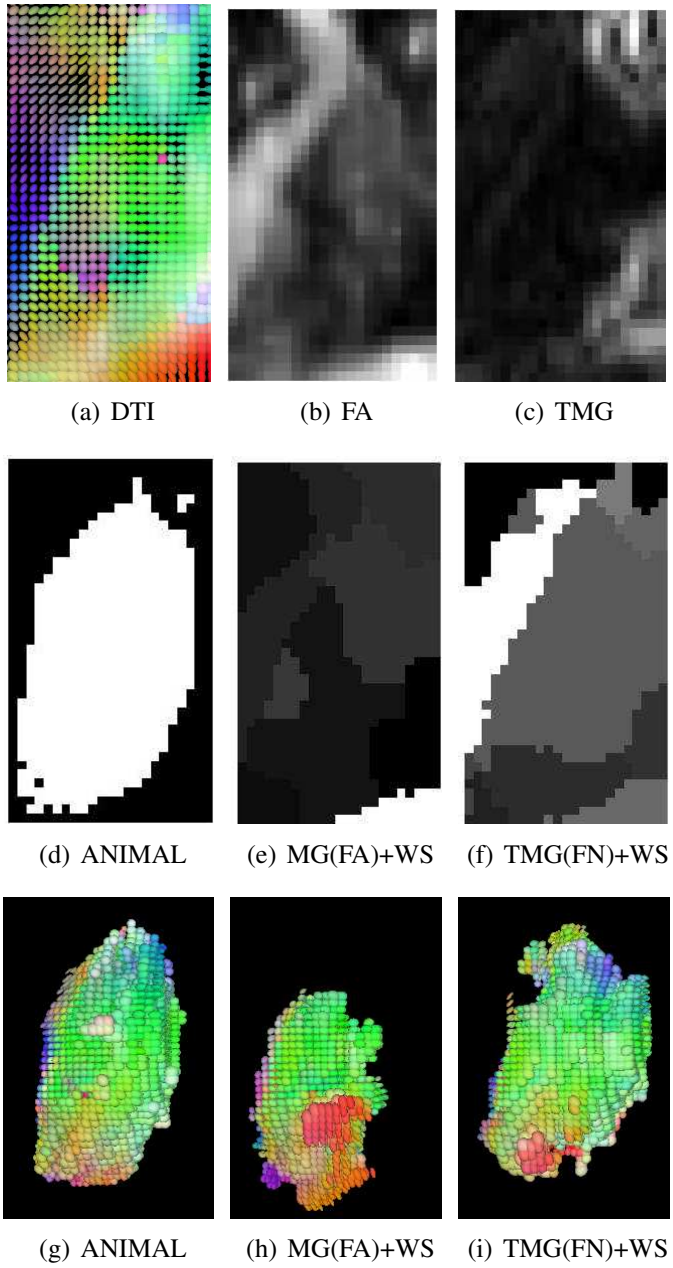

(a) DTI (b) FA (c) TMG

(d) ANIMAL (e) MG(FA)+WS (f) TMG(FN)+WS

(g) ANIMAL (h) MG(FA)+WS (i) TMG(FN)+WS

Fig. 5.14: Watershed segmentation based on distinct scalar maps: morphological gradient of *FA* and tensorial morphological gradient based on FN. Comparison of obtained result with segmentation using ANIMAL. Segmentation based on the TMG-FN map is more similar to segmentation obtained by ANIMAL.

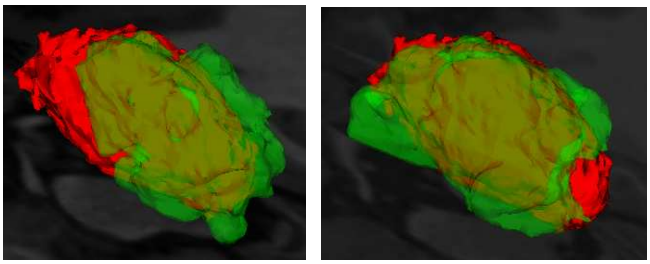

(a) MG(*FA*)+WS (b) TMG(FN)+WS

Fig. 5.15: Results obtained by watershed (green) overlaid to ANIMAL segmentation (red), confirming the superiority of the TMG-FN over the MG-FA.

5.7 Discussion

From Fig. 5.1 of the intravoxel measures, it is possible to infer that *FA* (Fig. 5.1(b)) maps diffusion anisotropy with greatest detail and has the highest sensitivity in the low anisotropy range. Fig. 5.1(c) shows that *VF* has decreased resolution in anisotropic regions and *sRA* and LI have an intermediate sensitivity in the low anisotropy range but worst in the high anisotropy range (Fig. 5.1(d)–(e)). Results reported by Papadakis *et al.* [Papadakis et al., 1999] and Skare *et al.* [Skare et al., 2000] support such notions.

In the example of Fig. 5.6 it is possible to confirm that transitions between low and high anisotropic regions are smooth in FA map (Fig. 5.6(b)) and more abrupt in VF map (Fig. 5.6(c)), due to its lack of sensitivity in less anisotropic regions. The corpus callosum, therefore, seems bigger in the FA map than in the VF map and would result in different segmentations. In the other hand, the MG-FA from Fig. 5.6(g) is much more noisy outside the corpus callosum than the MG-VF from Fig. 5.6(h), and the segmentation result could suffer distortions due to this noise. Also in regions of intermediate anisotropy, such as the thalamus, the FA map presented in Fig.5.13(b) is much more useful in border enhancement than the VF map in Fig.5.13(c).

Among the intervoxel measures, conclusions extracted from Fig.5.2–5.4 are confirmed by Fig.5.7. At first glance, conclusion from Fig. 5.2 and Fig. 5.3 is that the DP and the TDP are not suitable for tensors comparison purposes. Because both are measures that take into account only changes in tensors orientation, the dissimilarity computed between completely different tensors, concerning *FA* or trace is null. That is, distinct tensors pointing to the same direction are equal, if compared using the DP or the TDP. That is why Fig. 5.2(a)–(b), Fig. 5.3(a)–(b) are null images (completely black). Conversely, in comparisons where the only change is in tensors orientation, both measures are able to identify the dissimilarities. Fig. 5.4(a)–(b) depict the computed dissimilarities and confirm what was expected: the maximum computed dissimilarity is between tensors pointing to perpendicular directions.

Furthermore, Fig. 5.2 and Fig. 5.3 show that the Frobenius Norm and the J-divergence are both capable of measuring tensor dissimilarities, when tensors present small differences only in trace or in *FA*. But, while the dissimilarities computed using the Frobenius norm have a linear behavior (Fig. 5.2(c) and Fig. 5.3(c)), the ones computed by the J-divergence present a exponential characteristic, originated by its logarithmic nature(Fig. 5.2(d) and Fig. 5.3(d)).

Finally, when observing Fig. 5.4 is possible to identify the distinct behavior of the Frobenius norm, in comparison to all other measures tested, derived from the fact that it is not an affine invariant measure. While in Fig. 5.4(a),(b) and (d) tensors aligned to cartesian axes are similar only to tensors pointing in same direction (angular distance = 0 or π), in Fig. 5.4(c), tensors not aligned to cartesian axes are similar not only to tensors pointing in same direction (angular distance = 0 or π), but also in opposite direction (angular distance = $\pi/2$ or $3\pi/2$).

By using the same intravoxel measures in TMG computation, conclusions are slightly different. The DP and the TDP, not able to detect differences between distinct tensors with same orientation, were able to preserve important borders, as shown in Fig.5.7(f) and Fig.5.7(b) in the corpus callosum experiment. The Frobenius Norm, not affine invariant, also provided a useful scalar map (Fig.5.7(c)), when used to compute the TMG.

In a recent study, Peeters *et al.* [Peeters et al., 2008] classified and summarize the different intervoxel measures that have been presented in diffusion tensor literature, and also presented a framework to analyze and compare the behavior of the measures according to several selected properties (size, shape, orientation, robustness and metric). The measures behavior were illustrated through several plots and required carefully interpretation. Results obtained here are consistent with conclusions from Peeters *et al.* [Peeters et al., 2008]. According to them, the Frobenius Norm proved to be the most robust measure, and it states that although the FN measure is relatively simple, it showed good behavior. They show also that, when using measures like the Jdiv, the LogE and the Riem, one has to be careful with the sensitivity to small shape and size changes close to the degenerate cases.

Since the corpus callosum has a mean diffusivity and an anisotropy very distinct from the neighboring structures, all morphological gradients (MGs) computed based on the intervoxel DAIs preserved the borders. Simple segmentation techniques based on any of the computed MGs would probably be able to segment the corpus callosum.

Comparing the TMGs with the DAIs and with the MGs, is evident that the TMGs are richer in details, since they take into account much more information. The DAIs are the most simple measures, taking into account only the eigenvalues of each voxel. The MGs are an extension of the DAIs, considering the measure, not only in the voxel, but also in the neighbors. The neighborhood is also included in the computation of the TMGs, but while the MGs are based on intravoxel measures,

i.e.,consider only the eigenvalues, the TMGs are based on intervoxel measures, therefore include information from the eigenvectors.

The gradients based on Jdiv (Fig. 5.7(a)), the LogE (Fig. 5.7(e)) and the Riem (Fig. 5.7(d)) presented smoother borders, therefore it is expected that the segmentation result provided by them will not be good. The borders in the TMG using the TDP (Fig. 5.7(b)), the FN (Fig. 5.7(c)), the DP (Fig. 5.7(f)), the A_{dd} (Fig. 5.7(g)) and the LI_N (Fig. 5.7(h)) were sharper and should provide better results in the application of watershed technique.

The neighboring intervoxel measures presented in Fig.5.8(a)–(c) seem able to preserve the borders of corpus callosum, specially the A_{dd}. But their counterpart presented in last row of Fig. 5.7 accomplish the task with superiority, thanks not only to the replacement of the mean by the maximum (see Eq. 5.14 and Eq. 5.21, for example), but also due to the neighborhood being considered in their computation.

Take the case of Fig. 5.8(a) (*CI*) and Fig. 5.7(f) (*CI*-TMG). As expected, the *CI* looks like an attenuation of *CI*-TMG, preserving almost all the borders of the corpus callosum. While Fig. 5.9(d) confirm that border from corpus callosum was detected by the *CI*-TMG, in Fig. 5.9(c) the same edge was not recognized by *CI*. The main reason for this can be understood by observing Fig. 5.9(e)–(g). Whereas the DP computed in the right-left and the anterior-posterior directions are very low (very directionally coherent), the DP in the superior-inferior direction is the only one presenting high values in the border of corpus callosum. Because the *CI* is computed using information only from the 8 neighbors of the axial plane, the superior-inferior angular difference detected in Fig. 5.9(g) was not even considered, as opposed to the *CI*-TMG, that used in the example a 6-connected structuring element (3D).

By choosing another plane to use in the *CI* computation (sagittal or coronal), the mentioned border from corpus callosum would be probably detected, in detriment to other borders. A better solution would be to use a 3D neighborhood. Fig. 5.10 shows that the result of the *CI* could be considerably improved by changing from 8-connected neighbors (2D) to 6-connected neighbors (3D). Similar conclusions can be drawn about *LI* and A_{dd}, since the neighbors used in their computation are also from a single plane.

While the first segmentation experiment showed that the segmentation of the corpus callosum is possible using almost any combination of measures and segmentation techniques, by observing each DAI of Fig.5.13 is possible to notice the absence of strong borders, specially in the medial and posterior part of the thalamus. Therefore, a simple thresholding of the intravoxel measures is not able to correctly segment it, as depict in Fig. 5.13(f)– (j). Even the morphological gradients of intravoxel measures presented in Fig. 5.13(k)– (o) were not able to detect the borders of the thalamus. That explains why none of the watershed segmentation results based on these MGs and presented in the

last row of Fig. 5.13 was close to the result from the ANIMAL segmentation.

Fig. 5.14(b) shows that the anisotropy does not change significantly inside and outside the thalamus. Nevertheless, the TMG based on the Frobenius Norm, presented in Fig. 5.14(c), was able to delineate the thalamus, since its computation considers the eigenvalues and the eigenvectors of the tensors and their neighbors.

5.8 Conclusions

In this work, tensor-derived maps, usually used in quantitative analysis of DTI, were studied in a segmentation perspective. Existing intravoxel and intervoxel maps were discussed, and new scalar maps were explored, based on concepts of mathematical morphology. While a simple thresholding applied to the *FA* map is able to segment the corpus callosum, only scalar maps that take into account not only the eigenvalues, but also the eigenvectors were able to preserve the information necessary to successfully perform the segmentation of the thalamus. Furthermore, with no information from the neighbors, segmentation of the thalamus was not possible. Segmentation results obtained by the watershed applied to the FN-TMG were comparable to atlas-based segmentation.

Capítulo 6

Segmentação de núcleos do tálamo

O artigo a seguir, intitulado "Segmentation of thalamic nuclei based on tensorial morphological gradient of diffusion tensor fields" e submetido ao *International Symposium on Biomedical Imaging - ISBI'10*, apresenta os primeiros resultados obtidos a partir da aplicação do método de segmentação de imagens de tensores de difusão baseado em morfologia matemática, descrito nos capítulos anteriores no problema de segmentação dos núcleos do tálamo. A segmentação dos núcleos do tálamo tem aplicação direta no planejamento cirúrgico e no estudo de doenças neuro-degenerativas e só passou a ser possível *in vivo* depois do surgimento da DTI. Até então, a divisão do tálamo em núcleos só era feita *post-mortem*.

6.1 Abstract

Although thalamic nuclei are not directly visible on conventional anatomical magnetic resonance images (MRI), it is possible to observe differences between the nuclei using diffusion tensor imaging (DTI), because of their distinct fiber orientation. This work presents a method to segment the various nuclei of human thalamus using diffusion MRI. Our approach is to use the watershed transform and other concepts from mathematical morphology to segment the nuclei. However, to segment structures using the tensor data produced with DTI (as opposed to scalar images) the concept of a tensorial morphological gradient (TMG) needs to be introduced. Based on the TMG, segmentation of the nuclei of the thalamus was successful using the watershed transform. Our segmentation is consistent with a histological atlas. Since the proposed method, as opposed to the majority of the DTI-based segmentation methods, does not require manual seed and/or surface placement, its results are highly repeatable.

6.2 Introduction

The thalamus is a subcortical structure that processes and relays sensory information selectively to various regions of the cerebral cortex. These relay neurons are clustered into nuclei based on histological or functional criteria, and delineation of the nuclei is important for surgical treatment of various movement disorders and for localization of functional brain activation to specific nuclei.

The thalamic nuclei have traditionally been delineated histologically by their distinct cyto- and myeloarchitecture [Morel et al., 1997]. Recently, it has been shown that the thalamic nuclei can be differentiated using diffusion tensor imaging (DTI), a new modality of magnetic resonance imaging able to quantify the anisotropic diffusion of water molecules in highly structured biological tissues. In diffusion tensor images, the thalamus shows distinct clusters of different diffusion displacement distribution, that correspond in anatomic location and fiber orientation to the thalamic nuclei. The diffusion displacement distribution, as described in DTI by the diffusion tensor, thus provides a new criterion for distinguishing thalamic nuclei. Although DTI can resolve thalamic nuclei, a segmentation algorithm is required to explicitly delineate the boundaries of the individual nuclei.

Several methods have been proposed to segment the thalamic nuclei based on diffusion MRI. Behrens *et al.* [Behrens et al., 2003] mapped the connections between each voxel of the thalamus and the cortex using a tractography-based method. A subsequent paper [Johansen-Berg et al., 2005] confirmed that the obtained clusters correspond to individual thalamic nuclei. Wiegell *et al.* [Wiegell et al., 2003] did not use connectivity properties, but presented a modified k-means clustering algorithm, that finds voxels which are close in position and similar in diffusion properties. Ziyan *et al.* [Ziyan et al., 2006] also used local diffusion properties and described an approach for segmentation of thalamic nuclei using a spectral graph partitioning algorithm. Duan *et al.* [Duan et al., 2007] proposed a nuclei segmentation algorithm based on the mean-shift technique. The segmentation of thalamic nuclei presented by Jonasson *et al.* [Jonasson et al., 2007] was done by propagating a set of coupled level-sets through a region-based force.

The algorithms listed above require previous knowledge of the structures to be segmented and depend on seed placement, initial surface delineation and/or parameter adjustments, making the segmentation process very susceptible to initialization. In order to reduce the influence of user choices, this work proposes a segmentation algorithm based on the watershed transform. The watershed transform can be classified as a region-based segmentation approach and has been successfully applied to the solution of many medical imaging problems, such as the segmentation of blood cells [Falcão et al., 2001], neuromorphometry [Falcão et al., 2002] and characterization of human cortex [Rettmann et al., 2002, Castellano et al., 2003].

A crucial step of the watershed-based segmentation is the computation of a gradient of the image to be segmented. Since the goal here is to segment tensorial images and not scalar ones, the classical

morphological gradient can not be computed. Therefore, a tensorial gradient has to be defined. In previous work [Rittner and Lotufo, 2008], a tensorial morphological gradient (TMG) was presented as a technique to transform the diffusion tensor image into a scalar map with meaningful values at edges of structures whose segmentation is desired. The TMG uses diffusion intervoxel measures and combines them to compute a gradient using concepts from mathematical morphology.

Once the TMG map is computed, its segmentation is done by the watershed transform. The over-segmentation usually resulting from the classical watershed transform is avoided by the application of the hierarchical watershed, where only the most significant regions of the image are delineated. The only parameter to be chosen is the number of regions into which the image should be segmented. While Section 6.3 describes the segmentation method, results are presented in Section 6.4. Finally, Section 6.5 discusses results and concludes the paper.

6.3 Methods

6.3.1 Data acquisition

The data used in our experiment were acquired on a Siemens 3T Trio MR scanner using an 8-channel phased array head coil. The following data were acquired in one healthy volunteer: diffusion images with $N = 30$ diffusion encoding directions with $b = 1000$ s/mm2, 2.0 mm isotropic voxel size, 63 slices, TE $= 95$ ms, TR $= 8700$ ms; a T1 image, 1 $.0$ mm isotropic voxel size, 176 slices, TE $= 2.98$ ms, TR $= 2300$ ms; a T2 image, 1.0 mm $\times$ 1.0 mm $\times$ 2.0 mm, 77 slices, TE $= 84$ ms, TR $= 14620$ ms and a PD image, 1.0 mm $\times$ 1.0 mm $\times$ 2.0 mm, 77 slices, TE $= 3240$ ms, TR $= 19$ ms. The diffusion data was first linearly interpolated to 1.0 mm isotropic resolution, before tensor estimation.

6.3.2 Segmentation of the thalamus as a whole

As a preliminary step prior to the application of our segmentation method, the entire thalamus was segmented using ANIMAL + INSECT [Collins et al., 1999], an algorithm for improved automatic segmentation of gross anatomical structures of the human brain. It merges the output of a tissue classification process (INSECT) with gross anatomical region masks, automatically defined by non-linear registration of a given data set with a probabilistic anatomical atlas (ANIMAL).

The result of the segmentation of the thalamus as a whole was used in the experiment as the outer marker for the hierarchical watershed. The hierarchical watershed and the choice of markers are better explained in Subsection 6.3.3.

6.3.3 Automatic segmentation based on TMG

The proposed automatic segmentation method is based on the computation of the tensorial morphological gradient (TMG) of a diffusion tensor field. Inspired by the morphological gradient, a tensorial morphological gradient (TMG) was defined and first described in previous work [Rittner et al., 2007]. It was then used, together with a tensorial representation of colors, to segment color images. The concept of TMG was expanded in subsequent work [Rittner and Lotufo, 2008], where it was applied to segment synthetic diffusion tensor images.

The morphological gradient is one of several existing gradients used in image processing to detect edges and is dependant on the size and shape of the chosen structuring element. Using a flat structuring element at each point, the morphological gradient yields the difference between the maximum and the minimum values over the neighborhood at the point determined by the flat structuring element [Heijmans, 1994]. The use of a three-dimensional structuring element leads to a morphological gradient that takes into account the neighborhood in all directions, and not only in an specific plane.

Let $E = \mathbb{Z} \times \mathbb{Z}$ be the set of all points in the tensorial image f. The tensorial morphological gradient (TMG) is defined by

$$\nabla_B^T(f)(x) = \bigvee_{y,z \in B_x} d(\mathbf{T}_y, \mathbf{T}_z), \tag{6.1}$$

$\forall x \in E$, where d represent any of the tensor similarity measures presented in the DTI literature [Pierpaoli and Basser, 1996, Alexander et al., 1999, Jones et al., 1999, Wang and Vemuri, 2005], $B \subset E$ is a structuring element centered at the origin of E, $\mathbf{T}_y$ is the tensor that represents the diffusion in y, and $\mathbf{T}_z$ is the tensor that represents the diffusion in z (y and z are in the neighborhood of x, defined by B_x). ∇_B^T is the proposed TMG. Experiment used a 6-connected structuring element and the Frobenius Norm as the similarity measure in the TMG computation.

Once the tensorial information was translated into a scalar image, the next step was to segment it using the watershed transform [Beucher and Meyer, 1992, Vincent and Soille, 1991]. The critical step in the watershed segmentation is the proper choice of markers. The classical watershed places the markers automatically at each regional minimum of the image. This usually leads to an over-segmentation and is not adequate for medical imaging applications. To solve the over-segmentation problem, hierarchical approaches are considered, in order to retain the most significant regions of the image at different scales [Meyer, 2001].

The dynamics of regional minima have been used to build this hierarchy, that can be interpreted as a set of region adjacencies, wherein an ordering is determined by a valuation, which can be controlled

by the relative altitudes of the regional minima. The contrast dynamic of a regional minimum, also known as the height extinction value, is defined as the minimal climb required for a path starting from a regional minimum to reach another one with strictly lower altitude, the climb being the difference in altitude between the highest point of the path and the regional minimum under study.

Similarly, the area extinction value can be seen as a size dynamic and the volume extinction value as a shape and contrast dynamic [Dougherty and Lotufo, 2003]. In our experiment, after computing the TMG of the original image, the n structures in the image with the greatest volume extinction values were automatically selected. The n markers assigned to these regions, together with the outer marker generated by the ANIMAL segmentation, were then used in the watershed transform, which segmented the TMG map into n regions. In this experiment, $n = 14$ regions were used.

The watershed transform and other morphological functions used here can be found in the "SDC Morphology Toolbox for MATLAB" [Dougherty and Lotufo, 2003]. The TMG computation and the segmentation algorithm was implemented in MATLAB 7.0 . The results obtained from application of the proposed segmentation method were qualitatively compared to Morel's histological atlas.

6.4 Results

This section presents experimental results of the proposed method described in Section 6.3. Although most images depict only one slice of the result to facilitate visualization, it is important to point out that the structuring element used in the TMG computation and in the watershed transform was 3D. In other words, the proposed segmentation method was applied in a 3D manner, and not slice by slice.

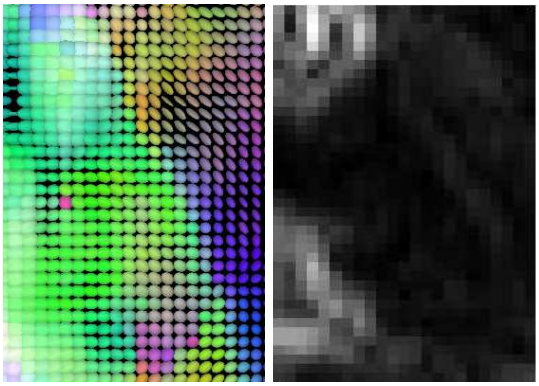

Fig. 6.1: Diffusion tensors in the thalamus region (left) and respective computed TMG (right). To distinguish the clusters is not a trivial task, even for the human eye.

Fig. 6.1 shows the diffusion tensor ellipsoids and the TMG map in a region including the thalamus. Although the details in the resultant TMG map are not visible to the human eye, information about

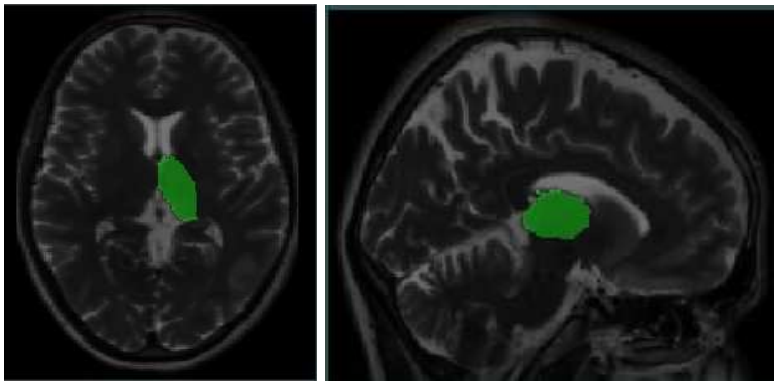

Fig. 6.2: ANIMAL+INSECT segmentation for right thalamus: transverse (left) and sagittal (right) views.

the different orientation of the distinct nuclei is present.

Fig. 6.2 presents the segmentation result for the right thalamus using the ANIMAL+INSECT method. From the resulting labeled image, a binary mask was generated and then used as the outer marker for the hierarchical watershed.

One slice of the watershed segmentation result is shown in Fig. 6.3, beside an illustration from Morel's atlas [Morel et al., 1997]. The correspondence between the atlas and the segmented nuclei can be appreciated in this figure by observing the colors of the nuclei in both images. Note that while the VLa (red outline in atlas illustration) was detected in this dataset, it is not visible here. Due to anatomical variation, it was not possible to find one view of the segmentation result that showed all of the nuclei in any one slice of the atlas illustration. The segmented nuclei can also be seen in Fig. 6.4, this time in a 3D visualization mode.

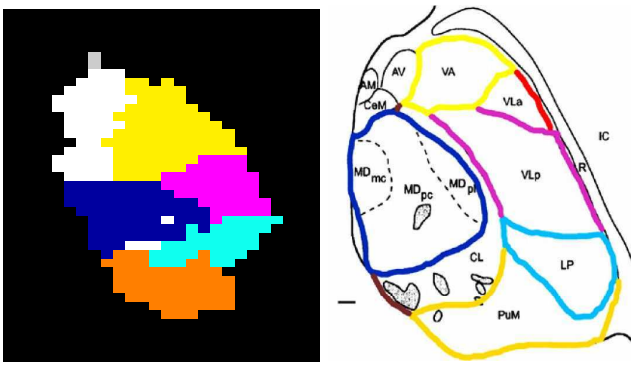

Fig. 6.3: Nuclei obtained by watershed segmentation compared to Morel's histological atlas. The segmentation algorithm delineated the main nuclei, such as the Pulvinar (PuM), the Medial Dorsal (MD), the Ventral Lateral (VL), the Lateral Posterior (LP) and the Ventral Anterior (VA).

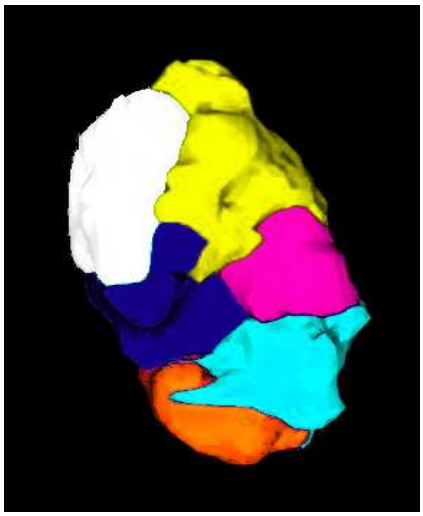

Fig. 6.4: 3D view of obtained nuclei using the proposed segmentation method.

6.5 Discussion

In this paper, the nuclei of the human thalamus are dissociated by applying the hierarchical watershed transform to the tensorial morphological gradient (TMG) map computed from the diffusion tensor field. The TMG processes the tensorial information and transforms it into a scalar image, in order to use the hierarchical watershed to segment it. It has the advantage of using all of the information in the diffusion tensor for the segmentation.

In this experiment, the user-input number of expected nuclei was fourteen, a number that is common in thalamic parcellation experiments [Wiegell et al., 2003, Jonasson et al., 2007]. There is no precise number of thalamic nuclei, as different atlases define nuclei on different scales. In our segmentation, clusters of small nuclei are grouped as one, e.g., the AM, AV, and CeM appear as one nucleus (white in Fig. 6.3 and Fig. 6.4). If the input number of nuclei were smaller, there would be further clustering of nuclei with similar diffusion properties. If the input number were larger, we would expect splitting of some of the nuclei segmented here. Small subnuclei are not expected to be segmentable using a diffusion MRI dataset such as this. At this spatial resolution of 2.0 mm $\times$ 2.0 mm $\times$ 2.0 mm, they cover only a few voxels, and at higher spatial resolution, the signal to noise ratio of the data would be unacceptable.

In conclusion, our experiment confirmed that the proposed algorithm is able to delineate the main nuclei of the thalamus. As opposed to other DTI-based segmentation algorithms, the proposed method requires no manual seed placement and/or initial surface delineation: the only parameter is the number of regions into which the image should be segmented. This independance from user input could be a major advantage in the application of this technique to large scale studies of normal anatomy, development, or disease.

Capítulo 7

Conclusões

Enquanto os métodos de segmentação baseada em DTI propostos até o presente momento foram adaptações de métodos já existentes, originalmente desenvolvidos para segmentação de imagens escalares, a idéia original desta tese foi utilizar um método de segmentação já bastante conhecido e validado, como a transformada de *watershed* para realizar a segmentação. Ao invés de adaptar o *watershed* para trabalhar com imagens tensoriais, decidiu-se propor mapas escalares baseados na morfologia matemática que retivessem toda a informação relevante contida nos tensores e, a partir deste mapa escalar, conseguir a segmentação da imagem aplicando a transformada de *watershed*.

A primeira contribuição original desta tese foi, portanto, o estudo dos mapas escalares já propostos na literatura, estudo este descrito na Seção 5.3 e Seção 5.4. Percebeu-se que a grande maioria dos mapas escalares existentes, como por exemplo, a anisotropia fracional (FA), o índice de reticulado e o índice de coerência, não é adequada para a tarefa de segmentação. Ou são medidas que não levam em consideração os vizinhos (intravoxel) e, além disso, são baseadas apenas nos autovalores dos tensores, desconsiderando a informação direcional. Ou são mapas escalares que utilizam informações dos vizinhos e que também levam em consideração autovalores e autovetores, mas neste caso consideram sempre a vizinhança 8-conexa (bi-dimensional) e fazem uma média das medidas obtidas nesta vizinhança. Enquanto a média suaviza as bordas, a vizinhança bi-dimensional não garante a percepção da coerência de estruturas que estejam em uma direção ortogonal ao plano de varredura.

A proposta do gradiente morfológico tensorial (TMG), introduzido na Seção 2.5, para imagens coloridas e depois estendido para imagens de tensores de difusão na Seção 3.3, e de outros mapas escalares baseados em conceitos da morfologia matemática (Seção 5.4.3) foi a segunda contribuição importante desta tese. Primeiro, porque o conceito de vizinhança é inerente à morfologia matemática, representado pelo elemento estruturante. Qualquer elemento estruturante pode ser utilizado para o cálculo dos mapas escalares propostos, mas, considerando-se a natureza tridimensional das imagens do cérebro, faz muito mais sentido o uso de vizinhança 6 ou 26-conexa do que a 8-conexa dos

mapas escalares já existentes. Além disso, graças à utilização de conceitos da morfologia matemática, introduzimos medidas intervoxel baseadas em max (ou $max - min$), ao invés da média. Enquanto a média suaviza as bordas, a operação de $max - min$ ressalta as bordas, o que é desejável como etapa intermediária no processo de segmentação por *watershed*.

Outra contribuição original deste trabalho foi a aplicação do *watershed* hierárquico para segmentar imagens de tensores de difusão. O método de segmentação baseado nos mapas escalares propostos e no *watershed* não requer escolha manual de marcadores, definição de superfície inicial nem escolha de muitos parâmetros, como discutido na Seção 4.3.2. O único parâmetro a ser escolhido pelo usuário, no *watershed* hierárquico, é o número de regiões em que a imagem será segmentada. Experimentos mostraram a aplicação bem sucedida do método proposto para segmentar tanto imagens de difusão sintéticas (Seção 3.5) quanto imagens de tensores de difusão do cérebro (Seção 4.3 e Seção 6.4).

Ainda devemos citar como resultado importante desta tese, não só o método de segmentação de imagens coloridas baseado no TMG e no *watershed* hierárquico, apresentado e testado na Seção 2.6, mas também a representação de imagens coloridas por tensores proposta na Seção 2.3 e Seção 2.4. Além de permitir a segmentação das imagens coloridas, a representação tensorial proposta abre novas frentes de estudo que permitem a aplicação de conceitos e métodos da álgebra tensorial para resolver problemas que envolvam imagens coloridas.

Nesta tese propusemos soluções para problemas de segmentação de imagens tensoriais utilizando conceitos da morfologia matemática. O gradiente morfológico tensorial, bem como os demais mapas escalares permitiram a segmentação destas imagens através da transformada de *watershed*. Experimentos apresentados na Seção 4.3 e na Seção 5.6 mostraram que o método de segmentação proposto é capaz de segmentar diversas estruturas do cérebro. Contudo, enquanto que para algumas estruturas, os resultados foram facilmente reproduzidos para todas as imagens adquiridas, o método de segmentação de DTI baseado no TMG e na transformada de *watershed* não se mostrou robusto na tarefa de identificação de subdivisões de pequenas estruturas do cérebro, como por exemplo, do tálamo (Seção 6.4). Os bons resultados obtidos para um determinado conjunto de dados não se repetiram para outros conjuntos.

7.1 Trabalhos futuros

Dentre os aspectos que podem contribuir significativamente para o aumento da robustez do método e que abrem oportunidades de trabalhos futuros, podemos citar: a melhoria da qualidade das imagens de tensores de difusão, novas medidas para o cálculo do TMG e a escolha de marcadores para a segmentação por *watershed*.

A baixa resolução das imagens de tensores de difusão nos obrigou a interpolar os dados, o que, sem dúvida, interferiu nos resultados. Bordas abruptas, que provavelmente seriam facilmente identificadas no cálculo do gradiente, passaram a ter uma transição mais suave, dificultando sua detecção. Novos esquemas de aquisição de imagens de tensores de difusão estão sendo constantemente testados e, dentro em breve, imagens com uma melhor resolução e melhor relação sinal-ruído deverão estar disponíveis. Também estão sendo estudados novos esquemas de cálculo dos tensores a partir das imagens de difusão adquiridas, bem como novos métodos de regularização e pré-processamento dos dados de difusão.

Outro aspecto que pode vir a melhorar ainda mais os resultados de segmentação obtidos, principalmente aqueles que envolveram imagens reais e foram apresentadios na Seção 4.3, Seção 5.6 e Seção 6.4, é a utilização de novas métricas no cálculo do TMG. Ao estudarmos as medidas intervoxel existentes e observarmos as segmentações baseadas no TMG calculado com cada uma delas, concluímos que a Norma de Forbenius, apesar de não ser invariante a transformações afins, apresentou os melhores resultados. Isso devido a seu comportamento linear com relação às variações de anisotropia e traço, em contraste com o comportamento exponencial da maioria das medidas estudadas. Isso nos leva a crer que, se encontrarmos uma medida intervoxel que mantenha as mesmas características lineares da Norma de Frobenius, e ao mesmo tempo seja invariante a transformações afins, os resultados obtidos no cálculo do TMG e subseqüente segmentação serão ainda melhores.

Outra questão que prejudica a robustez do método de segmentação de DTI proposto, baseado no TMG e em *watershed* é a escolha automática de marcadores do *watershed* baseada na dinâmica dos mínimos regionais. Se considerarmos que a relação sinal-ruído é baixa, os mínimos regionais escolhidos como marcadores às vezes não são mínimos regionais de fato. Neste caso, a segmentação obtida pode não ser coerente com as estruturas desejadas, principalmente quando se trata de subdivisões com volumes não maiores do que 10 ou 12 voxels (como os núcleos do tálamo apresentados na Seção 6.4). Buscar novos métodos para a escolha de marcadores pode, portanto, nos levar a resultados melhores, mais robustos e conseqüentemente, reproduzíveis.

Uma alternativa para resolver a questão da escolha de marcadores seria a utilização da informação de classificação dos tecidos cerebrais. Em testes preliminares, identificamos um grande potencial na utilização do TMG, em conjunto com outros mapas escalares, para a classificação de tecido cerebral em três classes: substância cinzenta, substância branca e líquido céfalo-raquidiano. Além do resultado desta classificação ter utilidade por si só, ela também poderia ser útil como marcador para o *watershed*. Ao buscar a segmentação de uma estrutura composta de substância branca, por exemplo, envolvida por substância cinzenta, poderíamos utilizar a região identificada como substância cinzenta na etapa de classificação, como marcador externo no *watershed*.

Outra possibilidade seria o uso de algoritmos de segmentação baseados em atlas para ajudar na

identificação de marcadores para o *watershed*. Os algoritmos de segmentação baseados em atlas nem sempre são precisos na detecção das bordas reais das estruturas cerebrais, principalmente na presença de patologias que causem deformação/atrofia de tais estruturas. De qualquer modo, como são capazes de localizar de forma aproximada as estruturas que se deseja segmentar, poderiam ser utilizados na escolha de marcadores para o nosso método. Uma vez realizada a segmentação baseada em atlas, bastaria calcular os centróides da estruturas segmentadas, ou realizar a erosão destas estruturas e utilizar o resultado como marcador do método de segmentação baseado no TMG e no *watershed*.

Referências Bibliográficas

[Alexander et al., 1999] Alexander, D., Gee, J., and Bajcsy, R. (1999). Similarity measures for matching diffusion tensor images. In *Proceedings of the British Machine Vision Conference*, volume 1, pages 93–102, Nottingham, UK.

[Arsigny et al., 2006] Arsigny, V., Fillard, P., Pennec, X., and Ayache, N. (2006). Log-Euclidean metrics for fast and simple calculus on diffusion tensors. *Magnetic Resonance in Medicine*, 56(2):411–421.

[Assaf et al., 2003] Assaf, B. A., Mohamed, F. B., Abou-Khaled, K. J., Williams, J. M., Yazeji, M. S., Haselgrove, J., and Faro, S. H. (2003). Diffusion tensor imaging of the hippocampal formation in temporal lobe epilepsy. *AJNR Am J Neuroradiol*, 24(9):1857–1862.

[Awate and Gee, 2007] Awate, S. and Gee, J. (2007). A fuzzy, nonparametric segmentation framework for DTI and MRI analysis. In *IPMI*, pages 296–307.

[Basser and Pajevic, 2000] Basser, P. and Pajevic, S. (2000). Statistical artifacts in diffusion tensor MRI (DT-MRI) caused by background noise. *Magn. Reson. in Medicine*, 44:41–50.

[Basser and Pierpaoli, 1996] Basser, P. and Pierpaoli, C. (1996). Microstructural and physiological features of tissues elucidated by quantitative-diffusion-tensor MRI. *J. Magn. Reson.*, 111(3):209–219.

[Basser et al., 2000] Basser, P. J., Pajevic, S., Pierpaoli, C., Duda, J., and Aldroubi, A. (2000). In vivo fiber tractography using dt-mri data. *Magnetic resonance in medicine : official journal of the Society of Magnetic Resonance in Medicine / Society of Magnetic Resonance in Medicine*, 44(4):625–632.

[Batchelor et al., 2005] Batchelor, P. G., Moakher, M., Atkinson, D., Calamante, F., and Connelly, A. (2005). A rigorous framework for diffusion tensor calculus. *Magnetic Resonance in Medicine*, 53(1):221–225.

[Behrens et al., 2003] Behrens, T. E., Johansen-Berg, H., Woolrich, M. W., Smith, S. M., Wheeler-Kingshott, C. A., Boulby, P. A., Barker, G. J., Sillery, E. L., Sheehan, K., Ciccarelli, O., Thompson, A. J., Brady, J. M., and Matthews, P. M. (2003). Non-invasive mapping of connections between human thalamus and cortex using diffusion imaging. *Nat Neurosci*, 6(7):750–757.

[Beucher and Meyer, 1992] Beucher, S. and Meyer, F. (1992). The morphological approach to segmentation: the watershed transformation. In *Mathematical Morphology in Image Processing*, chapter 12, pages 433–481. Marcel Dekker.

[Bigün et al., 1991] Bigün, J., Granlund, G. H., and Wiklund, J. (1991). Multidimensional orientation estimation with applications to texture analysis and optical flow. *IEEE Trans. Patt. Anal. Machine Intell.*, 13(8):775–790.

[Bishop and Goldberg, 1980] Bishop, R. L. and Goldberg, S. I. (1980). *Tensor Analysis on Manifolds*. Dover.

[Borsotti et al., 1998] Borsotti, M., Campadelli, P., and Schettini, R. (1998). Quantitative evaluation of color image segmentation results. *Pattern Recognition Letters*, (19):741–747.

[Boykov and Jolly, 2001] Boykov, Y. Y. and Jolly, M.-P. (2001). Interactive graph cuts for optimal boundary and region segmentation of objects in N-D images. *International Conference in Computer Vision*, 01:105.

[Bozzali et al., 2002] Bozzali, M., Cercignani, M., Sormani, M., Comi, G., and Filippi, M. (2002). Quantification of brain gray matter damage in different MS phenotypes by use of diffusion tensor MR imaging. *A.J.N.R.*, 23:985–988.

[Bozzali and Cherubini, 2007] Bozzali, M. and Cherubini, A. (2007). Diffusion tensor MRI to investigate dementias: a brief review. *Magn Reson Imaging*, 25(6):969–977.

[Bozzali et al., 2005] Bozzali, M., Falini, A., Cercignani, M., Baglio, F., Alberoni, M., Vezzuli, P., Olivotto, F., Mantovani, F., Shallice, T., Scotti, G., Canal, N., and Nemni, R. (2005). Brain tissue damage in dementia with lewy bodies: an in vivo diffusion tensor MRI study. *Brain*, 128(7):pp.1595 – 1604.

[Broit, 1981] Broit, C. (1981). *Optimal Registration of Deformed Images*. PhD thesis, Computer and Information Science Dept., University of Pennsylvania, Philadelphia, PA.

[Brummer et al., 1993] Brummer, M. E., Mersereau, R. M., Eisner, R. L., and Lewine, R. R. (1993). Automatic detection of brain contours in MRI data sets. *IEEE Transactions on Medical Imaging*, 12(2):153–166.

[Campbell et al., 2005] Campbell, J. S., Siddiqi, K., Rymar, V. V., Sadikot, A. F., and Pike, G. B. (2005). Flow-based fiber tracking with diffusion tensor and Q-ball data: validation and comparison to principal diffusion direction techniques. *Neuroimage*, 27(4):725–736.

[Castellano et al., 2003] Castellano, G., Lotufo, R., Falcao, A., and Cendes, F. (2003). Characterization of the human cortex in MR images through the image foresting transform. *ICIP 2003*, 1:357–360.

[Cercignani et al., 2001] Cercignani, M., Inglese, M., Pagani, E., Comi, G., and Filippi, M. (2001). Mean diffusivity and fractional anisotropy histograms of patients with multiple sclerosis. *AJNR Am J Neuroradiol*, 22(5):952–958.

[Chan et al., 2007] Chan, L.-L., Rumpel, H., Yap, K., Lee, E., Loo, H.-V., Ho, G.-L., Fook-Chong, S., Yuen, Y., and Tan, E.-K. (2007). Case control study of diffusion tensor imaging in Parkinson's disease. *Journal of neurology, neurosurgery, and psychiatry*, 78:1383–6.

[Chanussot and Lambert, 1998] Chanussot, J. and Lambert, P. (1998). Total Ordering Based on Space Filling Curves for Multivalued Morphology. In Heijmans, H. J. and Roerdink, J. B., editors, *Mathematical morphology and its applications to image and signal processing*, volume 12 of *Computational Imaging and Vision*, pages 51–58. Kluwer Academic Publishers, Dordrecht.

[Collins et al., 1999] Collins, D. L., Zijdenbos, A. P., Baaré, W. F. C., and Evans, A. C. (1999). ANIMAL+INSECT: Improved cortical structure segmentation. In *IPMI 99: Proceedings of the 16th International Conference on Information Processing in Medical Imaging*, pages 210–223, London, UK. Springer-Verlag.

[Collins et al., 1995] Collins, L. D., Holmes, C. J., Peters, T. M., and Evans, A. C. (1995). Automatic 3-D model-based neuroanatomical segmentation. *Human Brain Mapping*, 3(3):190–208.

[Cousty et al., 2009] Cousty, J., Bertrand, G., Najman, L., and Couprie, M. (2009). Watershed cuts: Minimum spanning forests and the drop of water principle. *IEEE Transactions on Pattern Analysis and Machine Intelligence*, 31(8):1362–1374.

[Danielson, 2003] Danielson, D. A. (2003). *Vectors and Tensors in Engineering and Physics*. Westview (Perseus).

[de Luis Garcia et al., 2005] de Luis Garcia, R., Deriche, R., Rousson, M., and Alberola-Lopez, C. (2005). Tensor processing for texture and colour segmentation. In *SCIA*, pages 1117–1127.

[Dong et al., 2004] Dong, Q., Welsh, R. C., Chenevert, T. L., Carlos, R. C., Maly-Sundgren, P., Gomez-Hassan, D. M., and Mukherji, S. K. (2004). Clinical applications of diffusion tensor imaging. *J. of Magn. Reson. Imag.*, 19(1):6–18.

[Dougherty and Lotufo, 2003] Dougherty, E. R. and Lotufo, R. A. (2003). *Hands-on Morphological Image Processing*, volume TT59. SPIE.

[Duan et al., 2007] Duan, Y., Li, X., and Xi, Y. (2007). Thalamus segmentation from diffusion tensor magnetic resonance imaging. *Journal of Biomedical Imaging*, 2007(2):1–1.

[Eriksson et al., 2001] Eriksson, S. H., Rugg-Gunn, F. J., Symms, M. R., Barker, G. J., and Duncan, J. S. (2001). Diffusion tensor imaging in patients with epilepsy and malformations of cortical development. *Brain*, 124(3):617–626.

[Falcão et al., 2002] Falcão, A., Costa, L., and da Cunha, B. (2002). Multiscale skeletons by image foresting transform and its applications to neuromorphometry. *Pattern Recognition*, 35(7):1571–1582.

[Falcão et al., 2001] Falcão, A., Cunha, B., and Lotufo, R. (2001). Design of connected operators using the image foresting transform. In *Medical Imaging 2001: Image Processing*, volume 4322 of *SPIE Conference*, pages 468–479.

[Falcão et al., 2004] Falcão, A., Stolfi, J., and Lotufo, R. (2004). The image foresting transform: Theory, algorithms, and applications. *IEEE Trans. Pattern Anal. Mach. Intell.*, 26(1):19–29.

[Fillard, 2005] Fillard, P. (2005). DTI-track. `http://www-sop.inria.fr/asclepios/personnel/Pierre.Fillard/softwares/FiberTracking/`.

[Fillard et al., 2009] Fillard, P., Souplet, J., and Toussaint, N. (2009). MedINRIA. `http://www-sop.inria.fr/asclepios/software/MedINRIA`.

[Flores et al., 2004] Flores, F., Polidório, A., and Lotufo, R. (2004). Color image gradients for morphological segmentation: the weighted gradient improved by automatic imposition of weights. In *SIBGRAPI*, pages 146–153, Curitiba, Brazil.

[Flores et al., 2006] Flores, F., Polidório, A., and Lotufo, R. (2006). The weighted gradient: a color image gradient applied to morphological segmentation. *Journal of the Brazilian Computer Society - JBCS*, 11(3):53–63.

[Freidlin et al., 2007] Freidlin, R. Z., Özarslan, E., Komlosh, M. E., Chang, L.-C., Koay, C. G., Jones, D. K., and Basser, P. J. (2007). Parsimonious model selection for tissue segmentation and classification applications: A study using simulated and experimental DTI data. *IEEE Trans. Med. Imag.*, 26(11):1576–1584.

[Gerig et al., 1991] Gerig, G., Martin, J., Kikinis, R., Kübler, O., Shenton, M. E., and Jolesz, F. A. (1991). Automating segmentation of dual-echo MR head data. In *IPMI 91: Proceedings of the 12th International Conference on Information Processing in Medical Imaging*, pages 175–187, London, UK. Springer-Verlag.

[Gonzalez and Woods, 1992] Gonzalez, R. C. and Woods, R. E. (1992). *Digital Image Processing*. Addison-Wesley Publishing Company.

[Grimaud, 1992] Grimaud, M. (1992). A New Measure of Contrast: the Dynamics. In SPIE, editor, *Image Algebra and Morphological Image Processing III*, volume 1769, pages 292–305.

[Gupta et al., 2006] Gupta, R. K., Saksena, S., Hasan, K. M., Agarwal, A., Haris, M., Pandey, C. M., and Narayana, P. A. (2006). Focal Wallerian degeneration of the corpus callosum in large middle cerebral artery stroke: Serial diffusion tensor imaging. *Journal of Magnetic Resonance Imaging*, 24(3):549–555.

[Hanbury, 2003] Hanbury, A. (2003). A 3D-polar coordinate colour representation well adapted to image analysis. In *SCIA*, pages 804–811.

[He et al., 2004] He, R., Mehta, M., and Narayana, P. (2004). Color coding for visualization of the directional information of DTI. In *IEMBS '04. 26th Annual International Conference of the IEEE*, volume 1, pages 1857–1859.

[Heijmans, 1994] Heijmans, H. J. A. M. (1994). *Morphological Image Operators*. Academic Press, Boston.

[Hein et al., 2004] Hein, P. A., Eskey, C. J., Dunn, J. F., and Hug, E. B. (2004). Diffusion-weighted imaging in the follow-up of treated high-grade gliomas: tumor recurrence versus radiation injury. *AJNR Am J Neuroradiol*, 25(2):201–209.

[Jiang et al., 2006] Jiang, H., van Zijl, P. C., Kim, J., Pearlson, G. D., and Mori, S. (2006). DtiStudio: resource program for diffusion tensor computation and fiber bundle tracking. *Comput Methods Programs Biomed*, 81(2):106–116.

[Johansen-Berg et al., 2005] Johansen-Berg, H., Behrens, T., Sillery, E., Ciccarelli, O., Wheeler-Kingshott, C., Thompson, A., Smith, S., and Matthews, P. (2005). Functional-anatomical validation and individual variation of diffusion tractography-based segmentation of the human thalamus. *Cerebral Cortex*, 15:31–39.

[Jonasson et al., 2005] Jonasson, L., Bresson, X., Hagmann, P., Cuisenaire, O., Meuli, R., and Thiran, J. (2005). White matter fiber tract segmentation in DT-MRI using geometric flows. *Medical Image Analysis*, 9(3):223–236.

[Jonasson et al., 2003] Jonasson, L., Hagmann, P., Bresson, X., Meuli, R., Cuisenaire, O., and Thiran, J.-P. (2003). White matter mapping in DT-MRI using geometric flows. In *Proceedings of the 9th International Workshop on Computer Aided System Theory*, pages 80–82, Spain.

[Jonasson et al., 2007] Jonasson, L., Hagmann, P., Pollo, C., Bresson, X., Wilson, C. R., Meuli, R., and Thiran, J.-P. (2007). A level set method for segmentation of the thalamus and its nuclei in DT-MRI. *Signal Processing*, 87(2):309–321.

[Jones et al., 1999] Jones, D., Horsfield, M., and Simmons, A. (1999). Optimal strategies for measuring diffusion in anisotropic systems by magnetic resonance imaging. *Magnetic Resonance in Medicine*, 42(3):515–525.

[Kapouleas, 1990] Kapouleas, I. (1990). Segmentation and feature extraction for magnetic resonance brain image analysis. In *Proceedings of the 10th International Conference on Pattern Recognition*, volume i, pages 583–590 vol.1.

[Kingsley, 2006] Kingsley, P. B. (2006). Introduction to diffusion tensor imaging mathematics: Part II. anisotropy, diffusion-weighting factors, and gradient encoding schemes. *Concepts in Magnetic Resonance Part A*, 28A(2):123–154.

[Klingberg et al., 1999] Klingberg, T., Vaidya, C. J., Gabrieli, J. D. E., Moseley, M. E., and Hedehus, M. (1999). Myelination and organization of the frontal white matter in children: a diffusion tensor MRI study. *NeuroReport*, 10:2812–2821.

[Lenglet et al., 2006] Lenglet, C., Rousson, M., and Deriche, R. (2006). A statistical framework for DTI segmentation. In *Proceedings of the International Symposium on Biomedical Imaging*, pages 794–797. IEEE.

[Li and Wünsche, 2005] Li, J. and Wünsche, B. C. (2005). An analysis of algorithms for in vivo fibre. In *Proceedings of IVCNZ '05*, pages 183–188, New Zealand.

[Lobo et al., 2009] Lobo, R., Rittner, L., Lotufo, R., and Magalhães, L. (2009). MM-DTI. `http://www.students.ic.unicamp.br/~ra064041/mm-dti/gallery#animation`.

[Lotufo and Falcão, 2000] Lotufo, R. and Falcão, A. (2000). The Ordered Queue and the Optimality of the Watershed Approaches. In *Proceedings of the 5th International Symposium on Mathematical Morphology*, pages 341–350, Palo Alto (CA), USA. Kluwer Academic.

[Lotufo et al., 2002] Lotufo, R., Falcão, A., and Zampirolli, F. (2002). IFT-watershed from gray-scale marker. In *SIBGRAPI02: Proceedings of the XV Brazilian Symposium on Computer Graphics and Image Processing*, pages 146–152, Fortaleza, Brazil. IEEE Press.

[Maas et al., 2004] Maas, L. C., Mukherjee, P., Carballido-Gamio, J., Veeraraghavan, S., Miller, S. P., Partridge, S. C., Henry, R. G., Barkovich, A. J., and Vigneron, D. B. (2004). Early laminar organization of the human cerebrum demonstrated with diffusion tensor imaging in extremely premature infants. *NeuroImage*, 22(3):1134 – 1140.

[Mardor et al., 2001] Mardor, Y., Roth, Y., Lidar, Z., Jonas, T., Pfeffer, R., Maier, S. E., Faibel, M., Nass, D., Hadani, M., Orenstein, A., Cohen, J. S., and Ram, Z. (2001). Monitoring response to convection-enhanced taxol delivery in brain tumor patients using diffusion-weighted magnetic resonance imaging. *Cancer Res*, 61(13):4971–4973.

[Martin et al., 2001] Martin, D., Fowlkes, C., Tal, D., and Malik, J. (2001). A database of human segmented natural images and its application to evaluating segmentation algorithms and measuring ecological statistics. In *Proceedings of the 8th International Conference in Computer Vision*, volume 2, pages 416–423.

[Meyer, 1996] Meyer, F. (1996). The dynamics of minima and contours. In P. Maragos, R. S. Butt, M., editor, *ISMM 3rd. Computational Imaging and Vision*, pages 329–336.

[Meyer, 2001] Meyer, F. (2001). An overview of morphological segmentation. *International Journal of Pattern Recognition and Artificial Intelligence*, 15(7):1089–1118.

[Miller et al., 1993] Miller, M., Christensen, G., Amit, Y., and Grenander, U. (1993). Mathematical textbook of deformable neuroanatomies. *Proceedings of the National Academy of Sciences of the United States of America*, 90(24):11944–11948.

[Morel et al., 1997] Morel, A., Magnin, M., and Jeanmonod, D. (1997). Multiarchitectonic and stereotactic atlas of the human thalamus. *J Comp Neurol*, 387(4):588–630.

[Mori and van Zijl, 2002] Mori, S. and van Zijl, P. C. (2002). Fiber tracking: principles and strategies - a technical review. *NMR Biomed*, 15(7-8):468–480.

[Najman and Schmitt, 1996] Najman, L. and Schmitt, M. (1996). Geodesic saliency of watershed contours and hierarchical segmentation. *IEEE Trans. Pattern Anal. Mach. Intell.*, 18(12):1163–1173.

[Nicoletti et al., 2006] Nicoletti, G., Lodi, R., Condino, F., Tonon, C., Fera, F., Malucelli, E., Manners, D., Zappia, M., Morgante, L., Barone, P., Barbiroli, B., and Quattrone, A. (2006). Apparent diffusion coefficient measurements of the middle cerebellar peduncle differentiate the Parkinson variant of MSA from Parkinson's disease and progressive supranuclear palsy. *Brain*, 129(10):2679–2687.

[Niogi et al., 2007] Niogi, S. N., Mukherjee, P., and McCandliss, B. D. (2007). Diffusion tensor imaging segmentation of white matter structures using a reproducible objective quantification scheme (ROQS). *NeuroImage*, 35:166–174.

[Pajevic and Pierpaoli, 1999] Pajevic, S. and Pierpaoli, C. (1999). Color schemes to represent the orientation of anisotropic tissues from diffusion tensor data: Application to white matter fiber tract mapping in the human brain. *Magn. Reson. Med.*, 42:526–540.

[Papadakis et al., 1999] Papadakis, N., Xing, D., Houston, G., Smith, J., Smith, M., James, M., Parsons, A., Huang, C.-H., Hall, L., and Carpenter, T. (July 1999). A study of rotationally invariant and symmetric indices of diffusion anisotropy. *Magnetic Resonance Imaging*, 17:881–892(12).

[Park et al., 2004] Park, H. J., Kubicki, M., Westin, C.-F., Talos, I. F., Brun, A., Pieper, S., Kikinis, R., Jolesz, F. A., McCarley, R. W., and Shenton, M. E. (2004). Method for combining information from white matter fiber tracking and gray matter parcellation. *American Journal of Neuroradiology*, 25:1318–1324.

[Parker et al., 2003] Parker, G. J. M., Haroon, H. A., and Wheeler-Kingshott, C. A. M. (2003). A framework for a streamline-based probabilistic index of connectivity (PICo) using a structural interpretation of MRI diffusion measurements. *J Magn Reson Imaging*, 18(2):242–254.

[Peeters et al., 2008] Peeters, T., Rodrigues, P., Vilanova, A., and ter Haar Romeny, B. (2008). Analysis of distance/similarity measures for diffusion tensor imaging. In *Visualization and Processing of Tensor Fields: Advances and Perspectives*. Springer, Berlin.

[Pennec et al., 2006] Pennec, X., Fillard, P., and Ayache, N. (2006). A Riemannian framework for tensor computing. *International Journal Computer Vision*, 66(1):41–66.

[Pierpaoli and Basser, 1996] Pierpaoli, C. and Basser, P. J. (1996). Toward a quantitative assessment of diffusion anisotropy. *Magnetic Resonance in Medicine*, 36(6):893–906.

[Rettmann et al., 2002] Rettmann, M., Han, X., Xu, C., and Prince, J. (2002). Automated sulcal segmentation using watersheds on the cortical surface. *Neuroim.*, 15(2):329 – 344.

[Rittner et al., 2009a] Rittner, L., Appenzeller, S., and Lotufo, R. (2009a). Segmentation of brain structures by watershed transform on tensorial morphological gradient of diffusion tensor imaging. In *SIBGRAPI09: Proceedings of the XXII Brazilian Symposium on Computer Graphics and Image Processing*, Rio de Janeiro, Brazil. IEEE Computer Society.

[Rittner et al., 2007] Rittner, L., Flores, F., and Lotufo, R. (2007). New tensorial representation of color images: Tensorial morphological gradient applied to color image segmentation. In *SIBGRAPI07: Proceedings of the XX Brazilian Symposium on Computer Graphics and Image Processing*, pages 45–52, Belo Horizonte, Brazil. IEEE Computer Society.

[Rittner et al., 2009b] Rittner, L., Flores, F., and Lotufo, R. (2009b). A tensorial framework for color images. *Pattern Recognition Letters*. In press.

[Rittner and Lotufo, 2008] Rittner, L. and Lotufo, R. (2008). Diffusion tensor imaging segmentation by watershed transform on tensorial morphological gradient. In *SIBGRAPI08: Proceedings of the XXI Brazilian Symposium on Computer Graphics and Image Processing*, pages 196–203, Campo Grande, Brazil. IEEE Computer Society.

[Rittner and Lotufo, 2009] Rittner, L. and Lotufo, R. (2009). Segmentation of DTI based on tensorial morphological gradient. In *Medical Imaging 2009: Image Processing*, volume 7259, page 72591E. SPIE.

[Rousson et al., 2004] Rousson, M., Lenglet, C., and Deriche, R. (2004). Level set and region based surface propagation for diffusion tensor MRI segmentation. In Sonka, M., Kakadiaris, I. A., and Kybic, J., editors, *Proceedings of the ECCV Workshops CVAMIA and MMBIA*, volume 3117 of *Lecture Notes in Computer Science*, pages 123–134. Springer.

[Rovaris et al., 2005] Rovaris, M., Gass, A., Bammer, R., Hickman, S. J., Ciccarelli, O., Miller, D. H., and Filippi, M. (2005). Diffusion MRI in multiple sclerosis. *Neurology*, 65(10):1526–1532.

[Skare et al., 2000] Skare, S., Li, T., Nordell, B., and Ingvar, M. (2000). Noise considerations in the determination of diffusion tensor anisotropy. *Magnetic resonance imaging*, 18(6):659–69.

[Soille and Vincent, 1990] Soille, P. and Vincent, L. (1990). Determining watersheds in digital pictures via flooding simulations. In *Visual Communications and Image Processing*, pages 240–250. SPIE. volume 1360.

[Symms et al., 2004] Symms, M., Jager, H. R., Schmierer, K., and Yousry, T. A. (2004). A review of structural magnetic resonance neuroimaging. *Journal of Neurology, Neurosurgery and Psychiatry*, 75(9):1235–1244.

[Talbot et al., 1998] Talbot, H., Evans, C., and Jones, R. (1998). Complete ordering and multivariate mathematical morphology: algorithms and applications. In Heijmans, H. J. and Roerdink, J. B., editors, *Mathematical Morphology and its Applications to Image and Signal Processing*, volume 12 of *Computational Imaging and Vision*, pages 27–34. Kluwer Academic Publishers, Dordrecht.

[Tessa et al., 2008] Tessa, C., Giannelli, M., Nave, R. D., Lucetti, C., Berti, C., Ginestroni, A., Bonuccelli, U., and Mascalchi, M. (2008). A whole-brain analysis in De Novo Parkinson disease. *AJNR Am J Neuroradiol*, page ajnr.A0900.

[Thivard et al., 2006] Thivard, L., Adam, C., Hasboun, D., Clémenceau, S., Dezamis, E., Lehéricy, S., Dormont, D., Chiras, J., Baulac, M., and Dupont, S. (2006). Interictal diffusion MRI in partial epilepsies explored with intracerebral electrodes. *Brain*, 129(Pt 2):375–385.

[Thomalla et al., 2005] Thomalla, G., Glauche, V., Weiller, C., and Röther, J. (2005). Time course of Wallerian degeneration after ischaemic stroke revealed by diffusion tensor imaging. *J Neurol Neurosurg Psychiatry*, 76(2):266–268.

[Vachier and Meyer, 1995] Vachier, C. and Meyer, F. (1995). Extinction value: A new measurement of persistence. In *Proceedings of the 1995 IEEE Workshop on Nonlinear Signal and Image Processing*, volume I, pages 254–257. IEEE.

[van de Weijer and Gevers, 2004] van de Weijer, J. and Gevers, T. (2004). Tensor based feature detection for color images. In *12th Color Imaging Conference: Color Science and Engineering Systems, Technologies, Applications*, volume 12, pages 100–105.

[van de Weijer et al., 2006] van de Weijer, J., Gevers, T., and Smeulders, A. W. M. (2006). Robust photometric invariant features from the color tensor. *IEEE Transactions on Image Processing*, 15(1):118–127.

[Vilanova et al., 2005] Vilanova, A., Zhang, S., Kindlmann, G., and Laidlaw, D. H. (2005). An introduction to visualization of diffusion tensor imaging and its applications. In *Visualization and Image Processing of Tensor Fields*. Springer-Verlag.

[Vincent and Soille, 1991] Vincent, L. and Soille, P. (1991). Watersheds in digital spaces: an efficient algorithm based on immersion simulations. 13(6):583–598.

[Wang and Vemuri, 2005] Wang, Z. and Vemuri, B. C. (2005). DTI segmentation using an information theoretic tensor dissimilarity measure. *IEEE Transactions on Medical Imaging*, 24(10):1267–1277.

[Weldeselassie and Hamarneh, 2007] Weldeselassie, Y. and Hamarneh, G. (2007). DT-MRI segmentation using graph cuts. In *Medical Imaging 2007: Image Processing, Proceedings of the SPIE*. SPIE.

[Westin et al., 2002] Westin, C.-F., Maier, S., Mamata, H., Nabavi, A., Jolesz, F., and Kikinis, R. (2002). Processing and visualization for diffusion tensor MRI. *Medical Image Analysis*, 6(93-108).

[Wiegell et al., 2003] Wiegell, M., Tuch, D., Larson, H., and Wedeen, V. (2003). Automatic segmentation of thalamic nuclei from diffusion tensor magnetic resonance imaging. *NeuroImage*, 19:391–402.

[Xu et al., 2002] Xu, D., Mori, S., Solaiyappan, M., van Zijl, P. C. M., and Davatzikos, C. (2002). A framework for callosal fiber distribution analysis. *NeuroImage*, 17:1131–1143.

[Zenzo, 1986] Zenzo, S. D. (1986). A note on the gradient of a multi-image. *Computer Vision, Graphics, and Image Processing*, 33:116–125.

[Zhang et al., 2005] Zhang, H., Yushkevich, P. A., and Gee, J. C. (2005). Deformable registration of diffusion tensor MR images with explicit orientation optimization. In *MICCAI*, pages 172–179.

[Zhang et al., 2004] Zhang, S., Kindlmann, G., and Laidlaw, D. H. (2004). Diffusion tensor MRI visualization. In *Visualization Handbook*. Academic Press.

[Zhukov et al., 2003] Zhukov, L., Museth, K., Breen, D., Whitaker, R., and Barr, A. (2003). Level set modeling and segmentation of DT-MRI brain data. *Journal of Electronic Imaging*, 12:125–133.

[Ziyan et al., 2006] Ziyan, U., Tuch, D., and Westin, C. (2006). Segmentation of thalamic nuclei from DTI using spectral clustering. In *MICCAI06: Proceedings of the Medical Image Computing and Computer Assisted Intervention*, Lecture Notes in Computer Science, pages 807–814, Denmark.

Apêndice A

MM-DTI: ferramenta de visualização e segmentação de imagens de tensores de difusão

No início deste trabalho, percebeu-se que seria difícil trabalhar com as imagens de tensores de difusão sem uma ferramenta adequada de visualização. Tendo isso em vista, iniciou-se um projeto de Iniciação Científica cujo objetivo foi desenvolver esta ferramenta, que além de visualização, permitiria a segmentação das imagens de tensores de difusão pelo método proposto. É fácil perceber que o desenvolvimento da ferramenta em questão foi de suma importância para a conclusão deste trabalho. Basta comparar as imagens dos capítulos iniciais com as dos últimos capítulos. Enquanto as imagens apresentadas nos Capítulos 2 e 3 desta tese foram geradas apenas com o MATLAB 7.0, as imagens dos Capítulos 4, 5 e 6 foram geradas com a ajuda da ferramenta desenvolvida.

O artigo a seguir, intitulado "MM-DTI: Visualization and segmentation tool for diffusion tensor images", foi submetido ao *International Symposium on Biomedical Imaging - ISBI'10*, e descreve a ferramenta desenvolvida.

A.1 Abstract

In this paper we present the MM-DTI, a tool that offers diffusion tensor processing functionalities based on mathematical morphology operators. Through a graphic user interface, it is possible to visualize a diffusion tensor image, to compute its tensorial morphological gradient (TMG) and finally, to segment it using the watershed transform. It offers three different visualization modes (tensor glyphs, volume rendering and tracts), three color mappings (FA-based, TMG-based and Segmentation-based) and an animation module.

A.2 Introduction

Diffusion tensor imaging (DTI) is a relatively new MRI modality able to quantify the anisotropic diffusion of water molecules in highly structured biological tissues [Basser and Pierpaoli, 1996]. DTI has been used to demonstrate subtle abnormalities in a variety of diseases (including stroke, multiple sclerosis, dyslexia, and schizophrenia) and is currently becoming part of many routine clinical protocols [Eriksson et al., 2001, Assaf et al., 2003, Symms et al., 2004].

One of the fundamental problems in understanding and working with diffusion tensor data is its three-dimensional and multi-variate nature. Visualizing such tensor fields is not a trivial task. Various techniques for visualizing diffusion tensor data were reported so far [Westin et al., 2002, Zhang et al., 2004, Vilanova et al., 2005] and can be categorized in two groups. One is the series of image-based methods in which each voxel value represents local anisotropy measure or principal direction of diffusion, and the 3D rendering of those images by volume rendering or surface rendering of the isosurface. The other is the group of symbolic (or geometric) display methods by using various types of glyph such as ellipsoids. A few DTI visualization tools have been recently developed and can be found in [Park et al., 2004, Fillard, 2005, Jiang et al., 2006, Fillard et al., 2009].

DTI-based segmentation is relatively new and is also a very challenging task. Only in the last decade some approaches for DTI-based segmentation have been proposed [Weldeselassie and Hamarneh, 2007, Wang and Vemuri, 2005, Awate and Gee, 2007].

This work presents the MM-DTI, a tool that deal with these two important problems of DTI: visualization and segmentation. Its visualization approach consists of three different and independent viewing modes and three color mapping options. The segmentation functionality is based on a method proposed in previous work [Rittner and Lotufo, 2008], where the segmentation of diffusion tensor fields is performed using mathematical morphology operators, such as the tensorial morphological gradient (TMG) and the watershed transform. The developed tool allows automatic and manual definition of markers as input to the watershed-based segmentation method.

The tool also provides an exclusive animation mode for the tensor glyphs viewing mode, which interpolates the glyph position on the 3D grid in the direction of the principal eigenvector of the tensor. While Section A.3 describes the developed tool, Section A.4 presents the results, and conclusions can be found in Section A.5.

A.3 MM-DTI

MM-DTI [Lobo et al., 2009] is a diffusion tensor image processing program running under Windows. It is suitable for tasks such as tensor field visualization, color mapping and DTI-based

segmentation. It was developed in C++ and uses OpenGL.

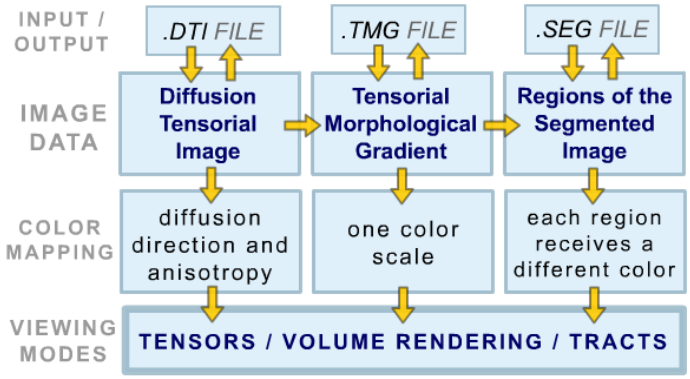

Fig. A.1: MM-DTI main functionality

As shown in Fig. A.1, it provides three viewing modes (tensor glyphs, volume rendering and tracts) and each one of them can reproduce a kind of color mapping (diffusion direction, TMG or segmentation labels). In addition to visualization functionalities, MM-DTI supports advanced techniques of image processing to calculate the TMG and to perform watershed-based segmentation.

Fig. A.2 contains one slice of a synthetic diffusion data (torus) illustrating all nine combinations of viewing modes and color mappings.

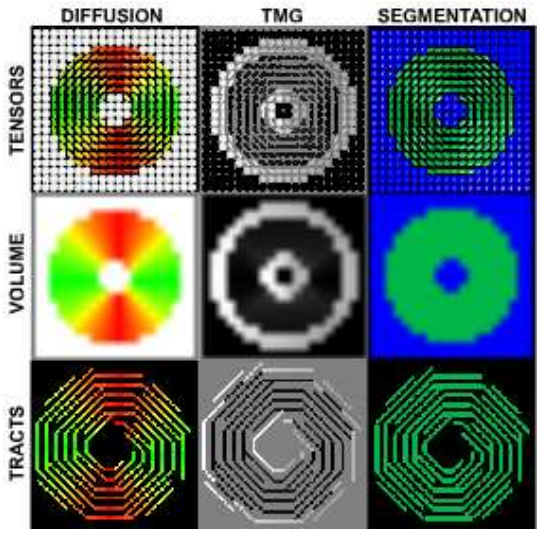

Fig. A.2: Viewing modes at rows and color mapping at columns for one slice of a torus

A.3.1 Viewing modes

MM-DTI has three viewing modes: tensor glyphs, volume rendering and tracts. The color assigned to each voxel or region of an image depends on the chosen color mapping.

Tensors glyphs

The program allows the representation of tensors by three types of objects: ellipsoids, boxes and lines. Such objects are arranged in a 3D-grid in the position of the voxel corresponding to each tensor, and are oriented following the direction of the principal eigenvector (e_1). The size of an object, in each dimension, is given by the square root of the corresponding eigenvalue (λ_i). Fig. A.3 illustrates such objects.

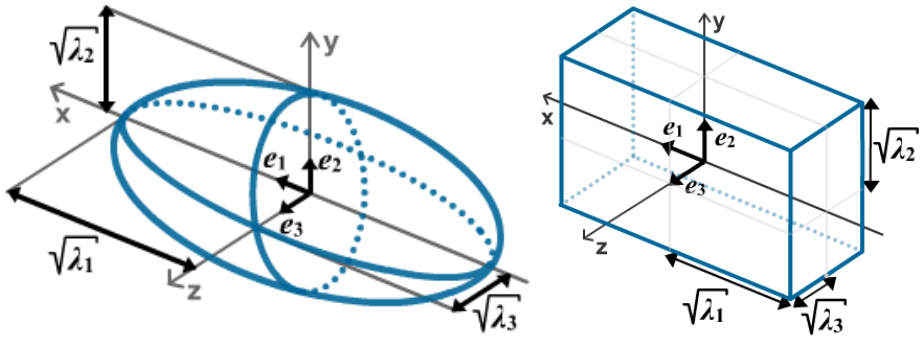

Fig. A.3: Objects representing a tensor: an ellipsoid and a box

Volume Rendering

The volume rendering viewing mode maps the color scheme being displayed on a 3D texture data, allowing the user to see the entire volume rendering or just some textured slices of the image. The slice mode is a feature also available in tensors and tracts viewing modes.

Tracts

The viewing mode by tracts generates tubes (or fibers) connecting a tensor X to other tensor Y, for which X points to. The principal eigenvector orientation of X is used to determine Y. This is done for all tensors of the image, resulting in multiples paths to the movement of water molecules. It is important to notice that a minimum value of fractional anisotropy (*FA*) is used to determine which tensors can generate a path, in order to avoid using tensors that have predominantly isotropic movement. Moreover, the thickness of a tube that represents a path is given by $1 - FA$, so thicker tubes represent more isotropic diffusion.

A.3.2 Color mapping

The tool provides three types of color mapping: main diffusion direction, tensorial morphological gradient (TMG) and segmentation labels.

Diffusion

Several color mapping schemes for diffusion tensor are available in DTI literature [Pajevic and Pierpaoli, 1999, Hein et al., 2004]. Usually, in the diffusion image, the color of each voxel is related to the direction of the principal eigenvector associated to that voxel, as well as its fractional anisotropy (*FA*). In our system we assign a color (RGB) based on *FA*, allowing the user to choose the desired *FA* influence in the color computation:

$$R = e_{1x} + (1 - e_{1x})(1 - FA)^n \tag{A.1}$$

$$G = e_{1y} + (1 - e_{1y})(1 - FA)^n \tag{A.2}$$

$$B = e_{1z} + (1 - e_{1z})(1 - FA)^n \tag{A.3}$$

with *FA* given by:

$$FA = \sqrt{\frac{3}{2}} \frac{\sqrt{(\lambda_1 - T_{av})^2 + (\lambda_2 - T_{av})^2 + (\lambda_3 - T_{av})^2}}{\sqrt{\lambda_1^2 + \lambda_2^2 + \lambda_3^2}}, \tag{A.4}$$

where T_{av} is the mean diffusivity [Basser and Pierpaoli, 1996].

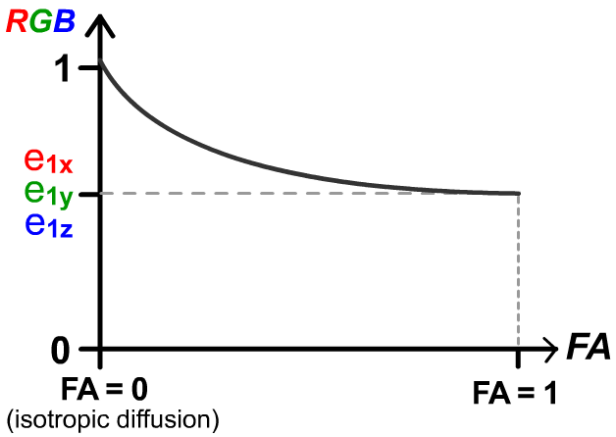

Fig. A.4: RGB *vs* *FA* color function graph with $n = 2$.

This method was developed to allow the user to choose the *FA* influence in tensors color. In Fig. A.4, it is possible to see graphically the influence of the characteristics of a tensor in determining

its color in a diffusion image. The curvature of the function in the graph is determined by n, which represents the chromatic sensitivity to *FA*. For larger values of n, the value of *FA* will have less influence on the final color of the object representing the tensor. The opposite is also true, i.e. for lower values of n, the colors associated with the tensor will be more influenced by the value of *FA*, tending to white. The traditional linear approach is also available just setting n to 1. In MM-DTI is also available a variation of the diffusion image color mapping, which assigns colors to tensor using only the *FA* value.

Tensorial morphological gradient (TMG)

In previous work, a tensorial morphological gradient (TMG) was presented [Rittner and Lotufo, 2008] as a technique to transform the diffusion tensor image into a scalar map with meaningful values at edges of structures whose segmentation is desired. The TMG uses diffusion intervoxel measures and combines them to compute a gradient using concepts from mathematical morphology. The MM-DTI implements the TMG computation based on four similarity functions: dot product, tensorial dot product, Frobenius norm and J-Divergence [Pierpaoli and Basser, 1996, Alexander et al., 1999]. It is also possible to choose the structuring element used in TMG computation, and to choose the colors to be assigned to the minimum and maximum values of TMG. It is important to note that the computed TMG serves as input data for the segmentation function.

Segmentation labels

The watershed-based segmentation method is applied to the results of the TMG calculation to divide the original image into regions with similar diffusion characteristics [Rittner and Lotufo, 2008]. Each region is identified by a label, and then a common color is assigned to voxels belonging to the same region. The user chooses between manual or automatic markers placement for the watershed segmentation, and can also configure the assignment of colors to each label of the segmented image.

A.3.3 Animation

The tensor glyphs viewing mode has an extra feature (non-existent in other viewing modes), which provides an animation of the movement of water molecules through the interpolation of the object's position on the grid in the orientation and direction of the principal eigenvector [Lobo et al., 2009]. Since the original data of a diffusion tensorial image provides only the orientation of the eigenvector, and not the direction, we created a method that gives coherence to the animation by assigning direction to a tensor based on its neighbors. This method does a breadth-first search in the image, starting from a seed voxel, and determines the direction of each tensor in the image based on

its neighbors which have had their direction defined in order to minimize inconsistencies in the movement.

A.4 Results

Fig. A.5 shows the MM-DTI graphical user interface, with a slice of a diffusion tensorial image of a human brain on the center. The user interface allows camera operations, tensor/slice selection and simultaneous viewing modes. Through the "Settings" panel it is possible to configure preferences in visualization and image processing.

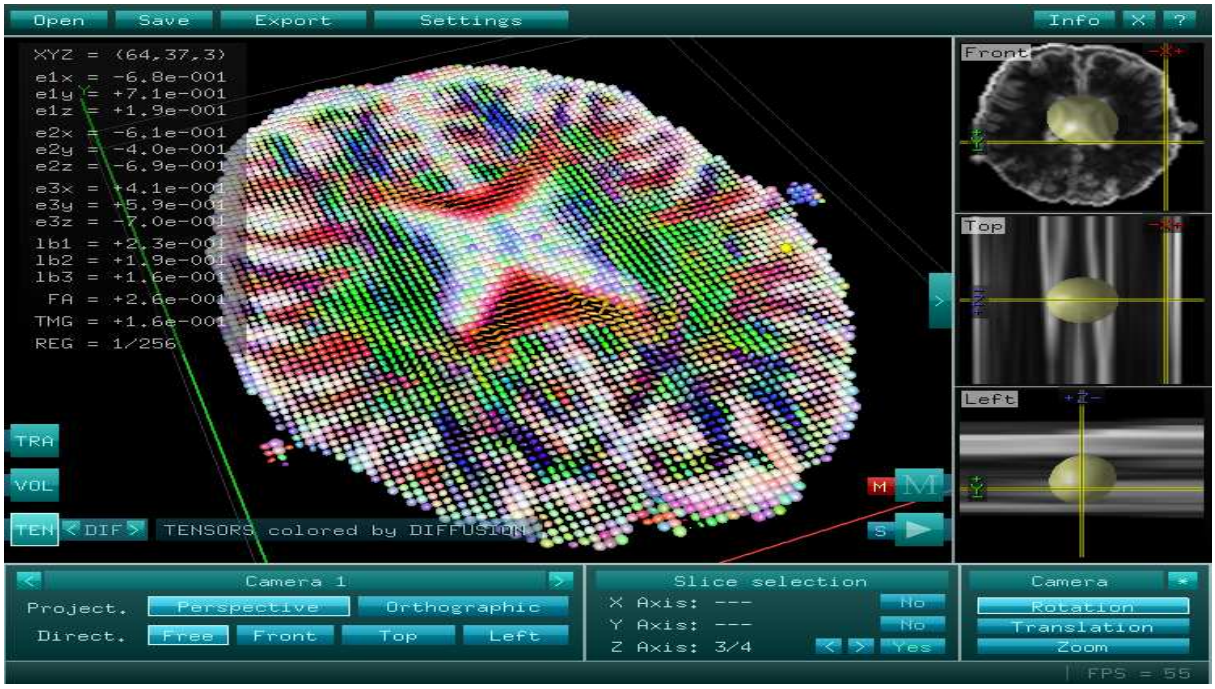

Fig. A.5: MM-DTI user interface

Fig. A.6 shows the three types of color mapping on a corpus callosum image. While Fig. A.6(a) shows ellipsoids colored by *FA*, Fig. A.6(b) shows ellipsoids colored by TMG and the markers placed by the user. Fig. A.6(c) depicts the segmentation result.

A.5 Conclusions

This paper presents the MM-DTI, a visualization and segmentation tool for diffusion tensor images. The MM-DTI visualization approach, which separates the data information in two

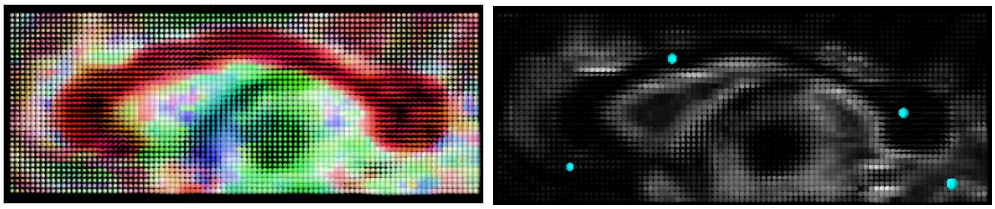

(a) Diffusion (b) computed TMG with markers

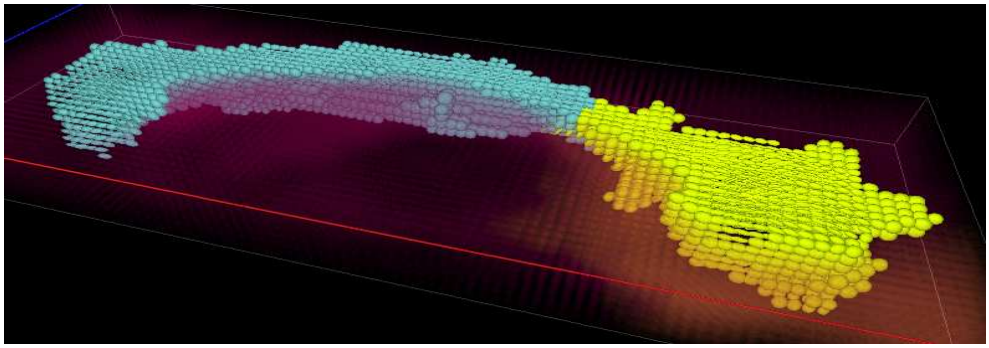

(c) Segmentation result

Fig. A.6: Steps for segmenting the corpus callosum

independent groups, named color mapping and viewing modes, allows the user to choose the best combination of visual information for each study case. In the segmentation functionality, the proposed method requires no manual seed placement and/or initial surface delineation, and it is possible to control the number of regions into which the image should be segmented. Finally, the tensor animation mode, which provides the possibility of dynamically viewing a DT field, renders a digital representation of the data closer to the diffusion phenomenon.

Apêndice B

Imagens coloridas do Capítulo 2

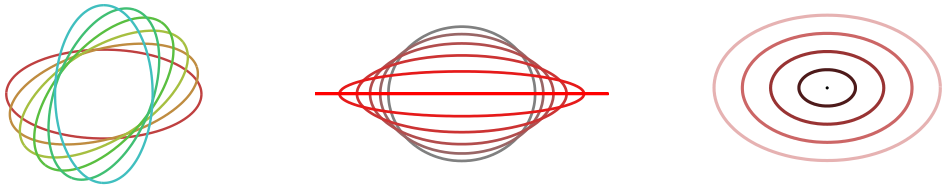

(a) Hue (b) Saturation (c) Luminance

Fig.2.2 Tensorial representation of HSL color information

(a) Selected region in the original image

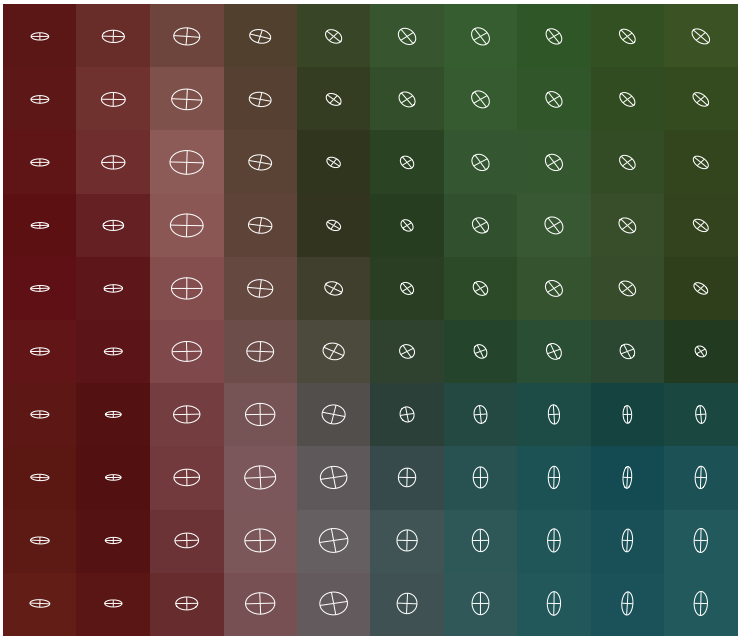

(b) Tensorial representation of colors for the selected region

Fig.2.3 Example of the tensorial representation of a color image

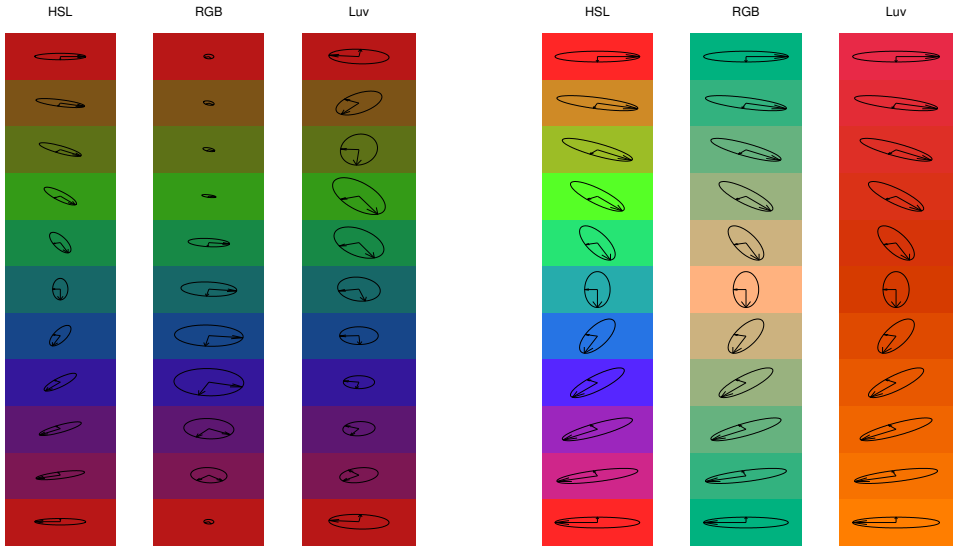

(a) Same colors (b) Same tensors

Fig.2.4 Extension of the tensorial representation to different color models

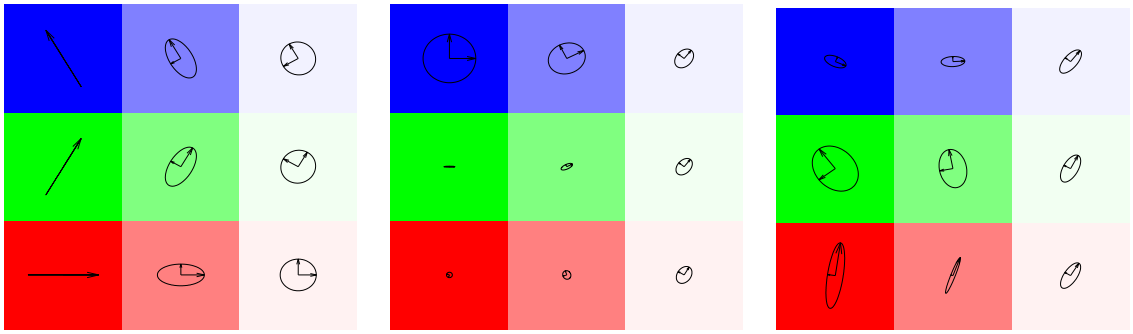

(a) HSL (b) RGB (c) $CIELUV$

Fig.2.5 Tensorial representation of colors based on different color models

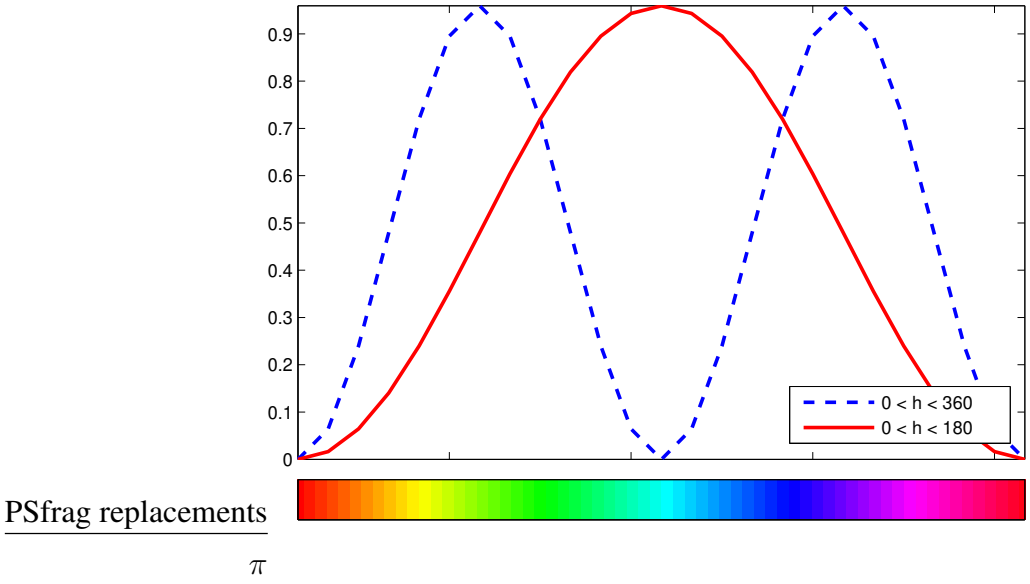

Fig.2.6 Dissimilarity between colors comparing original and modified hue scale

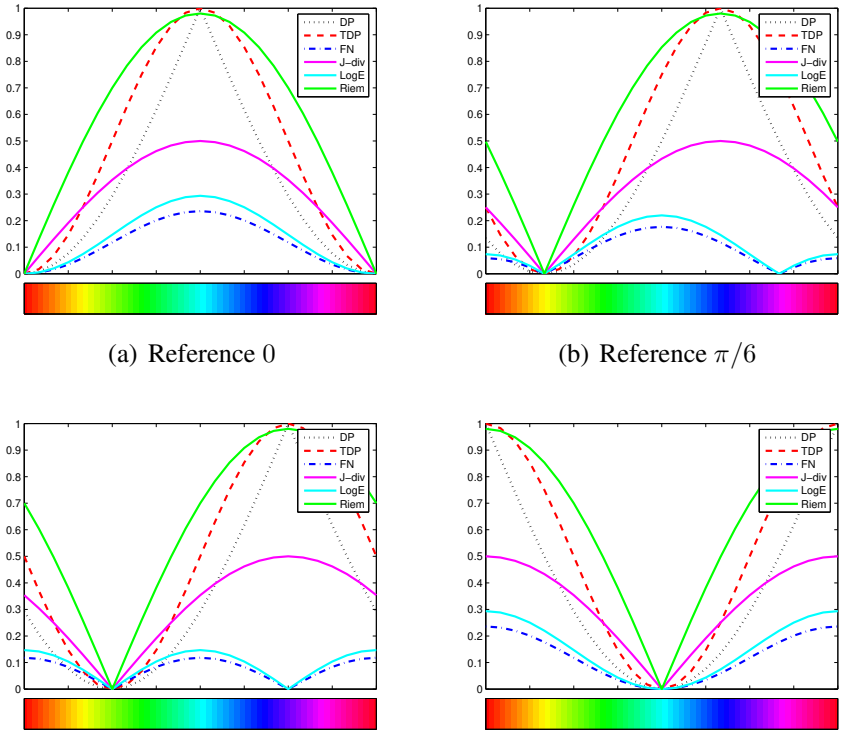

(a) Reference 0 (b) Reference $\pi/6$

(c) Reference $\pi/4$ (d) Reference $\pi/2$

Fig.2.7 Dissimilarity between a tensor and a reference, computed for different reference angles and by different measures

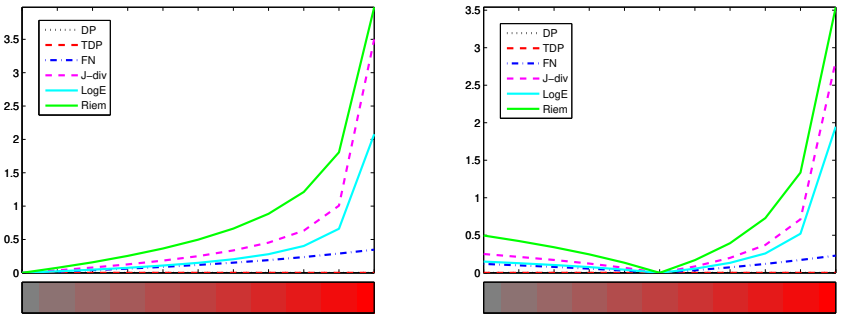

(a) Reference $s = 0$ (b) Reference $s = 0.5$

(c) Reference $s = 0.7$ (d) Reference $s = 1.0$

Fig.2.8 Dissimilarity between a tensor and a reference, computed for different reference saturations and by different measures

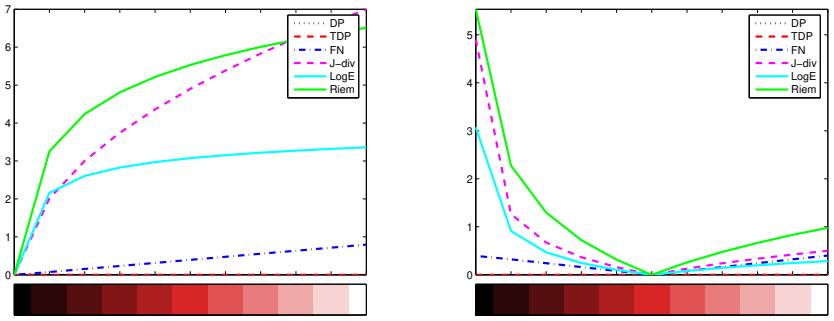

(a) Reference $l = 0$ (b) Reference $l = 0.5$

(c) Reference $l = 0.7$ (d) Reference $l = 1.0$

Fig.2.9 Dissimilarity between a tensor and a reference, computed for different reference luminances and by different measures

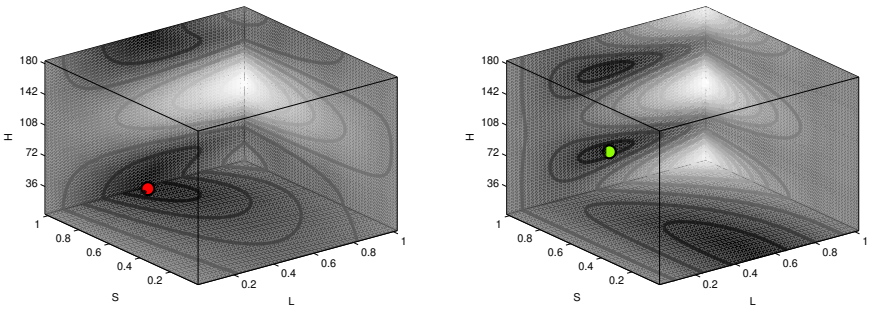

(a) FN ($h = 0$, $s = 1.0$, $l = 0.5$) (b) FN ($h = 0.25$, $s = 1$, $l = 0.5$)

Fig.2.10 Dissimilarity between all colors and a reference, computed using the Frobenius Norm for two different color references ($h = 0$ and $h = \pi/8$)

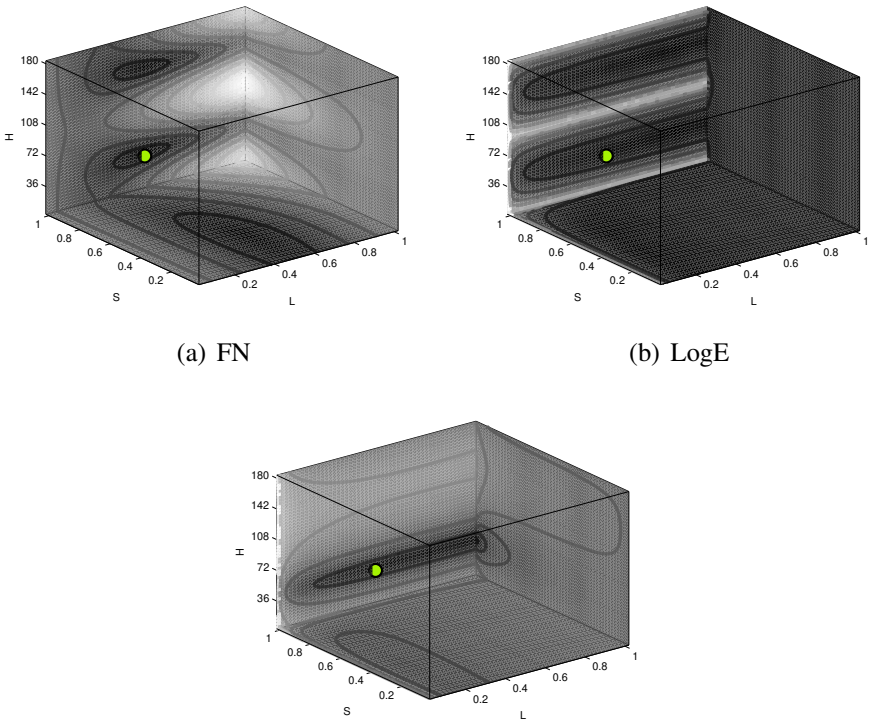

(a) FN

(b) LogE

(c) Riemannian

Fig.2.11 Dissimilarity between all colors and a reference ($h = \pi/8$, $s = 1$, $l = 0.5$), computed by different measures

(a) Original

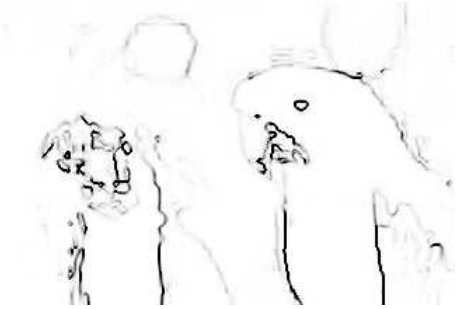

(b) Dot product

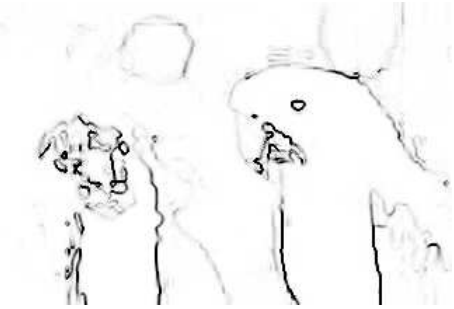

(c) Tensorial dot product

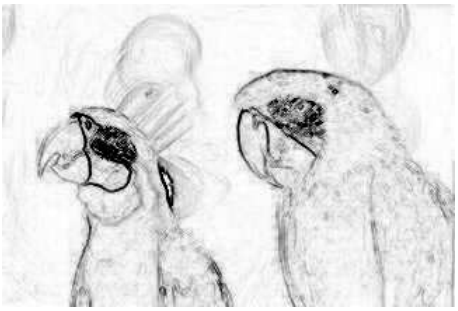

(d) Frobenius Norm

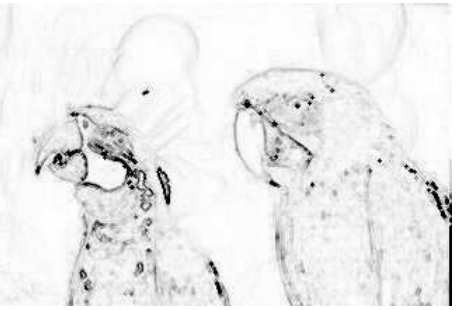

(e) J-divergence

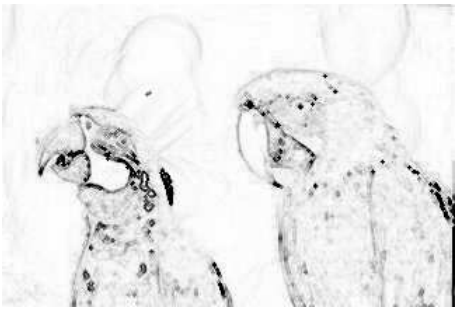

(f) Log-Euclidean distance

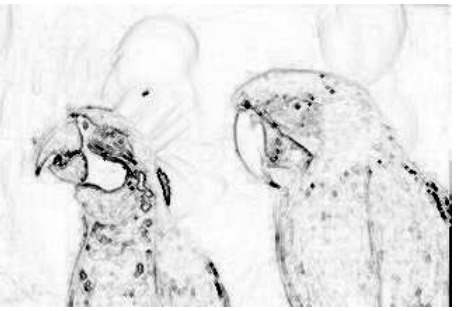

(g) Riemannian distance

Fig.2.12 Tensorial morphological gradients (TMGs) using different similarity measures

(a) Dot product

(b) Tensorial dot product

(c) Frobenius Norm

(d) J-divergence

(e) Log-Euclidean distance

(f) Riemannian distance

Fig.2.14 Watershed segmentation of the “parrots” image with 25 regions using TMGs

(a) Original image

(b) Selected region

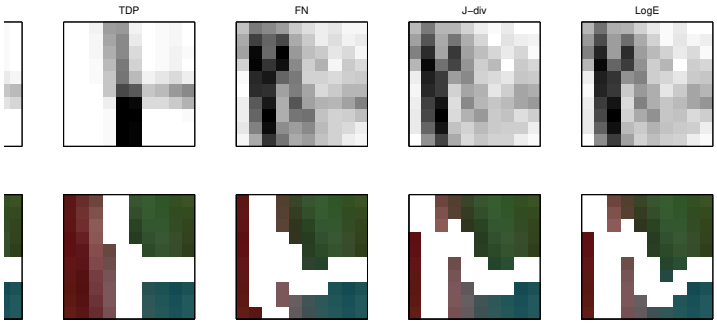

(c) Different similarity measures using HSL tensorial representation

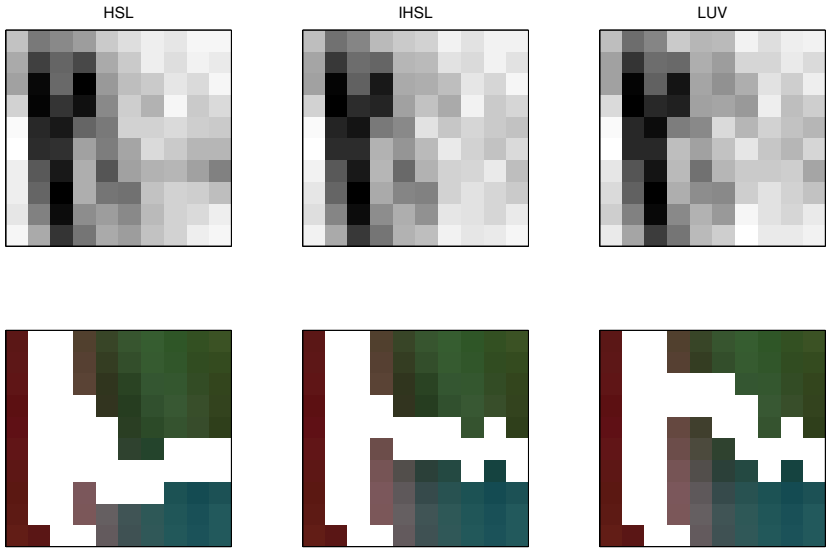

(d) FN measure using different color models for tensorial representation

Fig.2.15 Negated TMGs and segmentation results of a detail of the “parrots"image. The TMGs were computed using different similarity measures and different color models

(a) Selected region

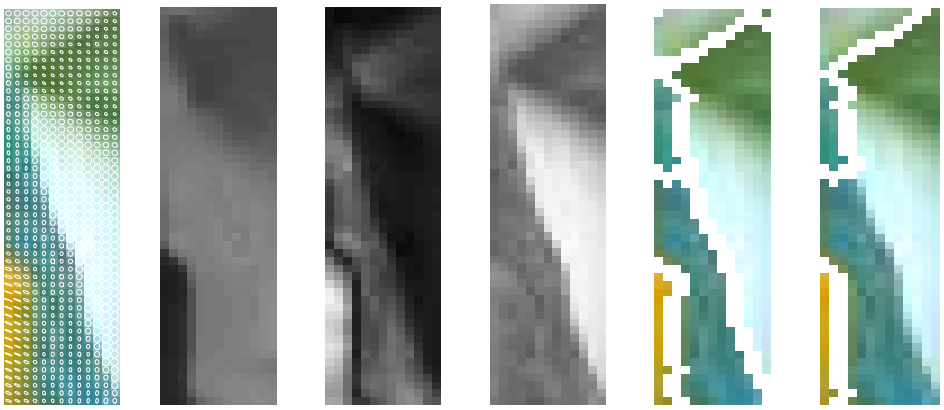

(b) Tensors (c) Hue (d) Sat (e) Lum (f) FN (g) Riem

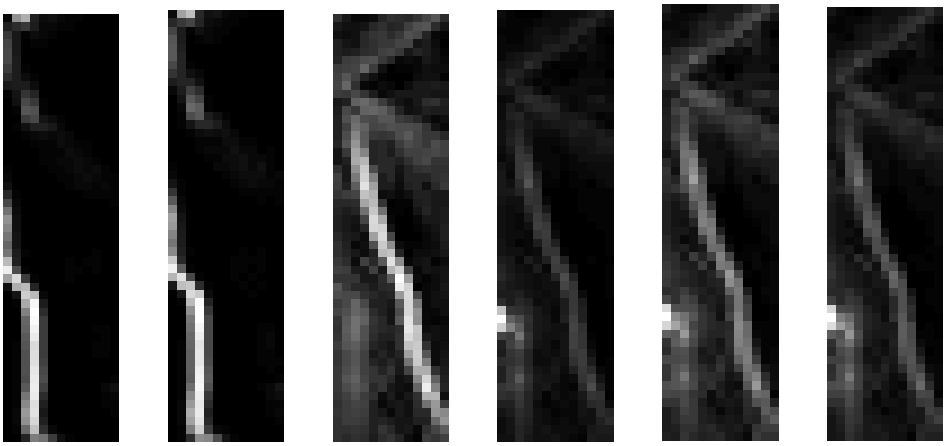

(h) DP (i) TDP (j) FN (k) Jdiv (l) LogE (m) Riem

Fig.2.16 Detail of the parrot image - color components, watershed results and TMGs

(a) DP (HSL) (b) DP ($IHSL$) (c) DP ($CIELUV$)

(d) FN (HSL) (e) FN ($IHSL$) (f) FN ($CIELUV$)

(g) LogE (HSL) (h) LogE ($IHSL$) (i) LogE ($CIELUV$)

Fig.2.17 Watershed segmentation results based on TMGs computed using different similarity measures and different color models

(a) 42049 (b) 227092

Fig.2.18 Two images from the Berkeley segmentation dataset (BSDS)

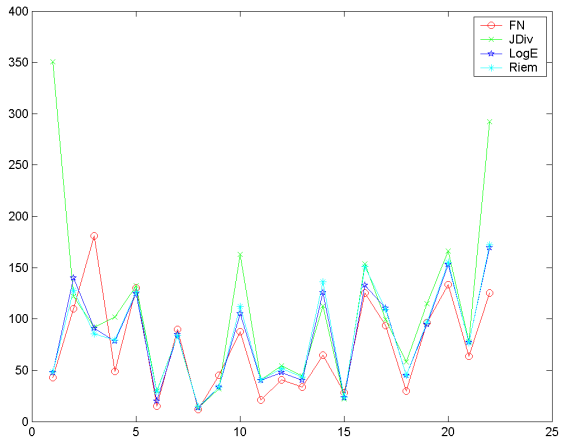

(a) The Borsotti Function F'

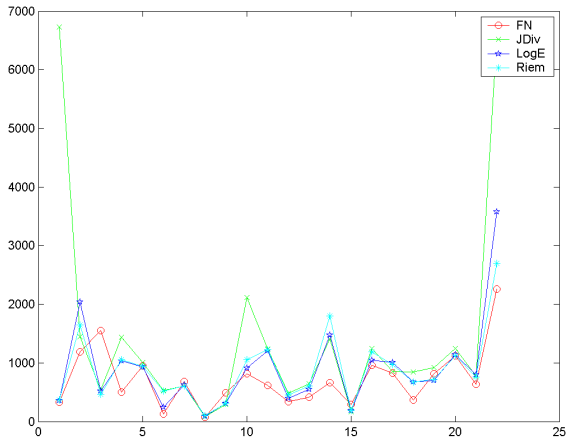

(b) The Borsotti Function Q

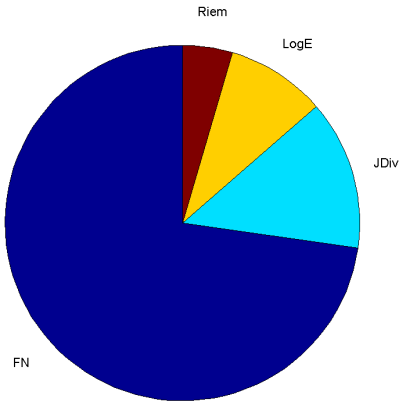

(c) Lowest Borsotti F' errors

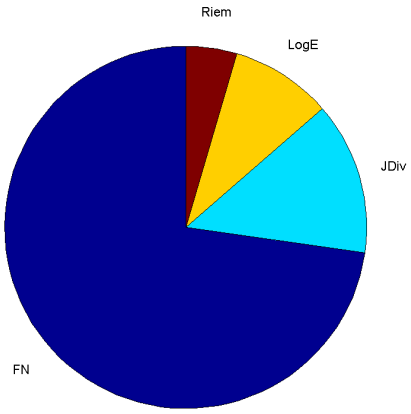

(d) Lowest Borsotti Q errors

Fig.2.20 Evaluation of segmentation results for 22 images. (a) and (b) Segmentation error for each test case; (c) and (d) Amount of lowest errors for each TMG metric

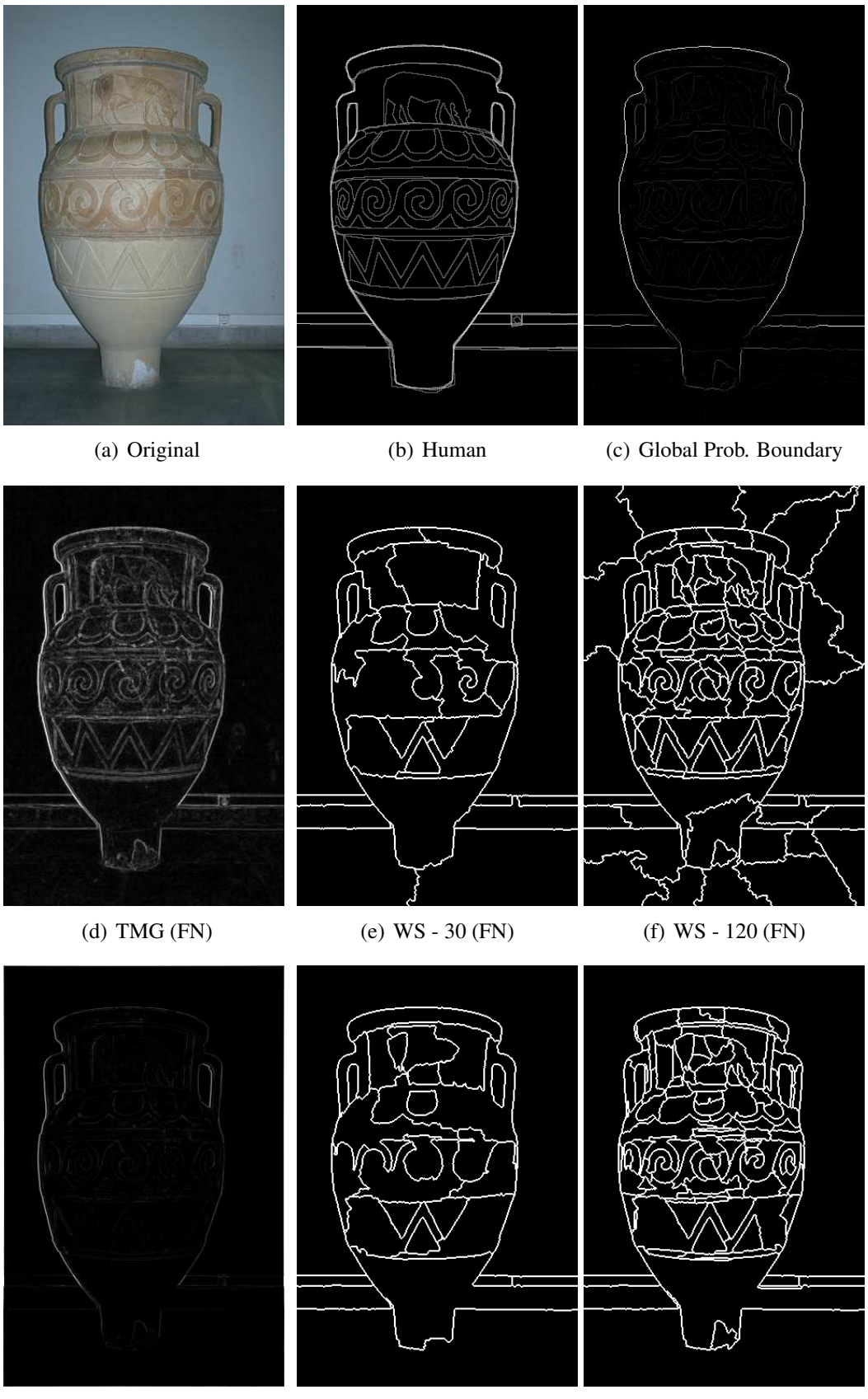

(a) Original (b) Human (c) Global Prob. Boundary

(d) TMG (FN) (e) WS - 30 (FN) (f) WS - 120 (FN)

(g) DiZenzo gradient (h) WS - 30 (DiZenzo) (i) WS - 120 (DiZenzo)

Fig.2.22 TMGs compared to other segmentation algorithms

Apêndice C

Imagens coloridas do Capítulo 4

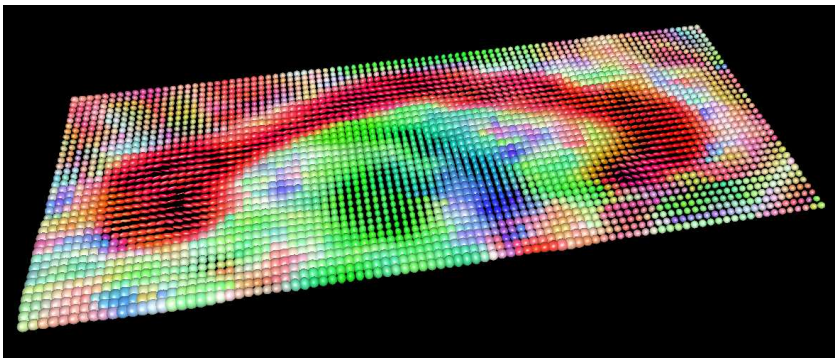

Fig.4.1 Ellipsoids representing the diffusion tensors in the region containing the corpus callosum

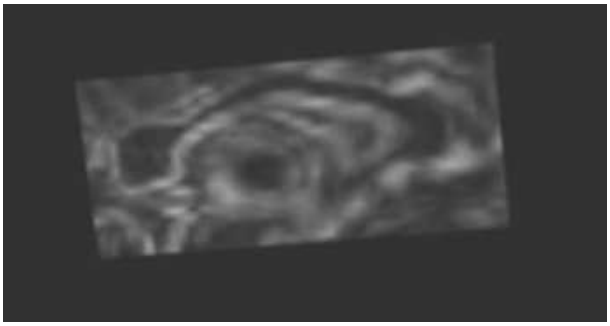

(a) Tensorial morphological gradient (TMG)

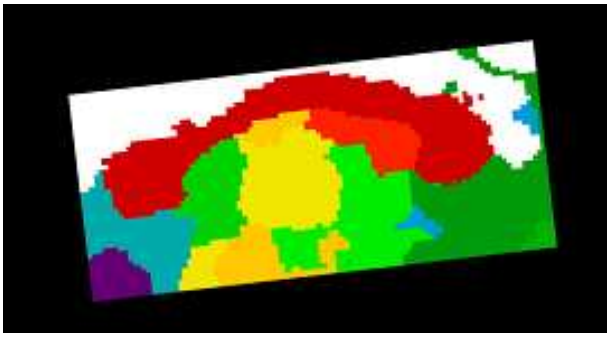

(b) Resulting labeled regions from Watershed on TMG

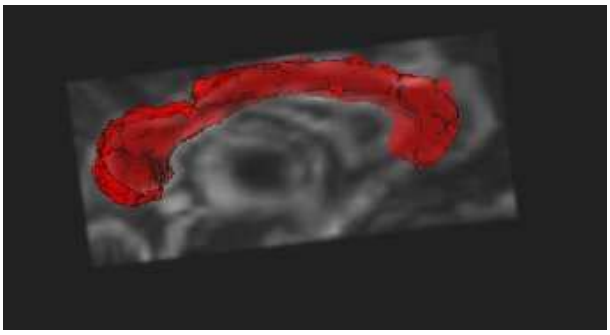

(c) Corpus callosum (3D) segmented by the watershed on the TMG

Fig.4.2 Segmenting the corpus callosum: the computed TMG (one slice), the hierarchical watershed transform (one slice) and the 3D segmentation result

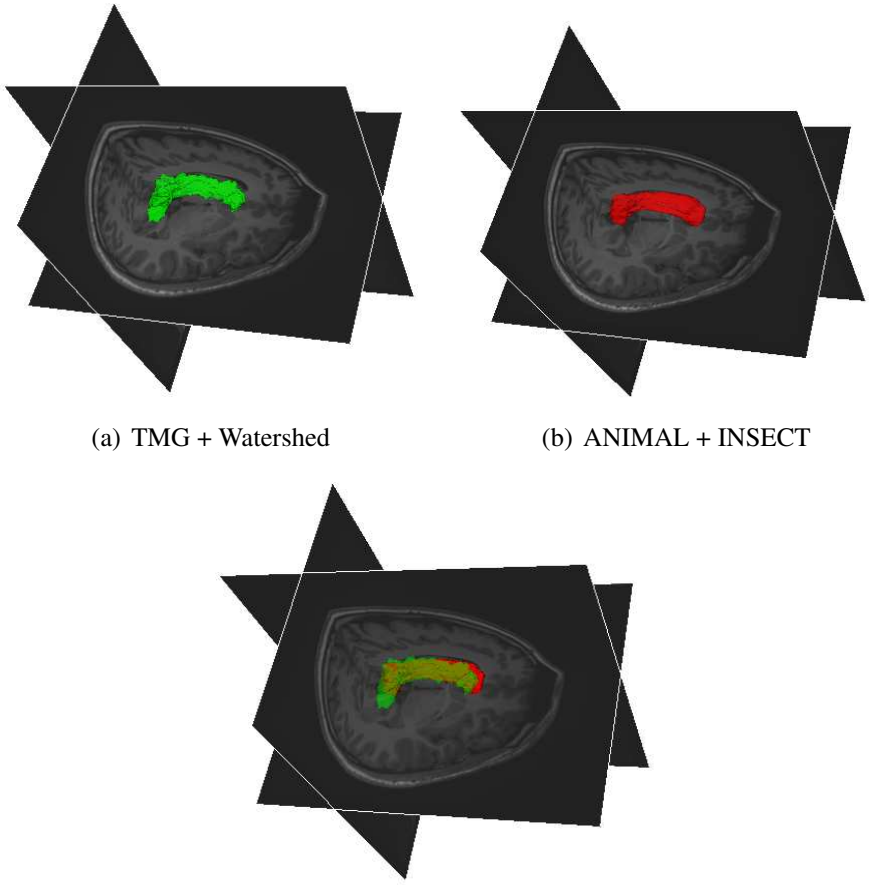

(a) TMG + Watershed

(b) ANIMAL + INSECT

(c) Both results (overlaid)

Fig.4.3 Comparison of corpus callosum obtained by different segmentation methods: In green, the TMG+Watershed performed on DTI and in red, the ANIMAL+INSECT performed on T1, T2 and PD images

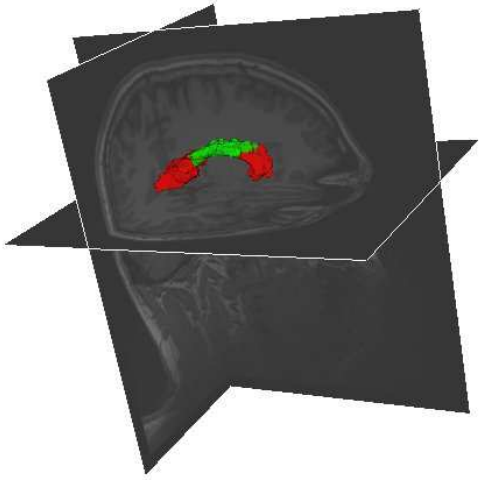

Fig.4.4 3D segmentation result of corpus callosum, when increasing the number n of regions. Instead of only one label, three labels were assigned to the corpus callosum by the watershed transform.

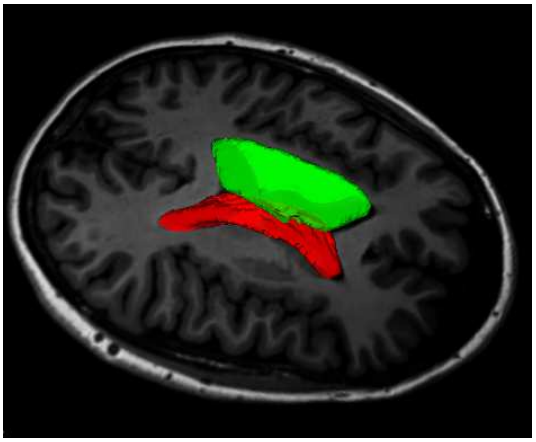

(a) ANIMAL

Fig.4.5 Left and right ventricles, segmented by the watershed transform on the TMG

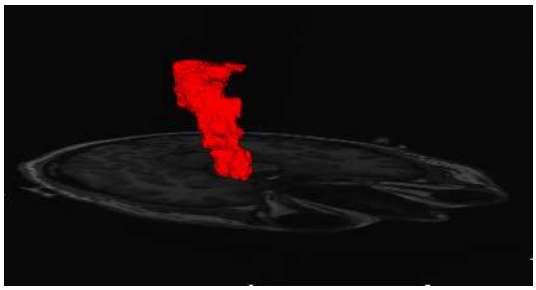

Fig.4.6 Segmentation of cortico-spinal tract by the proposed method

Apêndice D

Imagens coloridas do Capítulo 5

(a) DTI (b) λ_1 (c) λ_2 (d) λ_3 (e) PED

Fig.5.5 Corpus Callosum: the diffusion tensors represented by ellipsoids, each eigenvalue (λ_1, λ_2 and λ_3) shown separately and the principal eigenvector direction (e_1). Small λ_2 and λ_3 and uniform color of e_1 confirm that the corpus callosum is a highly oriented structure.

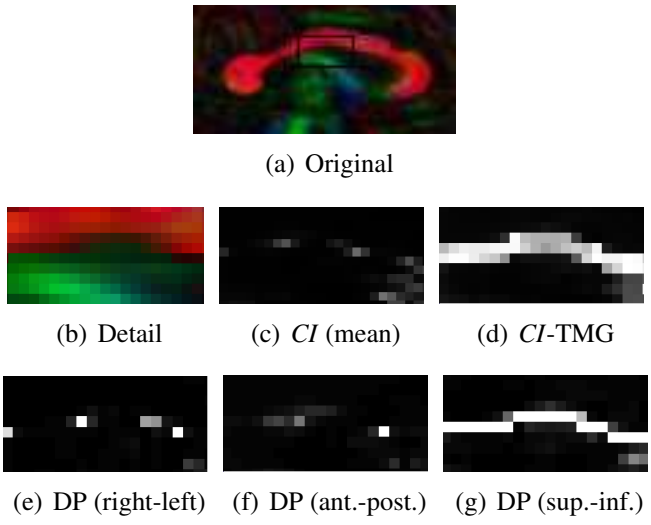

(a) Original

(b) Detail (c) *CI* (mean) (d) *CI*-TMG

(e) DP (right-left) (f) DP (ant.-post.) (g) DP (sup.-inf.)

Fig.5.9 Comparison of the coherence index (*CI*) computed by mean and computed using the TMG. Only a detail of the original image is shown. The dot product (DP) was computed separately for neighbors in each direction (right-left, anterior-posterior, superior-inferior).

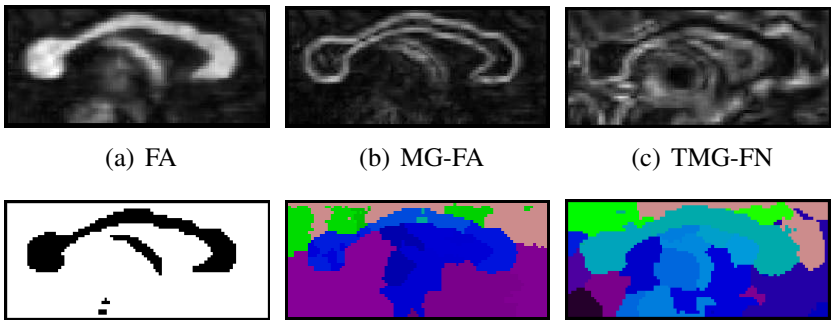

(a) FA (b) MG-FA (c) TMG-FN

(d) FA + Threshold (e) MG-FA + WS (f) TMG-FN + WS

Fig.5.11 Segmentation of Corpus Callosum using different measures and different segmentation techniques: Threshold over the *FA*; Watershed over the morphological gradient of *FA*; Watershed over the tensorial morphological gradient computed using the Frobenius Norm.

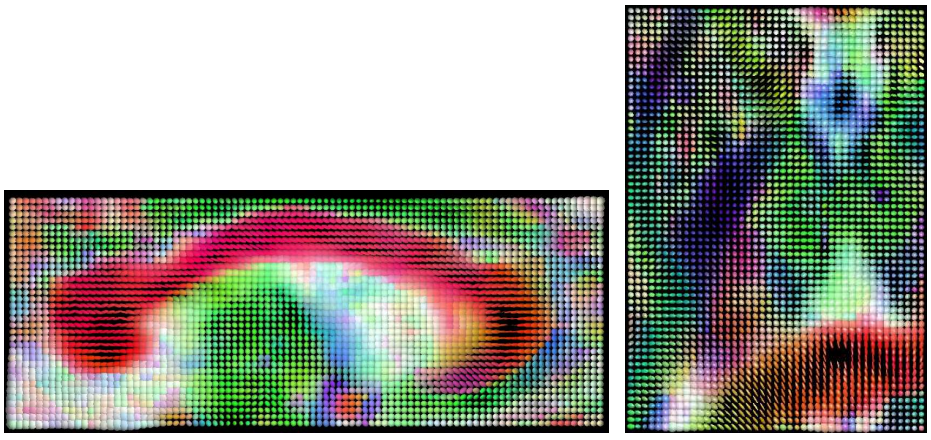

(a) DTI (b) DTI

Fig.5.12 One slice of the diffusion tensor field in the region of the corpus callosum and of the thalamus.

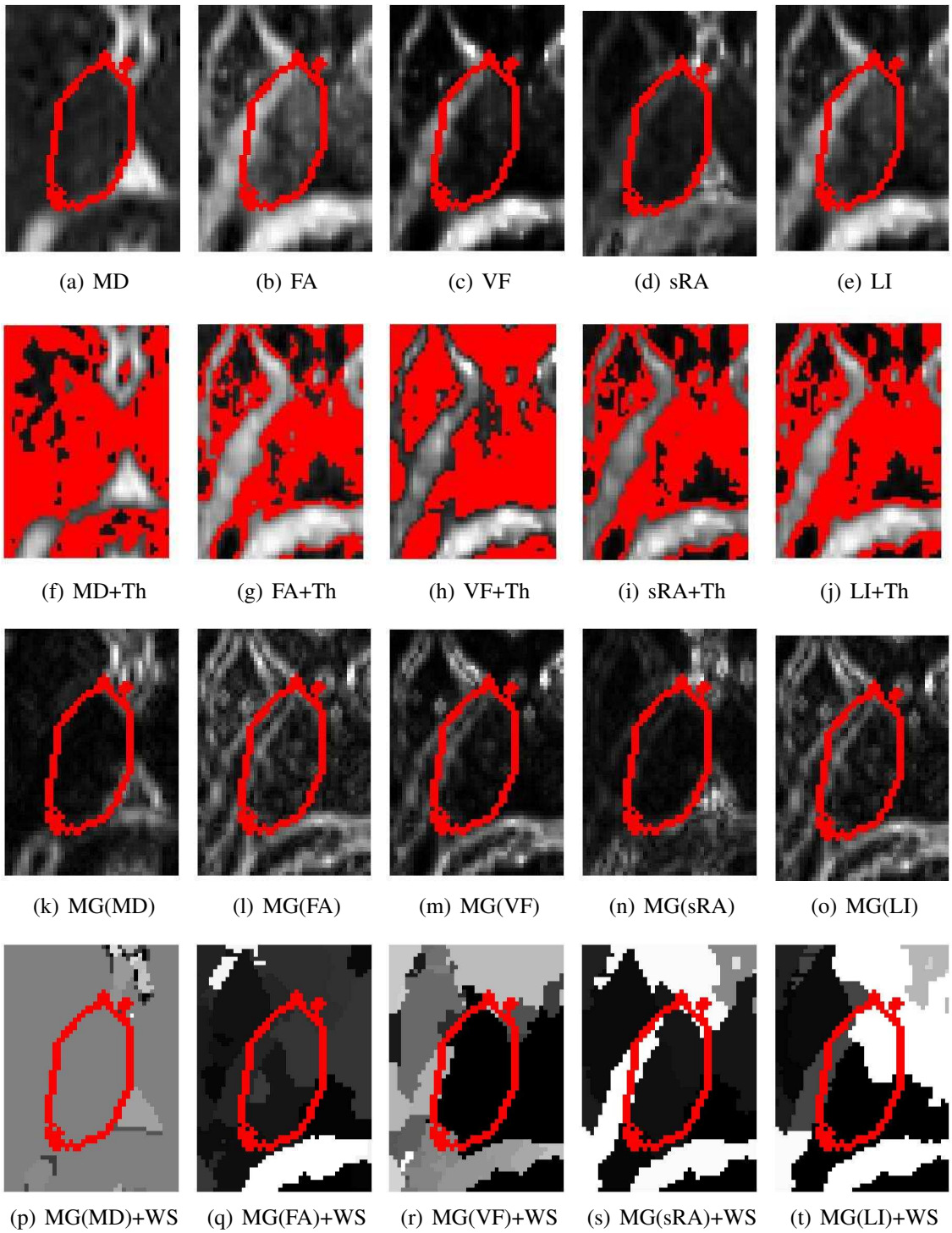

(a) MD (b) FA (c) VF (d) sRA (e) LI

(f) MD+Th (g) FA+Th (h) VF+Th (i) sRA+Th (j) LI+Th

(k) MG(MD) (l) MG(FA) (m) MG(VF) (n) MG(sRA) (o) MG(LI)

(p) MG(MD)+WS (q) MG(FA)+WS (r) MG(VF)+WS (s) MG(sRA)+WS (t) MG(LI)+WS

Fig.5.13 Segmentation experiments of the thalamus based on intravoxel measures and morphological gradients. Thresholds over the intravoxel measures were not able to segment the thalamus. Not even the morphological gradient of intravoxel measures were able to preserve borders and allow segmentation by the watershed.

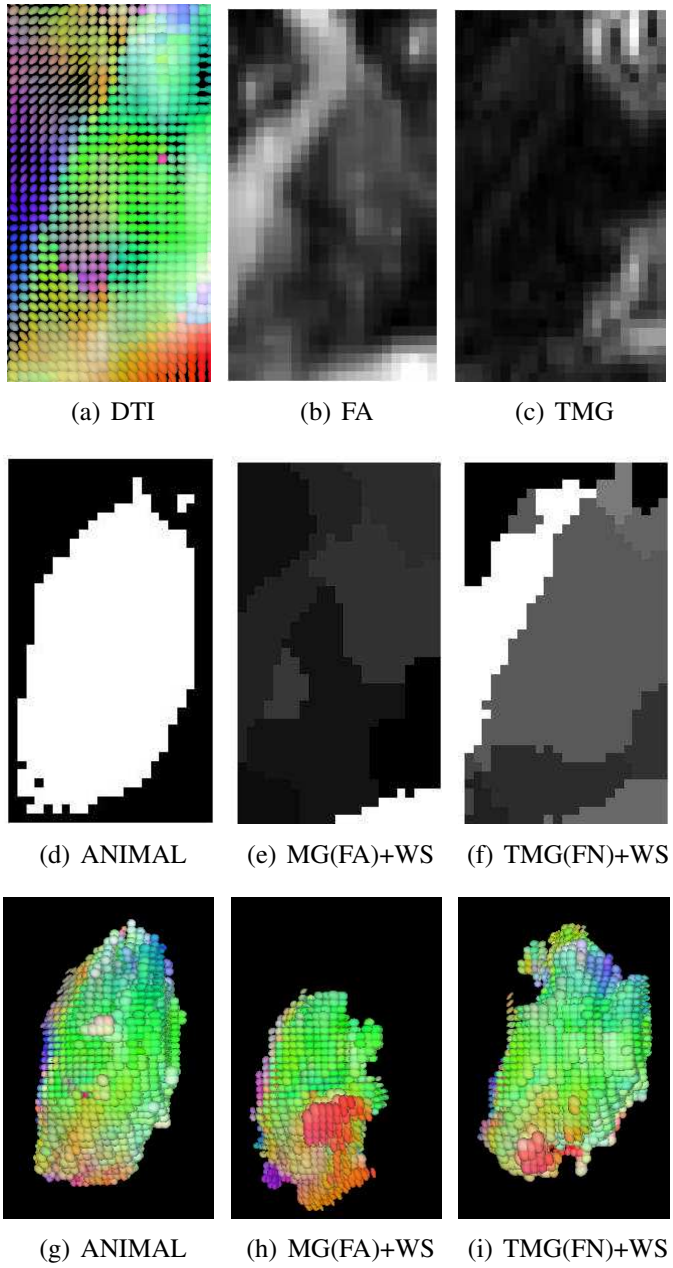

(a) DTI (b) FA (c) TMG

(d) ANIMAL (e) MG(FA)+WS (f) TMG(FN)+WS

(g) ANIMAL (h) MG(FA)+WS (i) TMG(FN)+WS

Fig.5.14 Watershed segmentation based on distinct scalar maps: morphological gradient of *FA* and tensorial morphological gradient based on FN. Comparison of obtained result with segmentation using ANIMAL. Segmentation based on the TMG-FN map is more similar to segmentation obtained by ANIMAL.

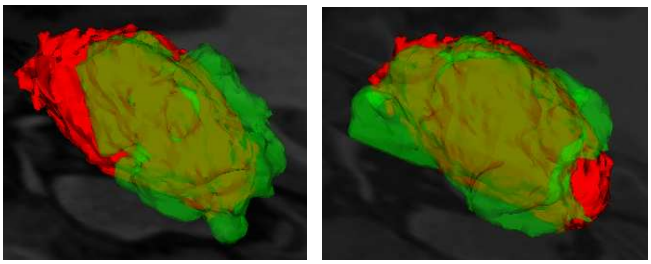

(a) MG(FA)+WS (b) TMG(FN)+WS

Fig.5.15 Results obtained by watershed (green) overlaid to ANIMAL segmentation (red), confirming the superiority of the TMG-FN over the MG-FA.

Apêndice E

Imagens coloridas do Capítulo 6

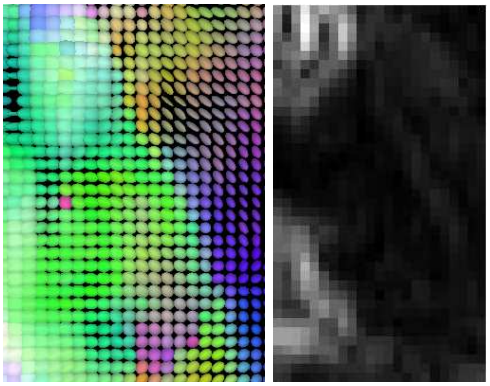

Fig.6.1 Diffusion tensors in the thalamus region (left) and respective computed TMG (right). To distinguish the clusters is not a trivial task, even for the human eye.

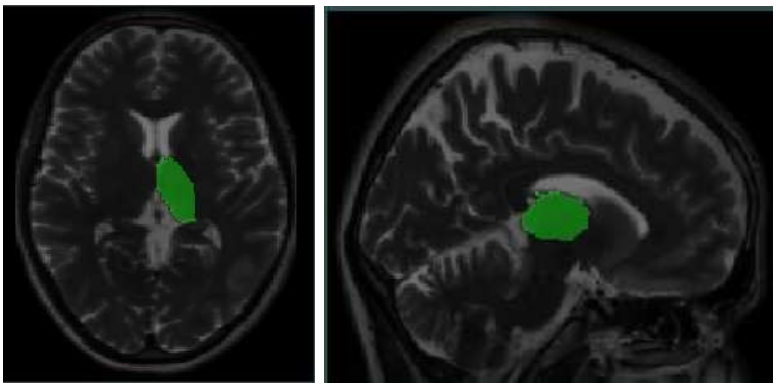

Fig.6.2 ANIMAL+INSECT segmentation for right thalamus: transverse (left) and sagittal (right) views.

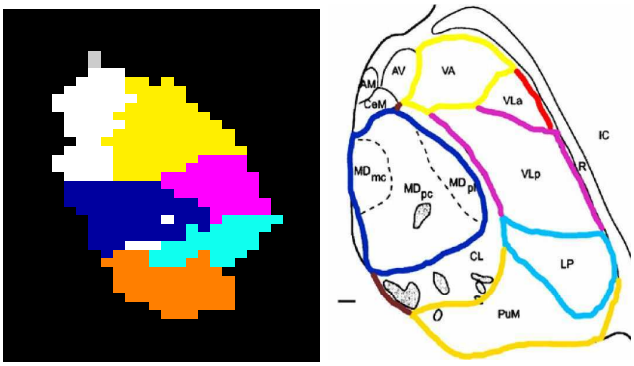

Fig.6.3 Nuclei obtained by watershed segmentation compared to Morel's histological atlas. The segmentation algorithm delineated the main nuclei, such as the Pulvinar (PuM), the Medial Dorsal (MD), the Ventral Lateral (VL), the Lateral Posterior (LP) and the Ventral Anterior (VA).

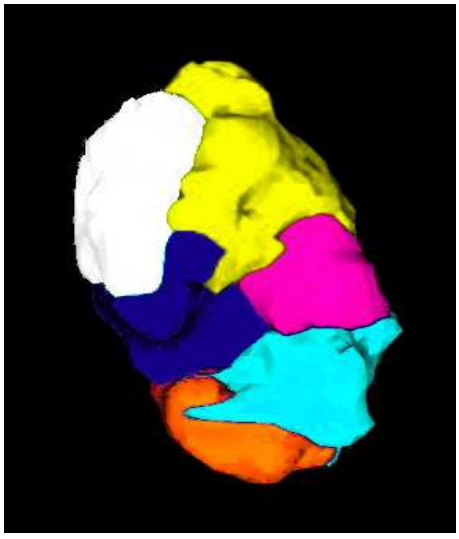

Fig.6.4 3D view of obtained nuclei using the proposed segmentation method.